

QUANTUM MONTE CARLO STUDIES OF FERMI SYSTEMS IN
LATTICE EFFECTIVE FIELD THEORY

By

Rongzheng He

A DISSERTATION

Submitted to
Michigan State University
in partial fulfillment of the requirements
for the degree of

Physics – Doctor of Philosophy

2019

ABSTRACT

QUANTUM MONTE CARLO STUDIES OF FERMI SYSTEMS IN LATTICE EFFECTIVE FIELD THEORY

By

Rongzheng He

With the rapid growth of the computational resources, quantum Monte Carlo (QMC) methodology has become a powerful tool for numerical simulations, especially for lattice effective field theory. Those QMC simulations have successfully described the physics of the few- and many-body systems. In this thesis, we investigate the Fermi systems with balanced and unbalanced populations of up and down spins using QMC with ab initio techniques. We also present a newly developed method called eigenvector continuation (EC) and its promising applications to some numerically unavoidable problems, like the sign problem in Monte Carlo simulations.

For the eigenvector continuation method, we demonstrate that although Hamiltonian is usually represented as a matrix in a linear space with enormous dimensions, the eigenvector trajectory generated by a smoothly changed Hamiltonian matrix is well approximated by a low-dimensional space. We use analytic continuation theory to prove this statement and propose an algorithm to implement our method. In the simulation with strong numerical sign oscillations, we first “learn” the subspace where the trajectory is approximately spanned by a finite number of accurately computable eigenvectors and then apply eigenvector continuation to solve the physics system where there is a severe sign problem. Our results converge rapidly as we include more eigenvectors. The results show that for the same computational cost, the EC method reduces errors by an order of magnitude compared to the direct calculations in cases when we have a strong sign problem.

In $L \times L \times L$ cubic lattices with various box sizes, we study the ground-state properties of fermionic many-body system in the unitary limit. The universal parameter (Bertsch parameter ξ) is calculated with high accuracy and the result is extrapolated to infinite volume. We characterize the superfluid phase in this system by calculating the off-diagonal long-range order of the two-body density matrix, and the condensate fraction α , which is calculated to be 0.43(1). In addition, we study the properties of the superfluid pairs. The pair size ζ_p is found to be proportional to k_F^{-1} and the ratio ζ_p/k_F^{-1} is 1.93(9).

Dedicated to my parents and fiancée.

ACKNOWLEDGMENTS

To all the people who supported me in academic and non-academic circumstances during my doctoral program: Aug. 2014 - Aug. 2017 in North Carolina State University and Sep. 2017 - Jun. 2019 in Michigan State University.

First, my deepest appreciation to my advisor Dean Lee for giving me an opportunity to work on great projects with enlightening guidance along the way. His continuous supports, heartwarming encouragements and inspiring ideas have helped keeping my passion in every step of forward going. I feel fortunate to be in such a friendly scientific environment provided by his kindness.

I would like to thank FRIB, physics and astronomy department at Michigan State University, and physics department at NC State University for building a professional atmosphere for all students and researchers.

I also would like to thank Bingnan Lu and Ning Li who are postdocs in our group for always helping when it was needed. A special thank you to Dillon Frame for the comfortable discussions and great time with you since I joined our group in NC State. I wish to thank Rhonda Bennett who is the graduate and undergraduate program coordinator in physics department at NC State. Her significant help and warm-hearted considerations made things go smoothly.

Last but not the least, I want to thank Ying who broadens my life to an extra dimension and always supports me with great patience whenever needed.

CONTRIBUTIONS TO THE THESIS

Under the guidance of my advisor, I and Dillon Frame have developed the eigenvector continuation method for the Bose-Hubbard model in matlab code and the neutron matter in Monte Carlo simulations. Working together with the collaborators, we published the following paper:

D. Frame, R.-Z. He, I. Ipsen, Da. Lee, De. Lee and E. Rrapaj,
“Eigenvector continuation with subspace learning”,
Phys. Rev. Lett. **121**, (2018) 032501.

Based on the GPU program developed by B.-N. Lu, S. Elhatisari, N. Li, and D. Lee, I have made several modifications in the algorithms for the efficient simulations of spin-unpolarized Fermi systems:

1. Building in an algorithm that generates the down-spin wave functions from the known up-spin wave functions so that the total GPU memory usage is saved for up to 75%;
2. Write in the programs that can calculate each of the observables discussed in this thesis and the corresponding stochastic errors over parallel threads.

Depending on the data collected from the Monte Carlo simulations, I have done the extrapolations towards an infinite time for all of the observables in each lattice size and the extrapolations to an infinite volume of the lattice. I have derived the lattice-based formulas for the condensate fraction, normalization of the pair wave function, and the pair size.

TABLE OF CONTENTS

LIST OF TABLES	ix
LIST OF FIGURES	x
Chapter 1 Overview	1
Chapter 2 Scattering Theory	3
2.1 Introduction	3
2.2 Lippmann-Schwinger equation	5
2.3 Partial-wave decomposition	9
2.4 Effective range expansion	12
2.5 Lüscher’s finite-volume formula	13
Chapter 3 Lattice Effective Field Theory	16
3.1 Introduction	16
3.2 Lattice regularization	18
3.3 Lattice formulation	21
3.4 Grassmann path integral	24
3.4.1 Path integral	24
3.4.2 Grassmann variables	28
3.4.3 Grassmann path integral without auxiliary field	29
3.4.4 Grassmann path integral with auxiliary field	31
3.5 Euclidean time projection method	34
3.5.1 Time projection operator	34
3.5.2 Asymptotic behavior of observable	36
3.6 Numerical methods	42
3.6.1 Monte Carlo methods	42
3.6.2 Importance sampling	43
3.6.3 Markov chain	44
3.6.4 Metropolis algorithm	45
3.6.5 Weighted average calculation	46
3.6.6 The sign problem	47
3.6.7 Eigenvector continuation method	48
Chapter 4 Systems of Fermions	60
4.1 Introduction	60
4.2 Universal parameter in the unitary limit	64
4.2.1 Free particles on the lattice	65
4.2.2 Bertsch parameter in the continuum limit	67
4.3 Superfluidity in the unitary limit	73
4.3.1 One- and two-body density matrices	74

4.3.2	Condensate fraction	76
4.4	Fulde-Ferrell-Larkin-Ovchinnikov phase	88
4.4.1	One-dimensional system	88
4.4.2	Order parameter	91
Chapter 5	Summary and outlook	98
BIBLIOGRAPHY	101

LIST OF TABLES

Table 3.1: Direct calculations and eigenvector continuation results for the ground state energy for six and fourteen neutrons using sampling data $g^2 = c_1, c_2, c_3$, where $c_1 = 0.25$, $c_2 = 0.60$, and $c_3 = 0.95$	59
Table 4.1: Sequence of momentum states filled for each spin	65
Table 4.2: Bertsch parameter extrapolation to infinite volume for fixed particle number $N = 66$ with different fitting functions. The highlighted rows are for $\xi_{N_\uparrow, N_\downarrow}^{thermo}$ and the unhighlighted rows for $\xi_{N_\uparrow, N_\downarrow}$	70
Table 4.3: Ratios between $\xi_{N_\uparrow, N_\downarrow}^{thermo}$ and $\xi_{N_\uparrow, N_\downarrow}$ for various lattice sizes with $N_\uparrow = N_\downarrow = 33$	72
Table 4.4: Condensate fraction at unitary limit extrapolated to infinite volume for fixed particle number $N = 66$ with different fitting functions.	81
Table 4.5: $\zeta_p k_F$ as a linear function of the Fermi momentum k_F with fixed particle number $N = 66$	87

LIST OF FIGURES

Figure 2.1:	Sum of bubble diagrams contributing to two-particle scattering.	15
Figure 3.1:	Chiral expansion for two-, three- and four-nucleon forces up to next-to-next-to-next-to-leading order [29]. Solid lines represent nucleons and dashed lines pions. Small dots, large solid dots, solid squares, and solid diamonds denote vertices of index $\Delta = 0, 1, 2$ and 4.	17
Figure 3.2:	Ground-state energies for $L = 5, 6$ (upper panel) and 10, 11 (lower panel) versus projection time t . The data points are fitted using the function Eq. (3.85). The projection time is in dimensionless lattice units.	39
Figure 3.3:	Two-body density versus projection time t for $L = 5, 6$. The data points are fitted by the function in form of Eq. (3.93). The projection time is in dimensionless lattice units.	41
Figure 3.4:	Convergence region of a function's series expansion about $c = 0$, with singularities z and \bar{z}	49
Figure 3.5:	Analytic extension of a function's convergence region in the complex plane.	51
Figure 3.6:	Direct calculations of the ground-state energy for six neutrons as a function of projection time. The red open squares are the raw data, solid line is the fitted curve, and the dashed lines indicate the one σ error of the fitted curve.	55
Figure 3.7:	Direct calculations of the ground-state energy for fourteen neutrons as a function of projection time. The red open squares are the raw data, solid line is the fitted curve, and the dashed lines indicate the one σ error of the fitted curve.	55
Figure 3.8:	Eigenvector continuation measurements of the ground-state energy for six neutrons versus projection time, using sampling data $g^2 = c_1, c_2, c_3$, where $c_1 = 0.25$, $c_2 = 0.60$, and $c_3 = 0.95$. We show results obtained using one vector: c_1 (red open squares), c_2 (magenta open circles), c_3 (black open triangles); two vectors: c_1, c_2 (red asterisks), c_2, c_3 (grey pluses), c_1, c_3 (blue crosses); three vectors: c_1, c_2, c_3 (orange filled squares).	58

Figure 3.9:	Eigenvector continuation measurements of the ground-state energy for fourteen neutrons versus projection time, using sampling data $g^2 = c_1, c_2, c_3$, where $c_1 = 0.25$, $c_2 = 0.60$, and $c_3 = 0.95$. We show results obtained using one vector: c_1 (red open squares), c_2 (magenta open circles), c_3 (black open triangles); two vectors: c_1, c_2 (read asterisks), c_2, c_3 (grey pluses), c_1, c_3 (blue crosses); three vectors: c_1, c_2, c_3 (orange filled squares). . . .	58
Figure 4.1:	The BEC-BCS crossover [107]. The two-body interaction is varied; when the interaction is strong, the pair is in bound state as BEC state of molecules (left); when the interaction is arbitrarily weak, Cooper pairs are formed and the system reaches the BCS limit (right); the intermediate regime at the crossover shows the pair size is comparable with inter-particle spacing (middle).	63
Figure 4.2:	The absolute value of the relative difference between $E_{N_\uparrow, N_\downarrow}^{0, free}$ and $E_{N_\uparrow, N_\downarrow}^{thermo}$ versus the total particle number $N (= 2N_\uparrow = 2N_\downarrow)$ for different lattice side length L	66
Figure 4.3:	The absolute value of relative difference between $E_{N_\uparrow, N_\downarrow}^{0, free}$ and $E_{N_\uparrow, N_\downarrow}^{thermo}$ versus L for different total particle number N with $N_\uparrow = N_\downarrow$	67
Figure 4.4:	Phase shift of s-wave at unitary limit: analytic value of phase shift (blue line) and the phase shift measure on the lattice (orange triangle).	68
Figure 4.5:	Bertsch parameter $\xi_{N_\uparrow, N_\uparrow}^{thermo}(t) = E_{N_\uparrow, N_\uparrow}^0(t)/E_{N_\uparrow, N_\uparrow}^{thermo}$ with $N_\uparrow = N_\uparrow = 33$ for various L and fitted curves extrapolated to infinite t . Note that we use dimensionless variable $E_F t$ instead of t as horizontal axis.	69
Figure 4.6:	Bertsch parameter $\xi_{N_\uparrow, N_\uparrow}(t) = E_{N_\uparrow, N_\uparrow}^0(t)/E_{N_\uparrow, N_\uparrow}^{0, free}$ with $N_\uparrow = N_\uparrow = 33$ for various L and fitted curves extrapolated to infinite t . Note that we use dimensionless variable $E_F t$ instead of t as horizontal axis.	69
Figure 4.7:	$\xi_{N_\uparrow, N_\downarrow}^{thermo}$ and $\xi_{N_\uparrow, N_\downarrow}$ measured in various lattice volumes are fitted to different functions of density ρ	71
Figure 4.8:	Logarithm of the computation time per particle per unit volume for updating auxiliary field $s(\mathbf{n}, n_t)$ at all spatial points at certain time step. . .	73
Figure 4.9:	Renormalized pair correlation function of interacting (solid curves) and non-interacting (dashed curves) ultracold Fermi gas at unitarity. Systems in same lattice, with or without interaction, are plotted with same color.	76

Figure 4.10: Renormalized pair correlation function along two particular directions: axial direction and 2D diagonal direction. The upper panel is for $L = 10$ and the lower one for $L = 11$	77
Figure 4.11: Projected TBDM, $h(r)$, (dashed lines), $(2/N)[\rho_1(r)L^3]^2$ (triangle symbols) and $h_{res}(r)$ (solid lines) for different lattice volumes: $L = 8$ (upper left), $L = 9$ (upper right), $L = 10$ (lower left) and $L = 11$ (lower right). All calculations are performed at large Euclidean projection time t	79
Figure 4.12: Condensate fraction α for various L and fitted curves extrapolated to large projection time t . Note that we use $E_F t$ instead of t as horizontal axis.	80
Figure 4.13: Condensate fraction α extrapolated to infinite volume of lattice with different functions of density ρ	82
Figure 4.14: Radial part of the pair wave function, $\phi(r)$, for a pair of fermions with distance r in different lattices. Our measurements are made at large projection time t	83
Figure 4.15: The probability of finding a pair of fermions with size r . Our measurements are made at large projection time t	83
Figure 4.16: Expectation value of fermion pair size as a function of projection time t with various lattice volumes.	85
Figure 4.17: Expectation value of pair size as a function of inverse Fermi momentum k_F^{-1} . Our measurements are made at large projection time t and the values are all in lattice units.	86
Figure 4.18: Parameter ζ_p as a function of projection time t for various lattice sizes. All values are in lattice units.	87
Figure 4.19: Values of $\zeta_p k_F$ as a function of k_F . All calculations are made at large projection time t	88
Figure 4.20: One-body correlation function in momentum space with $N_\uparrow = N_\downarrow = 15$ in an $L = 32$ one-dimensional lattice. The vertical dashed line in blue corresponds to the Fermi momentum k_F and the one in black indicates the momentum right above Fermi surface. All values are in lattice units.	90
Figure 4.21: Pair correlation function in momentum space with $N_\uparrow = N_\downarrow = 15$ in an $L = 32$ one-dimensional lattice. All values are in lattice units.	90
Figure 4.22: Fermion pair formation of unpolarized system (BCS theory) versus that of polarized system (FFLO phase) in momentum space [174].	92

Figure 4.23: Pair correlation function in polarized systems with $N_{\downarrow} = 15$ and varying N_{\uparrow} . Our one-dimensional system uses the periodic boundary condition with $L = 32$ and $c_0 = -0.06$	93
Figure 4.24: Pair correlation function in momentum space of the spin-polarized systems for different interaction strengths. All values are in lattice units.	94

Chapter 1

Overview

The study of strongly interacting Fermi systems is one of the hot topics and major challenges in physics. It is related to many physics systems, such as cold atoms, metallic superconductors and nuclear matter. By using Feshbach resonances [110] in experiment, the strength of interaction is tunable that allows us to explore the physics in many length scales. In particular, an interesting regime is the unitary limit [108, 109] where the scattering length is divergent and the effective range of the interaction is much smaller than the inter-particle distance. In this thesis, the systems of nucleons are studied using ab initio method based on the lattice effective field theory.

Effective field theory (EFT) provides a systematic framework to study the physics system at a chosen energy scale or length scale. The idea is to describe the physical interactions using relevant degrees of freedom and omitting the details at higher energy or equivalently shorter distance. The description “higher” is defined with respect to some of energy cutoff, above which the current effective theory breaks down. In order to study the low-energy phenomena of quantum chromodynamics (QCD), chiral effective field theory (χ EFT) is constructed to be consistent with the underlying symmetries of QCD, such as the symmetries of parity, charge conjugate and time reversal. The Lagrangian of χ EFT is arranged according to a power counting scheme where nuclear forces are considered order by order.

Lattice effective field theory is a useful numerical method that combines the framework

of EFT with numerical lattice methods. As the lattice volume becomes large and the lattice spacing small, we can achieve a very good approximation of the physics observed in nature. Combined with quantum Monte Carlo simulations, lattice EFT turns out to be a powerful ab initio method in low-energy nuclear physics.

In this thesis I summarize the work I have done during my Ph.D. study. In Chapter 2, we review the basic concepts of scattering theory and the low-energy scattering on the lattice. In chapter 3, we discuss how we build the effective field theory on the lattice and numerical methods we have used. We start with the introduction to lattice effective field theory and the lattice formalism with and without one-pion exchange potential. Next, we present the algorithms behind the simulations and the numerical methods involved in Monte Carlo sampling. Lastly, the eigenvector continuation method is illustrated and demonstrated to be promisingly useful in computationally difficult problems. In chapter 4, we study the polarized and unpolarized Fermi systems in one dimension and three dimensions, respectively. On the 3D lattice, we investigate the unpolarized Fermi gas at the BCS-BEC crossover with zero temperature, and the properties of unitarity are well-studied. On the 1D lattice, we characterize Fulde-Ferrell-Larkin-Ovchinnikov (FFLO) phase in spin-polarized system, whose order parameter is shown to be dependent on the polarization of the system.

Chapter 2

Scattering Theory

2.1 Introduction

Scattering (or collision) is a very important tool for us to learn about the nature of the interactions between particles. By studying the incoming and outgoing particles or waves of a scattering process, we can determine what is happening in the interaction region. In this chapter, we review the time-independent scattering theory for structureless incoming particles. Following Ref. [1], we will reintroduce the Lippmann-Schwinger equation in section 2.2 and the partial-wave decomposition in section 2.3. The effective range expansion and Lüscher's formula for finite volumes will be reviewed in section 2.4 and 2.5, respectively.

Let us start with a one-dimensional case of elastic scattering. A particle with energy $\frac{\hbar^2 \mathbf{k}^2}{2m}$ is incident from the left upon a localized potential $V(x)$, where \mathbf{k} is the wave vector. The outgoing scattered waves have two components, the reflected and transmitted waves, with wave vectors $\pm \mathbf{k}$, due to energy conservation. On the left side of the potential, the wave function is the superposition of the incoming wave and reflected wave,

$$\Psi_L(x) = e^{i\mathbf{k}x} + Ae^{-i\mathbf{k}x}, \quad (2.1)$$

and the transmitted wave is of the form,

$$\Psi_R(x) = B e^{i\mathbf{k}\mathbf{x}}. \quad (2.2)$$

In three-dimensional space, consider a wave packet at $z = -\infty$ centered on momentum $\hbar\mathbf{k}$ along the positive z direction incident on a potential $V(r)$. In the same sense as in 1D space, the scattering can be described by the incident wave plus scattered wave. In experiments, wave function inside the interacting area is inaccessible, and we are interested in the region far away from the scattering region, where the flux of particles can be measured by detectors. At $r \rightarrow \infty$, the potential vanishes and the scattered wave takes the form of an outward propagating spherical wave. Wave function for the scattering process can be written as

$$\Psi(\mathbf{r}) \xrightarrow{r \rightarrow \infty} \frac{1}{(2\pi)^{3/2}} \left[e^{ikz} + f(\theta, \mathbf{k}) \frac{e^{ikr}}{r} \right], \quad (2.3)$$

where θ is the angle between scattered wave and z axis. Two-particle scattering can be factorized as the center of mass (CM) motion plus the scattering of a single particle in the CM frame. Consequently, for two-particle scattering, in Eq. (2.3), \mathbf{r} and \mathbf{k} are understood as the relative coordinate and wave vector. The scattering amplitude $f(\theta, \mathbf{k})$ of the outgoing wave carries the details of scattering process and is closely related to the differential cross section,

$$\frac{d\sigma}{d\Omega} = |f(\theta, \mathbf{k})|^2, \quad (2.4)$$

where $\frac{d\sigma}{d\Omega}$, classically, is defined as the number of particles scattered into direction (θ, ϕ) per unit time per unit solid angle, divided by the incoming flux. According to the definition, it is easy to see that the differential cross section has dimensions of area. Straightforwardly,

the total cross section over all solid angles is obtained by

$$\sigma_{tot} = \int \frac{d\sigma}{d\Omega} d\Omega = \int_0^{2\pi} d\phi \int_0^\pi d\theta \sin(\theta) \frac{d\sigma}{d\Omega}. \quad (2.5)$$

2.2 Lippmann-Schwinger equation

Let us focus on a elastic scattering and consider a Hamiltonian that consists of a free particle Hamiltonian and an interaction,

$$H = H_0 + V. \quad (2.6)$$

Compared to the free-particle state $|\phi\rangle$, the eigenstate of H is different due to the presence of V . Since the energy is conserved, the eigenstate of interest should have the same energy E as state $|\phi\rangle$. One can write the eigenvalue equations for both states,

$$H_0|\phi\rangle = E|\phi\rangle, \quad (2.7)$$

$$(H_0 + V)|\psi\rangle = E|\psi\rangle. \quad (2.8)$$

The solution to Eq. (2.8) has to satisfy $|\psi\rangle \xrightarrow{V \rightarrow 0} |\phi\rangle$. A formal solution can be written as

$$|\psi^\pm\rangle = |\phi\rangle + \frac{1}{E - H_0 \pm i\epsilon} V |\psi^\pm\rangle, \quad (2.9)$$

where the so-called $i\epsilon$ prescription is introduced to avoid hitting pole singularities. This equation is known as the Lippmann-Schwinger equation. The physical meaning of the “ \pm ” sign will be discussed later. In the position representation, the Lippmann-Schwinger equation

can be written as

$$\langle \mathbf{x} | \psi^\pm \rangle = \langle \mathbf{x} | \phi \rangle + \int d\mathbf{x}' \langle \mathbf{x} | \frac{1}{E - H_0 \pm i\epsilon} | \mathbf{x}' \rangle \langle \mathbf{x}' | V | \psi^\pm \rangle. \quad (2.10)$$

If $|\phi\rangle$ represents a plane-wave state with momentum \mathbf{p} , the first term has the form,

$$\langle \mathbf{x} | \phi \rangle = \frac{e^{i\mathbf{p}\cdot\mathbf{x}/\hbar}}{(2\pi\hbar)^{3/2}}. \quad (2.11)$$

The kernel of the integral, contains the Green's function

$$G_\pm = \frac{\hbar^2}{2m} \langle \mathbf{x} | \frac{1}{E - H_0 \pm i\epsilon} | \mathbf{x}' \rangle, \quad (2.12)$$

where $E = \hbar^2 k^2 / 2m$. The explicit form can be written as

$$G_\pm = -\frac{1}{4\pi} \frac{e^{\pm ik|\mathbf{x}-\mathbf{x}'|}}{|\mathbf{x}-\mathbf{x}'|}. \quad (2.13)$$

Plugging it into Eq. (2.10), we have

$$\langle \mathbf{x} | \psi^\pm \rangle = \langle \mathbf{x} | \phi \rangle - \frac{2m}{\hbar^2} \int d\mathbf{x}' \frac{e^{\pm ik|\mathbf{x}-\mathbf{x}'|}}{4\pi|\mathbf{x}-\mathbf{x}'|} \langle \mathbf{x}' | V | \psi^\pm \rangle. \quad (2.14)$$

Now the wave function for this scattering process is described by the incident wave function $\langle \mathbf{x} | \phi \rangle$ plus the term that comes from scattering. The “ \pm ” sign denotes two solutions with different asymptotic behaviors. Assume V is a local potential, then in position basis we can write

$$\langle \mathbf{x}' | V | \mathbf{x}'' \rangle = V(\mathbf{x}') \delta^{(3)}(\mathbf{x}' - \mathbf{x}''). \quad (2.15)$$

Consequently,

$$\langle \mathbf{x} | \psi^\pm \rangle = \langle \mathbf{x} | \phi \rangle - \frac{2m}{\hbar^2} \int d\mathbf{x}' \frac{e^{\pm ik|\mathbf{x}-\mathbf{x}'|}}{4\pi|\mathbf{x}-\mathbf{x}'|} V(\mathbf{x}') \langle \mathbf{x}' | \psi^\pm \rangle. \quad (2.16)$$

As to the physics behind the above equation, \mathbf{x} is understood as a vector directed to the point of interest and the convolution as the summation of outgoing spherical waves weighted by the local strength of the potential multiplying the wave function $\langle \mathbf{x}' | \psi \rangle$ in the range of the scatterer. In experiment, usually the detectors are far from the center of the scattering region. It is reasonable to assume that r ($= |\mathbf{x}|$) is much larger than r' ($= |\mathbf{x}'|$). Taking this limit, we write the wave function of the scattering process as

$$\begin{aligned} \langle \mathbf{x} | \psi^\pm \rangle &\xrightarrow{r \rightarrow \infty} \langle \mathbf{x} | \mathbf{k} \rangle - \frac{1}{4\pi} \frac{2m}{\hbar^2} \frac{e^{\pm ikr}}{r} \int d\mathbf{x}' e^{\mp i\mathbf{k}' \cdot \mathbf{x}'} V(\mathbf{x}') \langle \mathbf{x}' | \psi^{pm} \rangle \\ &= \frac{1}{(2\pi)^{3/2}} \left[e^{i\mathbf{k} \cdot \mathbf{x}} + \frac{e^{\pm ikr}}{r} f^\pm(\mathbf{k}', \mathbf{k}) \right], \end{aligned} \quad (2.17)$$

where \mathbf{k}' is the wave vector for waves propagating towards observation point \mathbf{x} . The “+” solution (“-” solution) corresponds to the plane wave plus an outgoing (incoming) spherical wave. We are primarily interested in the positive solution, since it is difficult to prepare a system to satisfy the boundary condition appropriate for the negative solution. The amplitude of scattered spherical wave is given by

$$\begin{aligned} f(\mathbf{k}', \mathbf{k}) &= -\frac{1}{4\pi} \frac{2m}{\hbar^2} (2\pi)^3 \int d\mathbf{x}' \frac{e^{-i\mathbf{k}' \cdot \mathbf{x}'}}{(2\pi)^{3/2}} V(\mathbf{x}') \langle \mathbf{x}' | \psi^+ \rangle \\ &= -\frac{1}{4\pi} \frac{2m}{\hbar^2} (2\pi)^3 \langle \mathbf{k}' | V | \psi^+ \rangle, \end{aligned} \quad (2.18)$$

where Eq. (2.15) is used in last step. We can define the transition operator T such that

$$V | \psi^+ \rangle \equiv T | \phi \rangle, \quad (2.19)$$

and write the scattering amplitude $f(\mathbf{k}', \mathbf{k})$ as

$$f(\mathbf{k}', \mathbf{k}) = -\frac{1}{4\pi} \frac{2m}{\hbar^2} (2\pi)^3 \langle \mathbf{k}' | T | \mathbf{k} \rangle. \quad (2.20)$$

Thus, to determine $f(\mathbf{k}, \mathbf{k}')$, it is sufficient to know the transition operator T . Multiplying V on both sides of the Lippmann-Schwinger equation and using Eq. (2.19), we obtain

$$T|\phi\rangle = V|\phi\rangle + V \frac{1}{E - H_0 + i\epsilon} T|\phi\rangle. \quad (2.21)$$

In this equation, $|\phi\rangle$ can be any plane-wave eigenstate and the basis formed by those momentum state is complete. Therefore, we can write the following operator equation

$$T = V + V \frac{1}{E - H_0 + i\epsilon} T. \quad (2.22)$$

Eq. (2.22) can be solved iteratively, yielding

$$T = V + V \frac{1}{E - H_0 + i\epsilon} V + V \frac{1}{E - H_0 + i\epsilon} V \frac{1}{E - H_0 + i\epsilon} V + \dots. \quad (2.23)$$

When the potential V is sufficiently weak, the above series will converge. However, if the potential is too small so that the series converges for all energies, then the potential supports no bound states. For a given potential V , there exists an energy E' above which the series converges; the higher the energy ($> E'$) the more rapid the convergence.

2.3 Partial-wave decomposition

It is the potential V that leads to a different eigenstate from a free-particle state. In order to study the interaction, we start with the transition operator T . Note that H_0 , the kinetic-energy operator, commutes with operators \mathbf{L}^2 and L_z ; hence l and m are good quantum numbers for the eigenstate denoted by $|E, l, m\rangle$ called a spherical-wave state. When it comes to the operator T , if V is a spherically symmetric potential, according to Eq. (2.23), T must be invariant under rotations in three dimensions. Equivalently, operators T , \mathbf{L}^2 and L_z commute with each other, and hence T is a scalar operator. The Wigner-Eckart theorem [1] immediately yields

$$\langle E', l', m' | T | E, l, m \rangle = T_l(E', E) \delta_{l'l} \delta_{m'm}, \quad (2.24)$$

in which T is diagonal in l and m and the diagonal elements are independent of m . Now we expand the plane wave $\langle \mathbf{x} | \mathbf{k} \rangle$, as follows

$$\frac{e^{i\mathbf{k}\cdot\mathbf{x}}}{(2\pi)^{3/2}} = \frac{1}{(2\pi)^{3/2}} \sum_{l=0}^{\infty} (2l+1) i^l j_l(kr) P_l(\cos\theta), \quad (2.25)$$

where $j_l(kr)$ is the spherical Bessel function of order l and $P_l(\cos\theta)$ is a Legendre polynomial with the angle between \mathbf{k} and \mathbf{r} denoted by θ . At large r , the spherical Bessel function behaves like

$$j_l(kr) \xrightarrow{r \rightarrow \infty} \frac{e^{i(kr-l\pi/2)} - e^{-i(kr-l\pi/2)}}{2ikr}. \quad (2.26)$$

Plugging Eq. (2.26) into Eq. (2.25), we obtain

$$\langle \mathbf{x} | \mathbf{k} \rangle \xrightarrow{r \rightarrow \infty} \frac{1}{(2\pi)^{3/2}} \sum_l^{\infty} (2l+1) \frac{P_l(\cos \theta)}{2ik} \left[\frac{e^{ikr}}{r} - \frac{e^{-i(kr-l\pi)}}{r} \right], \quad (2.27)$$

where $i^l = e^{il\pi/2}$ is used. Now the plane wave can be understood as the sum of a spherically outgoing wave, e^{ikr}/r , and a spherically incoming wave, $e^{-i(kr-l\pi)}/r$, over the quantum number l . Each value of l corresponds to a certain angular momentum and thus the incident wave is decomposed into its constituent partial waves in this way. For elastic scattering from a central potential, the scattering amplitude has to be symmetrical about the incident axis.

We can write $f(\mathbf{k}', \mathbf{k})$ in terms of the Legendre polynomials,

$$f(\mathbf{k}', \mathbf{k}) = f(\theta) = \sum_{l=0}^{\infty} (2l+1) f_l(k) P_l(\cos \theta), \quad (2.28)$$

where amplitude of the partial waves are defined as

$$f_l(k) = -\frac{\pi T_l(E)}{k} \Big|_{E=\hbar^2 k^2/2m}. \quad (2.29)$$

The scattering wave function at large r takes the form of

$$\begin{aligned} \langle \mathbf{x} | \psi^+ \rangle &\xrightarrow{r \rightarrow \infty} \frac{1}{(2\pi)^{3/2}} \left[e^{i\mathbf{k} \cdot \mathbf{x}} + f(\theta) \frac{e^{ikr}}{r} \right] \\ &= \frac{1}{(2\pi)^{3/2}} \left\{ \sum_l^{\infty} (2l+1) \frac{P_l(\cos \theta)}{2ik} \left[\frac{e^{ikr}}{r} - \frac{e^{-i(kr-l\pi)}}{r} \right] \right. \\ &\quad \left. + \sum_l^{\infty} (2l+1) P_l(\cos \theta) f_l(k) \frac{e^{ikr}}{r} \right\} \\ &= \frac{1}{(2\pi)^{3/2}} \sum_l^{\infty} (2l+1) \frac{P_l(\cos \theta)}{2ik} \left\{ \left[1 + 2ik f_l(k) \right] \frac{e^{ikr}}{r} - \frac{e^{-i(kr-l\pi)}}{r} \right\}. \end{aligned} \quad (2.30)$$

Comparing Eq. (2.27) and (2.30), it is clear that the effects of the scatterer only enter into $2ikf_l(k)$; other parts in the wave function remain the same. In elastic scattering, the flux must be conserved before, and after the scattering and the angular momentum is also conserved. Therefore, the flux conservation holds for each partial wave separately. This means $|1 + 2ikf_l(k)| = 1$ for each l . Now we can define

$$S_l(k) \equiv 1 + 2ikf_l(k) = e^{2i\delta_l(k)}, \quad (2.31)$$

with the real-valued phase shift $\delta_l(k)$ for the l th partial wave. Reconsidering $f_l(k)$, it can be expressed as

$$f_l(k) = \frac{e^{2i\delta_l(k)} - 1}{2ik} = \frac{e^{i\delta_l(k)} \sin \delta_l(k)}{k} = \frac{1}{k \cot \delta_l(k) - ik}. \quad (2.32)$$

The full scattering amplitude then becomes

$$\begin{aligned} f(\theta) &= \sum_{l=0}^{\infty} (2l+1) \left(\frac{e^{2i\delta_l(k)} - 1}{2ik} \right) P_l(\cos \theta) \\ &= \frac{1}{k} \sum_{l=0}^{\infty} (2l+1) e^{i\delta_l(k)} [\sin \delta_l(k)] P_l(\cos \theta). \end{aligned} \quad (2.33)$$

Following the above equation, the total cross section is given by

$$\begin{aligned} \sigma_{tot} &= \int |f(\theta)|^2 d\Omega \\ &= \frac{4\pi}{k^2} \sum_{l=0}^{\infty} (2l+1) \sin^2 \delta_l(k). \end{aligned} \quad (2.34)$$

From the last two equations, the optical theorem [2] is obtained

$$\text{Im}[f(\theta = 0)] = \frac{k}{4\pi} \sigma_{tot}, \quad (2.35)$$

which relates the imaginary part of forward-scattering amplitude $f(\theta = 0) \equiv f(\mathbf{k}, \mathbf{k})$ to the total cross section σ_{tot} .

2.4 Effective range expansion

Let us revisit the partial-wave amplitude $f_l(k)$ or equivalently $f_l(p)$ with $p \equiv \hbar k$. For all exponentially bounded potential V , it can be proved that $f_l(p)$ is analytic at low momentum [3] and the dependence on p has the form of

$$\lim_{p \rightarrow 0} f_l(p) = O(p^{2l}). \quad (2.36)$$

Following the last equality in Eq. (2.32), the partial-wave amplitude can be expressed as

$$f_l(p) = \frac{p^{2l}}{p^{2l+1} \cot \sigma_l(p) - ip^{2l+1}}. \quad (2.37)$$

In general, $f_l(p)$ can be written as a power series expansion of the relative momentum p that starts with a term of order $O(p^{2l})$. In some situations, it is convenient to expand $p^{2l+1} \cot \delta_l(p)$ instead of $f_l(p)$. The Taylor expansion in terms of the relative momentum p is known as the effective range expansion [4, 5],

$$p^{2l+1} \cot \delta_l(p) = -\frac{1}{a_l} + \frac{1}{2}r_l p^2 + b_l p^4 + c_l p^6 + O(p^8), \quad (2.38)$$

where a_l is the scattering length, r_l is the effective range of potential, and the coefficients of higher order terms are the shape parameters related specifically to the l th partial wave. In the context of the partial-wave decomposition, a low-momentum incident wave is decomposed

into a few partial waves with a relatively small l_{max} , while an incident wave with a high momentum P_{in} corresponds to a large l_{max} for the partial waves. This correspondence between P_{in} and l_{max} can be understood via De Broglie equation $\lambda = \frac{\hbar}{p}$ as follows. For a long wave or equivalently a low-momentum wave, only the rough structure of a potential can be resolved, for example, when the S-wave scattering dominates; however, a short wave or equivalently a high-momentum wave can “see” the fine structure of the scattering center, for instance, a dumbbell-like shape for $l = 1$.

Focusing on the low-momentum limit, S-wave scattering has the effective range expansion

$$p \cot \delta_0(p) = -\frac{1}{a_0} + \frac{1}{2}r_0p^2 + O(p^4). \quad (2.39)$$

When the scattering length $a_0 \rightarrow \infty$ and the effective range $r_0 \rightarrow 0$, we find the phase shift $\delta_0 \equiv \pi/2$. In this so-called unitary limit, the system has some universal properties. We will study the ultracold Fermi gas in this limit in Chapter 4.

2.5 Lüscher’s finite-volume formula

Our Monte Carlo simulations of many-body system are performed on a lattice with finite volume $L \times L \times L$ ¹, but real physics happens without this constraint. In order to connect the calculations in a finite box to physics in the infinite volume, we use Lüscher’s formula² [6–9]. The two-particle energy spectrum in center-of-mass frame is related to the S-wave phase shift by

$$p \cot \sigma_0(p) = \frac{1}{\pi L} S(\eta), \quad (2.40)$$

¹See details in Chapter 3

²See modifications and generalizations to Lüscher’s formula in Refs. [11–15]

where

$$\eta = \left(\frac{Lp}{2\pi} \right)^2, \quad (2.41)$$

and $S(\eta)$ is the three-dimensional zeta function,

$$S(\eta) = \lim_{\Lambda \rightarrow \infty} \left[\sum_{\mathbf{n}} \frac{\theta(\Lambda^2 - \mathbf{n}^2)}{\mathbf{n}^2 - \eta} - 4\pi\Lambda \right]. \quad (2.42)$$

where Λ is the momentum cutoff scale. For $|\eta| < 1$, we expand $S(\eta)$ in powers of η ,

$$\begin{aligned} S(\eta) &= -\frac{1}{\eta} + \lim_{\Lambda \rightarrow \infty} \left[\sum_{|\mathbf{n}| \neq 0} \frac{\theta(\Lambda^2 - \mathbf{n}^2)}{\mathbf{n}^2 - \eta} - 4\pi\Lambda \right] \\ &= -\frac{1}{\eta} + S_0 + S_1\eta^1 + S_2\eta^2 + S_3\eta^3 + \dots, \end{aligned} \quad (2.43)$$

where

$$S_0 = \lim_{\Lambda \rightarrow \infty} \left[\sum_{|\mathbf{n}| \neq 0} \frac{\theta(\Lambda^2 - \mathbf{n}^2)}{\mathbf{n}^2} - 4\pi\Lambda \right], \quad (2.44)$$

$$S_{j \geq 1} = \sum_{|\mathbf{n}| \neq 0} \frac{1}{|\mathbf{n}|^{2j+2}}. \quad (2.45)$$

The first few coefficients are

$$S_0 = -8.913631, \quad S_1 = 16.532288, \quad S_2 = 8.401924, \quad S_3 = 6.945808, \quad (2.46)$$

$$S_4 = 6.426119, \quad S_5 = 6.202149, \quad S_6 = 6.098184, \quad S_7 = 6.048263.$$

Lüscher's formula does not include effects of a finite cutoff or the contribution from higher partial waves coupling for particles with spin. If we have asymptotically small momenta, then the corrections are negligible and the effective expansion Eq. (2.39) still can hold. In

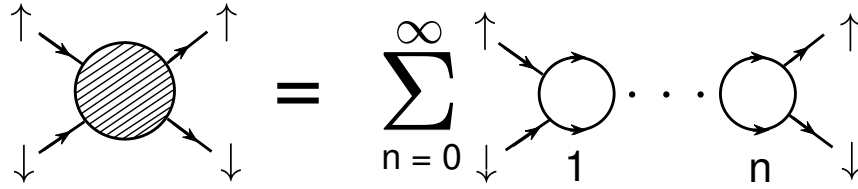


Figure 2.1: Sum of bubble diagrams contributing to two-particle scattering.

terms of η , the energy of the two-particle scattering state is

$$E_{pole} = \frac{p^2}{2m} = \frac{\eta}{m} \left(\frac{2\pi}{L} \right)^2. \quad (2.47)$$

The location of the two-particle scattering pole can be computed by summing the bubble diagram shown in Fig. 2.1 [10].

Chapter 3

Lattice Effective Field Theory

3.1 Introduction

Fascinating phenomena exist at all length scales and energy scales. Fortunately, understanding the phenomena at a particular scale does not require knowledge of what is going on at all scales [16, 17]. Based on this fact, the goal of effective field theory (EFT) is to describe the physics at a chosen length scale or energy scale, while ignoring substructure and short-distance details. One successful example is the Fermi theory of beta decay [18]. The theory posited a point-like interaction between four fermions at a point vertex and was in good agreement with low-energy experiments. Since then we have found that the underlying interactions involve the exchange of W particles of mass about 80 GeV. This heavy mass is responsible for the very short-range interaction and the point approximation was sufficient for describing beta decay experiments at an energy scale of less than 10 MeV. EFT turns out to be an very important tool for simplifying the systems with widely-separated energy scales [19–23].

In order to study a physical system at certain energy scale, it is crucial to find the appropriate variables or degrees of freedom to describe the system at hand. The first step is to choose a cutoff momentum scale Λ . We only consider momentum modes Q below Λ and integrate out high momentum modes above [17]. The low-energy Lagrangian can

then be expanded as a power series in Q/Λ , and the high-energy information is reflected in the expansion coefficients. We can always improve our model by including higher-order interactions as small perturbations. EFT yields an infinite number of terms and hence it is in general non-renormalizable; however, it is not an issue at a given order of the series expansion.

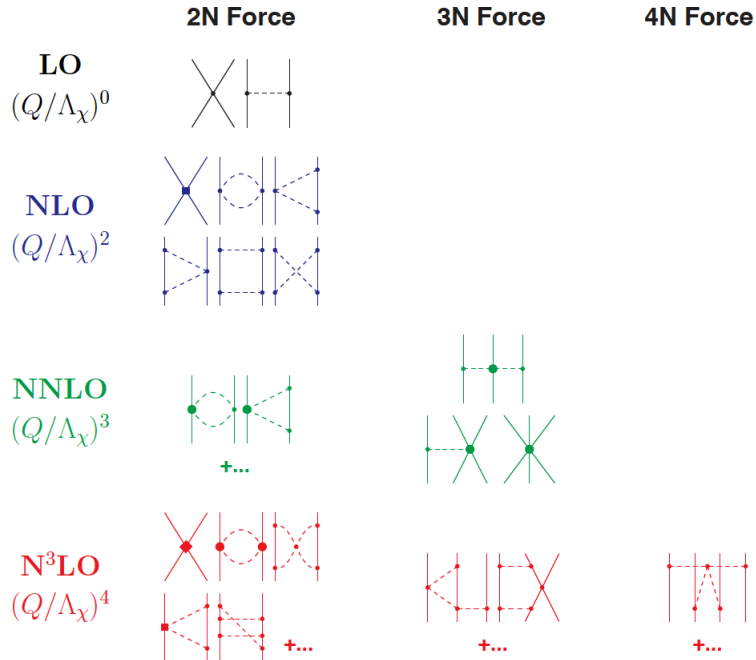


Figure 3.1: Chiral expansion for two-, three- and four-nucleon forces up to next-to-next-to-next-to-leading order [29]. Solid lines represent nucleons and dashed lines pions. Small dots, large solid dots, solid squares, and solid diamonds denote vertices of index $\Delta = 0, 1, 2$ and 4.

Any effective theory as an approximation for some underlying physical theory should take the most general form of Lagrangian consistent with analyticity, perturbative unitarity, cluster decomposition¹ and the assumed symmetries [26, 27]. In particular, chiral effective field theory constructs a Lagrangian that is consistent with the (approximate) chiral symmetry of quantum chromodynamics (QCD), as well as other symmetries such as parity and charge

¹In short, cluster decomposition theorem means that sufficiently separated regions behave independently. See Refs. [24, 25] for details of the cluster decomposition theorem.

conjugation [28, 29]. The Lagrangian is expanded in powers of Q/Λ_χ , where Q denotes the momentum scale in the physical system and Λ_χ is chiral symmetry breaking scale. By using power counting, the terms in expansion are arranged in order of importance, and then we can quantify the truncation errors. In Fig. 3.1 we represent the hierarchy of nuclear forces in chiral EFT. As an illustration, the first row shows the leading order (LO) of the expansion, which describes a two-nucleon force consisting of contact interactions and the one-pion exchange potential.

3.2 Lattice regularization

In this section we will talk about the energy spectrum of a finite-volume system at a sufficiently low energy scale. We use natural units by setting \hbar and the speed of light to 1. Consider a one-dimensional system of length L with periodic boundary condition. The possible momenta are

$$p = n \frac{2\pi}{L}, \quad n \in \mathbb{Z}, \quad (3.1)$$

and we write a momentum state with momentum p ,

$$|p\rangle = a_p^\dagger |0\rangle, \quad (3.2)$$

where $|0\rangle$ is the vacuum state with $\langle 0|0\rangle = 1$. a_p^\dagger and a_p are defined as the creation and annihilation operators with momentum p . In a momentum basis, the coordinate space creation and annihilation operators $a^\dagger(x)$ and $a(x)$ can be expanded as

$$a(x) = \frac{1}{\sqrt{L}} \sum_p e^{ipx} a_p, \quad a^\dagger(x) = \frac{1}{\sqrt{L}} \sum_p e^{-ipx} a_p^\dagger, \quad (3.3)$$

and the kinetic energy operator has the form

$$H_{free} = \sum_p \frac{p^2}{2m} a_p^\dagger a_p, \quad (3.4)$$

where the summation is over all possible momenta. At low momentum, one can neglect the higher-order terms in the effective range expansion of the interaction (Eq. (2.39)) and write

$$p \cot \delta_0(p) \approx -\frac{1}{a_0}. \quad (3.5)$$

Therefore, the interaction is taken to be in the form of a delta function

$$V(x_1 - x_2) = C \cdot \delta(x_1 - x_2). \quad (3.6)$$

Using the second quantization, the above potential can be written as

$$\begin{aligned} V &= \frac{1}{2} \int_0^L dx_1 \int_0^L dx_2 : a^\dagger(x_1) a(x_1) V(x_1 - x_2) a^\dagger(x_2) a(x_2) : \\ &= \frac{1}{2} C \int_0^L dx : (a^\dagger(x) a(x))^2 :, \end{aligned} \quad (3.7)$$

where Eq. (3.6) is used in the second step. Plugging relations Eq. (3.3) into Eq. (3.7), we obtain

$$V = \frac{1}{2} \frac{C}{L} \sum_{p_1, p_2, p'_1, p'_2} a_{p'_1}^\dagger a_{p'_2}^\dagger a_{p_1} a_{p_2} \delta_{p_1+p_2, p'_1+p'_2}, \quad (3.8)$$

where p_i and p'_i indicate the momenta before and after the interaction. Since we are interested in the low-momentum two-particle spectrum, we set a momentum cutoff scale Λ . Consequently, the possible momentum modes are $p = 0, \pm \frac{2\pi}{L}, \pm \frac{4\pi}{L}, \dots, \pm \Lambda$ and we have approximately $(\frac{\Lambda L}{\pi})^3$ independent terms on the right hand side of Eq. (3.8). In D-dimensional

$\int_0^L dx \rightarrow a_{latt} \sum_{n=0}^{N-1}$
$a(x) \rightarrow a(n)$
$\frac{\partial^2}{\partial x^2} a(x) \rightarrow \frac{a(n+1)+a(n-1)-2a(n)}{a_{latt}^2}$
$[a(n), a^\dagger(n')] = \delta_{n,n'}$

space, this number becomes $(\frac{\Lambda L}{\pi})^{3D}$, which shows that calculations become exponentially more expensive as Λ or L increase. To avoid this, we build our system on a lattice with size L using the mapping table above, and also constrain that $a(N) = a(0)$ and $a^\dagger(N) = a^\dagger(0)$ to keep the periodic boundary condition. The lattice spacing a_{latt} equals L/N .

We rewrite the kinetic operator in position space,

$$H_{free} = -\frac{1}{2m} \int_0^L dx a^\dagger(x) \frac{\partial^2}{\partial x^2} a(x), \quad (3.9)$$

using dimensionless lattice units so that any physical quantity is multiplied by powers of a_{latt} to make a dimensionless combination. Evaluating the derivative on lattice, we obtain the non-interacting Hamiltonian on this lattice,

$$H_{free} = -\frac{1}{2m} \sum_{n=0}^{N-1} [a^\dagger(n+1)a(n) + a^\dagger(n)a(n+1) - 2a^\dagger(n)a(n)]. \quad (3.10)$$

Note that this is built on a one-dimensional space and only the nearest-neighbor hopping terms are considered. In the next section, we will show the three-dimensional H_{free} with up to third nearest-neighbor hopping terms taken into account. Concluding this section, we

write the full Hamiltonian on 1D lattice,

$$H = H_{free} + \frac{C}{2} \sum_{n=0}^{N-1} : (a^\dagger(n)a(n))^2 : . \quad (3.11)$$

3.3 Lattice formulation

In lattice simulations we use a spatial lattice spacing $a = 100 \text{ MeV}^{-1}$ and a temporal step $a_t = 197 \text{ fm}/c$. The dimensionless temporal step is $\alpha_t (\equiv a_t/a)$. For the nucleon mass we use $m = 938.92 \text{ MeV}$.

Our lattice system is built on an $L \times L \times L$ periodic cube, so any operations that cross boundaries are defined with periodic boundary conditions. In the following, the notation $\sum_{\langle \mathbf{n} \mathbf{n}' \rangle}$ indicates the summation over all the nearest-neighbor sites of \mathbf{n} on lattice. $\sum_{\langle \mathbf{n} \mathbf{n}' \rangle_i}$ represents the summation over nearest-neighbor sites of \mathbf{n} along i^{th} spatial axis. In a similar way, $\sum_{\langle\langle \mathbf{n} \mathbf{n}' \rangle\rangle_i}$ is the sum over second nearest-neighbor sites of \mathbf{n} along i^{th} axis and $\sum_{\langle\langle\langle \mathbf{n} \mathbf{n}' \rangle\rangle\rangle_i}$ is the sum over third nearest-neighbor sites of \mathbf{n} along i^{th} axis.

In our calculations we only have fermions that do not involve the charge. a_{NL} is a four-component spin-isospin column vector and a_{NL}^\dagger is a four-component spin-isospin row vector. For real parameter s_{NL} , we define nonlocal annihilation and creation operators for each spin component, as follows

$$a_{NL}(\mathbf{n}) = a(\mathbf{n}) + s_{NL} \sum_{\langle \mathbf{n}' \mathbf{n} \rangle} a(\mathbf{n}'), \quad (3.12)$$

$$a_{NL}^\dagger(\mathbf{n}) = a^\dagger(\mathbf{n}) + s_{NL} \sum_{\langle \mathbf{n}' \mathbf{n} \rangle} a^\dagger(\mathbf{n}'). \quad (3.13)$$

For spin indices $S = 1, 2, 3$ and isospin indices $I = 1, 2, 3$, we define point-like densities,

$$\rho(\mathbf{n}) = a^\dagger(\mathbf{n})a(\mathbf{n}), \quad (3.14)$$

$$\rho_S(\mathbf{n}) = a^\dagger(\mathbf{n})\sigma_S a(\mathbf{n}), \quad (3.15)$$

$$\rho_I(\mathbf{n}) = a^\dagger(\mathbf{n})\tau_I a(\mathbf{n}), \quad (3.16)$$

$$\rho(\mathbf{n}) = a^\dagger(\mathbf{n})\sigma_S \otimes \tau_I a(\mathbf{n}). \quad (3.17)$$

and smeared nonlocal densities,

$$\rho_{NL}(\mathbf{n}) = a_{NL}^\dagger(\mathbf{n})a_{NL}(\mathbf{n}), \quad (3.18)$$

$$\rho_{S,NL}(\mathbf{n}) = a_{NL}^\dagger(\mathbf{n})\sigma_S a_{NL}(\mathbf{n}), \quad (3.19)$$

$$\rho_{I,NL}(\mathbf{n}) = a_{NL}^\dagger(\mathbf{n})\tau_I a_{NL}(\mathbf{n}), \quad (3.20)$$

$$\rho_{S,I,NL}(\mathbf{n}) = a_{NL}^\dagger(\mathbf{n})\sigma_S \otimes \tau_I a_{NL}(\mathbf{n}). \quad (3.21)$$

The interaction between up and down spins has the form

$$V_0 = \frac{c_0}{2} \sum_{\mathbf{n}, \mathbf{n}', \mathbf{n}''} : \rho_{NL}(\mathbf{n}) f_{s_L}(\mathbf{n} - \mathbf{n}') f_{s_L}(\mathbf{n}' - \mathbf{n}'') \rho_{NL}(\mathbf{n}'') : . \quad (3.22)$$

Here the $::$ symbol takes the usual normal ordering definition, where all creation operators are on the left side of annihilation operators. Normal ordering ensures that arbitrary products of annihilation and creation operators behave like the Grassmann variables². f_{s_L} is defined

²See section 3.4.2 for the definition.

with a real parameter s_L ,

$$f_{s_L}(\mathbf{n}) = \begin{cases} 1 & \text{if } |\mathbf{n}| = 0, \\ s_L & \text{if } |\mathbf{n}| = 1, \\ 0 & \text{otherwise;} \end{cases} \quad (3.23)$$

The one-pion exchange interaction is given by [48]

$$V_{OPEP} = -\frac{g_A^2}{8f_\pi^2} \sum_{\mathbf{n}, \mathbf{n}', S, S', I} : \rho_{S,I}(\mathbf{n}) f_{S,S'}(\mathbf{n} - \mathbf{n}') \rho_{S',I}(\mathbf{n}') :, \quad (3.24)$$

where $f_{S,S'}$ is defined as

$$f_{S,S'}(\mathbf{n} - \mathbf{n}') = \frac{1}{L^3} \sum_{\mathbf{q}} \frac{\exp[-i\mathbf{q} \cdot (\mathbf{n} - \mathbf{n}') - b_\pi \mathbf{q}^2] q_S q'_S}{\mathbf{q}^2 + m_\pi^2}, \quad (3.25)$$

and the parameter b_π is introduced to soften the divergent behavior at short distance. We take the pion mass to be $m_\pi = 134.98$ MeV and the pion decay constant to be $f_\pi = 92.2$ MeV. The free Hamiltonian on the lattice is taken to be [30]

$$\begin{aligned} H_{free} &= \frac{49}{12m} \sum_{\mathbf{n}} a^\dagger(\mathbf{n}) a(\mathbf{n}) - \frac{3}{4m} \sum_{\mathbf{n}, i} \sum_{\langle \mathbf{n} \mathbf{n}' \rangle_i} a^\dagger(\mathbf{n}') a(\mathbf{n}) \\ &+ \frac{3}{40m} \sum_{\mathbf{n}, i} \sum_{\langle\langle \mathbf{n} \mathbf{n}' \rangle\rangle_i} a^\dagger(\mathbf{n}') a(\mathbf{n}) \\ &- \frac{1}{180m} \sum_{\mathbf{n}, i} \sum_{\langle\langle\langle \mathbf{n} \mathbf{n}' \rangle\rangle\rangle_i} a^\dagger(\mathbf{n}') a(\mathbf{n}). \end{aligned} \quad (3.26)$$

where we consider the hopping terms up to third nearest neighbors along axes. Collecting all terms discussed above, the full Hamiltonian that contains lattice EFT LO interactions is

obtained as

$$H = H_{free} + V_0 + V_{OPE}. \quad (3.27)$$

For different nuclear systems, we choose the appropriate interactions.

3.4 Grassmann path integral

3.4.1 Path integral

The path integral in quantum mechanics, a generalization of the action principle of classical mechanics, describes the amplitude of overlap of two points in spacetime. In the early 19th century, Wiener process [31] was first introduced, named after Norbert Wiener, for solving problems in diffusion and Brownian motion. It formed the basis of the rigorous path integral formulation. Dirac extended the idea by the use of Lagrangians in quantum mechanics in his article [32]. Following that, a complete formulation [33] was developed by Feynman, who also generalized the formalism to quantum field theory. It provides a direct connection to Lagrangian density and is very useful in quantum theory and numerical calculations.

We start with quantum mechanics. The amplitude for a particle to propagate from a point q_I to a point q_F in time T is $\langle q_F | e^{-iHT} | q_I \rangle$, where $|q\rangle$ denotes the particle's quantum state. If we discretize the propagation time T into N segments with $\Delta t = T/N$, the amplitude becomes

$$\langle q_F | e^{-iHT} | q_I \rangle = \langle q_F | e^{-iH\Delta t} e^{-iH\Delta t} \dots e^{-iH\Delta t} | q_I \rangle. \quad (3.28)$$

We assume that the state $|q\rangle$ is normalized, and that the set of states $|q_j\rangle$ forms a complete

basis. We apply the identity $\int |q_j\rangle\langle q_j|dq_j = 1$ here and insert it between all time slices:

$$\begin{aligned} \langle q_F|e^{-iHT}|q_I\rangle &= \left(\prod_{j=1}^{N-1} \int dq_j \right) \langle q_F|e^{-iH\Delta t}|q_{N-1}\rangle \langle q_{N-1}|e^{-iH\Delta t}|q_{N-2}\rangle \times \dots \\ &\dots \times \langle q_2|e^{-iH\Delta t}|q_1\rangle \langle q_1|e^{-iH\Delta t}|q_I\rangle. \end{aligned} \quad (3.29)$$

Now we focus on one time slice, propagation from state $|q_j\rangle$ to $|q_{j+1}\rangle$ with the Hamiltonian $H = \hat{p}^2/2m + V(\hat{q})$. The potential is only a function of coordinates and we can write

$$\langle q_{j+1}|e^{-iH\Delta t}|q_j\rangle = \langle q_{j+1}|e^{-i\frac{\hat{p}^2}{2m}\Delta t}|q_j\rangle e^{-iV(q_j)\Delta t} \quad (3.30)$$

To calculate $\langle q_{j+1}|e^{-i\frac{\hat{p}^2}{2m}\Delta t}|q_j\rangle$, we insert an identity $\int \frac{dp}{2\pi} |p\rangle\langle p| = 1$ right before $|q_j\rangle$ and write

$$\begin{aligned} \langle q_{j+1}|e^{-i\frac{\hat{p}^2}{2m}\Delta t}|q_j\rangle &= \int \frac{dp}{2\pi} \langle q_{j+1}|e^{-i\frac{\hat{p}^2}{2m}\Delta t}|p\rangle \langle p|q_j\rangle \\ &= \int \frac{dp}{2\pi} e^{-i\Delta t(p^2/2m)} \langle q_{j+1}|p\rangle \langle p|q_j\rangle \\ &= \int \frac{dp}{2\pi} e^{-i\Delta t(p^2/2m)} e^{ip(q_{j+1}-q_j)}. \end{aligned} \quad (3.31)$$

Now we can replace \hat{p} by the eigenvalue p , and write the state $|q\rangle$ in momentum representation as a plane wave. The integral in the last step can be treated as a Gaussian integral and we obtain

$$\langle q_{j+1}|e^{-i\frac{\hat{p}^2}{2m}\Delta t}|q_j\rangle = \sqrt{\frac{-im}{2\pi\Delta t}} e^{\frac{im\Delta t}{2} \left(\frac{q_{j+1}-q_j}{\Delta t} \right)^2}. \quad (3.32)$$

Plugging Eq. (3.32) into Eq.(3.30) yields

$$\langle q_{j+1}|e^{-iH\Delta t}|q_j\rangle = \sqrt{\frac{-im}{2\pi\Delta t}} e^{\frac{im\Delta t}{2}\left(\frac{q_{j+1}-q_j}{\Delta t}\right)^2} e^{-iV(q_j)\Delta t}, \quad (3.33)$$

and Eq.(3.29) becomes

$$\begin{aligned} \langle q_F|e^{-iHT}|q_I\rangle &= \left(\frac{-im}{2\pi\Delta t}\right)^{N/2} \left(\prod_{k=1}^{N-1} \int dq_k\right) \\ &\times \exp\left\{i\Delta t \sum_{j=0}^{N-1} \left[\frac{m}{2}\left(\frac{q_{j+1}-q_j}{\Delta t}\right) - V(q_j)\right]\right\} \end{aligned} \quad (3.34)$$

with $q_0 = q_I$ and $q_N = q_F$. Now we go to the continuum limit $\Delta t \rightarrow 0$ and replace $\frac{q_{j+1}-q_j}{\Delta t}$ by \dot{q} , and $\Delta t \sum_{j=0}^{N-1}$ by $\int_0^T dt$ to obtain the path integral in the form

$$\langle q_F|e^{-iHT}|q_I\rangle = \int Dq(t) e^{iS[q(t)]}, \quad (3.35)$$

where we define the integral over paths as

$$\int Dq(t) = \lim_{N \rightarrow \infty} \left(\frac{-im}{2\pi\Delta t}\right)^{N/2} \left(\prod_{k=1}^{N-1} \int dq_k\right), \quad (3.36)$$

and

$$\exp\{iS[q(t)]\} = \exp\left\{i \int dt L(q, \dot{q}, t)\right\}. \quad (3.37)$$

The classical Lagrangian $L(q, \dot{q}, t)$ is $\frac{1}{2}m\dot{q}^2 - V(q)$. The final formula allows us to obtain $\langle q_F|e^{-iHT}|q_I\rangle$ – we can simply integrate over all possible paths $q(t)$ weighted by $e^{iS[q(t)]}$ and require $q(0) = q_I$ and $q(T) = q_F$. Now let us introduce the Euclidean-time path integral formulation. If we do a Wick rotation $it \rightarrow \tau$, each function of t now becomes a function of

τ , and we can rewrite the path integral as

$$\langle q_F | e^{H\tau} | q_I \rangle = \int Dq(t) e^{S_E[q(\tau)]}. \quad (3.38)$$

Eq. (3.36) and Eq. (3.37) become

$$\int Dq(\tau) = \lim_{N \rightarrow \infty} \left(\frac{m}{2\pi\Delta\tau} \right)^{N/2} \left(\prod_{k=1}^{N-1} \int dq_k \right) \quad (3.39)$$

and

$$\exp\{S[q(\tau)]\} = \exp\left\{ \int d\tau L(q, \dot{q}, \tau) \right\}. \quad (3.40)$$

The path integral formulation derived above can be applied to quantum field theory by the mapping shown in the following table³,

$q \rightarrow \varphi$
$\int Dq(t) \rightarrow \int D\varphi$
$i \int dt L(q, \dot{q}, t) \rightarrow i \int d^{dim}x \mathcal{L}(\varphi)$

and we write the path integral as follows

$$\mathcal{Z} = \int D\varphi e^{i \int d^{dim}x \mathcal{L}(\varphi)}. \quad (3.41)$$

Here we introduce a field φ , which is the dynamic variable in quantum field theory while the position is not a dynamic variable. In 3rd row of the table, x denotes the generalized coordinates, where the time is incorporated as one dimension. Therefore, $\mathcal{L}(\varphi)$ in the integral is the Lagrangian density.

³See Ref. [34] for rigorous derivation and detailed discussion

3.4.2 Grassmann variables

Grassmann variables (or numbers) are generated by anti-commuting elements or objects. If we define θ_i and θ_j as two different Grassmann variables, they have the following properties:

$$\theta_i\theta_j = -\theta_j\theta_i \quad \text{and} \quad \theta_i^2 = 0. \quad (3.42)$$

In short, the above relations can be expressed as the anti-commutation relation between Grassmann variables,

$$\{\theta_i, \theta_j\} = 0, \quad (3.43)$$

which is consistent with theory of fermionic fields, while bosonic fields obey commutation relation. Therefore, the path integral of Fermi systems that we are interested in is built upon Grassmann variables. In order to construct the Grassmann integral, we introduce some basic relations here. Consider a general function of the form $\sum_i c_i f_i(\theta)$, and calculate the integral $\int \sum_i c_i f_i(\theta) d\theta$. In the simplest case, we have

$$\int \theta d\theta = 1 \quad \text{and} \quad \int 1 d\theta = 0. \quad (3.44)$$

More complicated homogeneous functions will always either be equivalent to a constant or a linear function of θ . Therefore,

$$\int \frac{\partial f(\theta)}{\partial \theta} d\theta = 0. \quad (3.45)$$

3.4.3 Grassmann path integral without auxiliary field

Let us define c_i^* and c_i as the Grassmann fields for spin i on the lattice. The Grassmann fields are periodic along \hat{x} , \hat{y} and \hat{z} directions, respectively, in $L \times L \times L$ lattice.

$$c_i(\mathbf{n} + L\hat{x}, n_t) = c_i(\mathbf{n} + L\hat{y}, n_t) = c_i(\mathbf{n} + L\hat{z}, n_t) = c_i(\mathbf{n}, n_t) \quad (3.46)$$

and anti-periodic along the temporal direction,

$$c_i(\mathbf{n}, n_t + L_t) = -c_i(\mathbf{n}, n_t). \quad (3.47)$$

We define the Grassmann spin densities,

$$\rho_\sigma(n, n_t) = c_\sigma^*(n, n_t)c_\sigma(n, n_t), \quad (3.48)$$

and denote the spin species by σ . We consider the following Grassmann path integral

$$\mathcal{Z} = \int DcDc^* \exp[-S(c, c^*)], \quad (3.49)$$

where the integral over all possible paths is

$$DcDc^* = \prod_{\mathbf{n}, n_t, \sigma=\uparrow, \downarrow} dc_\sigma(\mathbf{n}, n_t)dc_\sigma^*(\mathbf{n}, n_t), \quad (3.50)$$

and the action is

$$S(c, c^*) = S_{free}(c, c^*) + c_0\alpha_t \sum_{\mathbf{n}, n_t} \rho_\uparrow(\mathbf{n}, n_t)\rho_\downarrow(\mathbf{n}, n_t). \quad (3.51)$$

The first term in $S(c, c^*)$ is the free fermion action,

$$\begin{aligned}
S_{free}(c, c^*) &= \sum_{\mathbf{n}, n_t, \sigma=\uparrow, \downarrow} [c_\sigma^*(\mathbf{n}, n_t) c_\sigma(\mathbf{n}, n_t + 1) - (1 - 6\frac{\alpha_t}{2m}) c_\sigma^*(\mathbf{n}, n_t) c_\sigma(\mathbf{n}, n_t)] \\
&\quad - \frac{\alpha_t}{2m} \sum_{\mathbf{n}, n_t, \sigma=\uparrow, \downarrow} \sum_{l=x, y, z} [c_i^*(\mathbf{n}, n_t) c_i(\mathbf{n} + \hat{l}, n_t) + c_i^*(\mathbf{n}, n_t) c_i(\mathbf{n} - \hat{l}, n_t)],
\end{aligned} \tag{3.52}$$

and the last term is an attractive contact interaction between opposite spins with strength c_0 .

Now we focus on the calculation of the Grassmann path integral in Eq. (3.49). According to Ref. [35, 36], we can convert a path integral to the trace of a product of transfer matrix operators along temporal direction, as follows

$$\begin{aligned}
&Tr \left\{ : F_{L_t-1} [a_{\sigma'}^\dagger(\mathbf{n}'), a_\sigma(\mathbf{n})] : \cdots \cdots : F_0 [a_{\sigma'}^\dagger(\mathbf{n}'), a_\sigma(\mathbf{n})] : \right\} \\
&= \int Dc Dc^* \exp \left\{ \sum_{n_t=0}^{L_t-1} \sum_{\mathbf{n}, \sigma} c_\sigma^*(\mathbf{n}, n_t) [c_\sigma(\mathbf{n}, n_t) - c_\sigma(\mathbf{n}, n_t + 1)] \right\} \\
&\quad \times \prod_{n_t=0}^{L_t-1} F_{n_t} [c_{\sigma'}^*(\mathbf{n}, n_t), c_\sigma(\mathbf{n}, n_t)],
\end{aligned} \tag{3.53}$$

where $c_\sigma(\mathbf{n}, L_t) = -c_\sigma(\mathbf{n}, 0)$. The operators $F_{n_t} [c_{\sigma'}^*(\mathbf{n}, n_t), c_\sigma(\mathbf{n}, n_t)]$ and $F_{n_t} [a_{\sigma'}^\dagger(\mathbf{n}'), a_\sigma(\mathbf{n})]$ have exactly same functional form. We define $a_\sigma^\dagger(\mathbf{n}) [a_\sigma(\mathbf{n})]$ as the fermionic annihilation (creation) operator of spin σ at lattice site \mathbf{n} . Let us define a free Hamiltonian on a three-dimensional lattice

$$\begin{aligned}
H_{free} &= \frac{3}{m} \sum_{\mathbf{n}, \sigma=\uparrow, \downarrow} a_\sigma^\dagger(\mathbf{n}) a_\sigma(\mathbf{n}) \\
&\quad - \frac{1}{2m} \sum_{\mathbf{n}, \sigma=\uparrow, \downarrow} \sum_{l=x, y, z} [a_\sigma^\dagger(\mathbf{n}) a_\sigma(\mathbf{n} + \hat{l}) + a_\sigma^\dagger(\mathbf{n}) a_\sigma(\mathbf{n} - \hat{l})]
\end{aligned} \tag{3.54}$$

with densities denoted by

$$\rho_{\sigma}^{a\dagger a}(\mathbf{n}) = a_{\sigma}^{\dagger}(\mathbf{n})a_{\sigma}(\mathbf{n}). \quad (3.55)$$

This Hamiltonian corresponds to the second term in the free fermion action (Eq. (3.52)). In our simulations, we use the free Hamiltonian in Eq. (3.26) to reduce the effect of finite lattice spacing. Therefore, the corresponding free fermion action shall contain the hopping terms of up to third nearest neighbors along axes. Following Eq. (3.53), the path integral can be expressed as

$$\mathcal{Z} = Tr(M^{Lt}), \quad (3.56)$$

where M is the transfer matrix operator in normal ordering

$$M =: \exp \left[-H_{free}\alpha_t - c_0\alpha_t \sum_{\mathbf{n}} \rho_{\uparrow}^{a\dagger a}(\mathbf{n})\rho_{\downarrow}^{a\dagger a}(\mathbf{n}) \right] :. \quad (3.57)$$

3.4.4 Grassmann path integral with auxiliary field

We introduce an auxiliary field $s(\mathbf{n}, n_t)$ that is real-valued and define a Grassmann action with the auxiliary field s ,

$$S(c, c^*, s) = S_{free}(c, c^*) - \sum_{\mathbf{n}, n_t} A[s(\mathbf{n}, n_t)] \cdot [\rho_{\uparrow}(\mathbf{n}, n_t) + \rho_{\downarrow}(\mathbf{n}, n_t)]. \quad (3.58)$$

and $A[s(\mathbf{n}, n_t)]$ is defined as

$$A[s(\mathbf{n}, n_t)] = \sqrt{-C\alpha_t} s(\mathbf{n}, n_t). \quad (3.59)$$

Therefore, the Grassmann path integral becomes

$$\mathcal{Z} = \prod_{\mathbf{n}, n_t} \left[\int \mathcal{D}s(\mathbf{n}, n_t) \right] \int Dc Dc^* \exp[-S(c, c^*, s)]. \quad (3.60)$$

We use a Gaussian-integral transformation similar to the original Hubbard-Stratonovich transformation [37, 38]

$$\int \mathcal{D}s(\mathbf{n}, n_t) = \frac{1}{\sqrt{2\pi}} \int_{-\infty}^{\infty} ds(\mathbf{n}, n_t) e^{-\frac{1}{2}s^2(\mathbf{n}, n_t)}, \quad (3.61)$$

It is straightforward to prove that

$$\int \mathcal{D}s(\mathbf{n}, n_t) 1 = 1, \quad (3.62)$$

$$\int \mathcal{D}s(\mathbf{n}, n_t) A[s(\mathbf{n}, n_t)] = 0. \quad (3.63)$$

Using the two identities above we will show that the new Grassmann action is equivalent to the one in Eq. (3.51) if $C = c_0$. The first term is still $S_{free}(c, c^*)$ and we consider the integral of the second term in the new Grassmann action,

$$\begin{aligned} \int \mathcal{D}s \exp [A(s) \cdot (\rho_{\uparrow} + \rho_{\downarrow})] &= \int Ds [1 + A(s)(\rho_{\uparrow} + \rho_{\downarrow}) + A^2(s)\rho_{\uparrow}\rho_{\downarrow}] \\ &= 1 + \int \mathcal{D}s A^2(s)\rho_{\uparrow}\rho_{\downarrow} = \exp \left[\int \mathcal{D}s A^2(s)\rho_{\uparrow}\rho_{\downarrow} \right]. \end{aligned} \quad (3.64)$$

Since $\int \mathcal{D}s A^2(s) = -C\alpha_t$, setting $C = c_0$ indeed yields a path integral that is equivalent to Eq. (3.49) in which there is no auxiliary fields. Using Eq. (3.53), we can rewrite the path integral as the trace of a product of transfer matrix operators that depend on the auxiliary

field $s(\mathbf{n}, n_t)$,

$$\mathcal{Z} = \prod_{\mathbf{n}, n_t} \left[\int \mathcal{D}s(\mathbf{n}, n_t) \right] Tr\{M(s, L_t - 1) \cdots M(s, 0)\}, \quad (3.65)$$

where

$$M(s, n_t) =: \exp \left\{ -H_{free} \alpha_t + \sum_{\mathbf{n}} A[s(\mathbf{n}, n_t)] \cdot \left[\rho_{\uparrow}^{a\dagger} a(\mathbf{n}) + \rho_{\downarrow}^{a\dagger} a(\mathbf{n}) \right] \right\} :. \quad (3.66)$$

Let $|\Phi_{N,N}^{0,free}\rangle$ be the initial state, which is a normalized Slater-determinant for the ground state of a non-interacting system of N up spins and N down spins. Then the Euclidean time projection amplitude can be written as⁴

$$Z_{N,N}(t) = \prod_{\mathbf{n}, n_t} \left[\int \mathcal{D}s(\mathbf{n}, n_t) \right] \left\langle \Phi_{N,N}^{0,free} \left| M(s, L_t - 1) \cdots M(s, 0) \right| \Phi_{N,N}^{0,free} \right\rangle, \quad (3.67)$$

where $t = L_t \alpha_t$ is the projection time. Due to the normal ordering, the transfer matrix contains only one-body operators that interact with the background auxiliary field and there is no direct interaction between particles. Using the properties of determinants, we can write

$$\left\langle \Phi_{N,N}^{0,free} \left| M(s, L_t - 1) \cdots M(s, 0) \right| \Phi_{N,N}^{0,free} \right\rangle = det[\mathcal{M}_{\uparrow}(s, t)] det[\mathcal{M}_{\downarrow}(s, t)], \quad (3.68)$$

where

$$\left[\mathcal{M}_{\sigma}(s, t) \right]_{k,k'} = \left\langle \mathbf{p}_{\sigma,k} \left| M(s, L_t - 1) \cdots M(s, 0) \right| \mathbf{p}_{\sigma,k'} \right\rangle, \quad (3.69)$$

with matrix indices $k, k' = 1, \dots, N$. $|\mathbf{p}_{\sigma,k}\rangle$ and $|\mathbf{p}_{\sigma,k'}\rangle$ are the single-particle momentum states with spin σ . If we fill the momentum space with particles in exactly the same way for

⁴See details in section 3.4

two spin species, it is clear that $|\mathbf{p}_{\uparrow,k}\rangle = |\mathbf{p}_{\downarrow,k}\rangle$. Consequently, the path integral becomes

$$Z_{N,N}(t) = \prod_{\mathbf{n}, n_t} \left[\int \mathcal{D}s(\mathbf{n}, n_t) \right] \left\{ \det[\mathcal{M}_{\uparrow}(s, t)] \right\}^2 \quad (3.70)$$

due to $\det[\mathcal{M}_{\uparrow}(s, t)] = \det[\mathcal{M}_{\downarrow}(s, t)]$. It is clear that \mathcal{M}_{σ} is Hermitian, so $\det[\mathcal{M}_{\sigma}]$ is real. Therefore, the square of the determinant is non-negative and we do not encounter sign oscillations here. In our simulations in the unitary limit, we use the interaction mentioned in Sec. 3.2 with a smeared nonlocal density ρ_{NL} . The auxiliary field $s(\mathbf{n}, n_t)$ and $\rho_{\sigma, NL}(\mathbf{n})$ couple to form the nonlocal interaction term $V_{\sigma, NL}$ and a quadratic term is generated by the auxiliary field itself,

$$V_{\sigma, NL}^s = \sqrt{-c} \sum_{\mathbf{n}, \mathbf{n}'} s(\mathbf{n}) f_{sL}(\mathbf{n} - \mathbf{n}') \rho_{\sigma, NL}(\mathbf{n}') \quad \text{and} \quad V_{NL}^{ss} = \frac{1}{2} s^2. \quad (3.71)$$

Consequently, the transfer matrix operator with respect to spin σ can be written as

$$M_{\sigma}(s, n_t) =: \exp[-H_{free}\alpha t - V_{\sigma, NL}\sqrt{\alpha t}] :. \quad (3.72)$$

and the quadratic term V_{NL}^{ss} of the auxiliary field is contained in the integral $\int \mathcal{D}s(\mathbf{n}, n_t)$ by its definition (see Eq. (3.61)).

3.5 Euclidean time projection method

3.5.1 Time projection operator

In quantum mechanics, the time evolution operator is $e^{-iH\Delta t}$ for a given Hamiltonian H , which evolves the state $|\Phi(t)\rangle$ to the state $|\Phi(t + \Delta t)\rangle$ in time. By setting $\Delta t = -i\Delta\tau$,

the time evolution operator becomes $e^{-H\Delta\tau}$. Since τ is the time in Euclidean space, the operator is called Euclidean time projection operator or imaginary time evolution operator. This transformation allows us to find the lowest-energy state of the physics system with a given Hamiltonian. Consider the eigenvalues and eigenstates of H , which are not known a priori:

$$H|\psi_j\rangle = E_j|\psi_j\rangle, \quad (3.73)$$

with $j = 0, 1, \dots$. E_0 is the ground-state energy. Here, each eigenstate could have some degeneracy, but we do not distinguish the degenerate states. If we want to find the lowest-energy state, $|\psi_0\rangle$, we can choose an almost arbitrary state $|\Psi_I\rangle$ as an initial wave function and expand it in the complete basis $\{|\psi_0\rangle, |\psi_1\rangle, \dots\}$,

$$|\Psi_I\rangle = \sum_{j=0} c_j |\psi_j\rangle. \quad (3.74)$$

We then let $e^{-H\Delta\tau}$ act on the initial state $|\Psi_I\rangle$ and obtain

$$e^{-H\Delta\tau}|\Psi_I\rangle = \sum_{j=0} c_j e^{-E_j\Delta\tau} |\psi_j\rangle. \quad (3.75)$$

and the normalized form can be written as

$$\frac{\sum_{j=0} c_j e^{-E_j\Delta\tau} |\psi_j\rangle}{\sqrt{\sum_{j=0} |c_j|^2 e^{-2E_j\Delta\tau}}}. \quad (3.76)$$

If $c_0 (= \langle \psi_0 | \Psi_I \rangle)$ is nonzero, the coefficient of $|\psi_0\rangle$ dominates when $\Delta\tau$ is large enough, and in the limit of infinite projection time, we obtain

$$|\psi_0\rangle = \lim_{\Delta\tau \rightarrow \infty} e^{-H\Delta\tau} |\Psi_I\rangle. \quad (3.77)$$

It is the exponentially-evolved coefficient of $|\psi_j\rangle$ that matters and the lowest-energy eigenstate has the largest coefficient at infinite $\Delta\tau$. Besides calculating the ground state, we can project out the first-excited state in the case of $c_0 = 0$ and $c_1 \neq 0$. In addition, some constraints can be applied to the initial wave function, allowing wide applications. If $|\Psi_I\rangle$ is, for instance, chosen to be spherically symmetric, using Euclidean time projection we can find the lowest-energy state with spherical symmetry.

3.5.2 Asymptotic behavior of observable

Let us define t as the total projection time and study the asymptotic behavior of the observables using the Euclidean time projection method. For an interacting system with the same particle number for two spin species, we label the energy eigenstates by $|\Psi_{N,N}^k\rangle$ with eigenvalues $E_{N,N}^k$ in nondecreasing order,

$$E_{N,N}^0 \leq E_{N,N}^1 \cdots \leq E_{N,N}^k \cdots, \quad (3.78)$$

where N, N denotes the particle number for up and down spins. The overlap between the energy eigenstate and free fermion ground state is defined as $c_{N,N}^k$,

$$c_{N,N}^k = \langle \Psi_{N,N}^k | \Phi_{N,N}^{0,free} \rangle, \quad (3.79)$$

and we assume $c_{N,N}^0$ is nonzero. In the transfer matrix formalism, the Hamiltonian is the logarithm of the transfer matrix and we have the following eigenvalue equations:

$$M|\Psi_{N,N}^k\rangle = e^{-E_{N,N}^k\alpha_t}|\Psi_{N,N}^k\rangle. \quad (3.80)$$

To study the asymptotic behavior of the estimated ground-state energy as a function of projection time t , we define the transient energy expectation value

$$E_{N,N}(t) = \alpha_t^{-1} \ln \frac{Z_{N,N}(t - \alpha_t)}{Z_{N,N}(t)}. \quad (3.81)$$

We perform a spectral decomposition of $Z_{N,N}(t)$ in terms of energy eigenstates,

$$Z_{N,N}(t) = \sum_{k=0}^{\infty} |c_{N,N}^k|^2 e^{-E_{N,N}^k t}, \quad (3.82)$$

and at large t the low-energy eigenstates have more significant contributions. For $t \rightarrow \infty$ we find

$$E_{N,N}(t) \approx E_{N,N}^0 + \sum_{k \neq 0} \left| \frac{c_{N,N}^k}{c_{N,N}^0} \right|^2 \alpha_t^{-1} [e^{(E_{N,N}^k - E_{N,N}^0)\alpha_t} - 1] e^{-(E_{N,N}^k - E_{N,N}^0)t}. \quad (3.83)$$

The excitation energy $E_{N,N}^k - E_{N,N}^0$ for low-energy states are small compared to the energy cutoff scale α_t^{-1} . Therefore,

$$E_{N,N}(t) \approx E_{N,N}^0 + \sum_{k \neq 0} \left| \frac{c_{N,N}^k}{c_{N,N}^0} \right|^2 (E_{N,N}^k - E_{N,N}^0) e^{-(E_{N,N}^k - E_{N,N}^0)t}. \quad (3.84)$$

This equation manifests the asymptotic behavior that the transient energy is $E_{N,N}^0$ plus the contributions from excited states that decay with projection time. There always exists a time t' , from which onward, the contributions from states with $k > 1$ are negligible compared to that from $k = 1$, the first excited state. The asymptotic behavior of transient energy expectation value takes the form of

$$E_{N,N}(t) = E_{N,N}^0 + be^{-\eta t}, \quad (3.85)$$

where $\eta = E_{N,N}^1 - E_{N,N}^0$. In different runs of the simulations, we set different projection times. In Fig. 3.2, we show the measurements of ground-state energies versus the projection time t for various box sizes with $L = 5, 6, 10, 11$. For each box size, curve is fitted by the exponential function above and $E_{N,N}^0$ is found as the ground state energy.

In the calculations of the energies, the transfer matrix operator commutes with the Hamiltonian. Now consider the asymptotic behavior of $\langle O \rangle(t)$ for an operator that does not commute with H . We start with the asymptotic form of the wave function

$$|\Psi_{N,N}(t)\rangle \approx c_0 e^{-E_{N,N}^0 t} |\Psi_{N,N}^0\rangle + c_1 e^{-E_{N,N}^1 t} |\Psi_{N,N}^1\rangle \quad (3.86)$$

Without generating confusion, we use c_k instead of $c_{N,N}^k$ in this equation and the following equations. We insert the operator O at some time between t_1 and t_2 , and measure the observable

$$\langle O \rangle(t_1, t_2) = \frac{\langle \Psi_{N,N}(t_1) | O | \Psi_{N,N}(t_2) \rangle}{\langle \Psi_{N,N}(t_1) | \Psi_{N,N}(t_2) \rangle}, \quad (3.87)$$

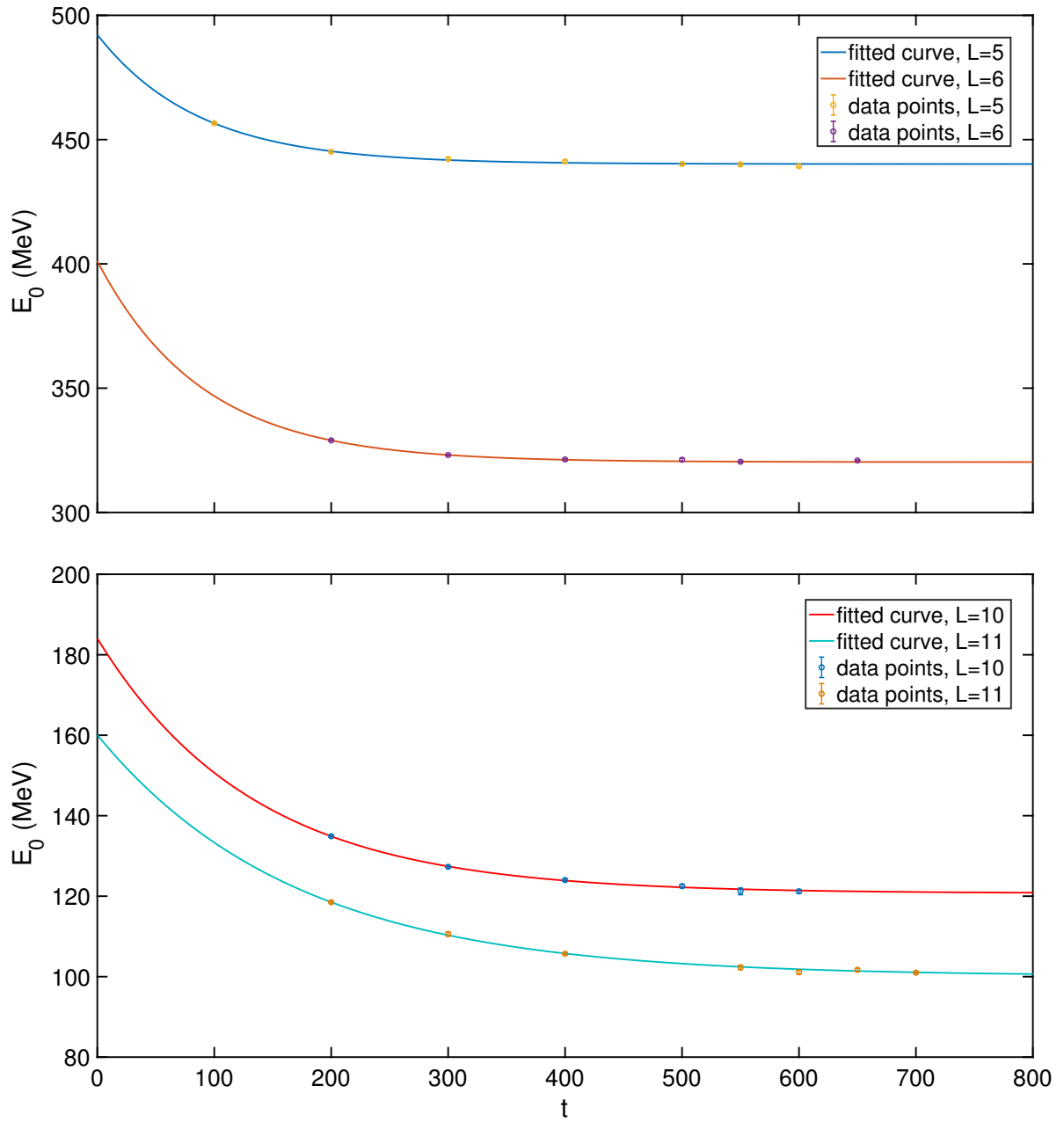


Figure 3.2: Ground-state energies for $L = 5, 6$ (upper panel) and $10, 11$ (lower panel) versus projection time t . The data points are fitted using the function Eq. (3.85). The projection time is in dimensionless lattice units.

where $t_1 + t_2 = t$. According to Eq. (3.86), we have

$$\begin{aligned} \langle O \rangle(t_1, t_2) &= O_{00} + O_{01} e^{-\left(E_{N,N}^1 - E_{N,N}^0\right)t_2} \\ &+ O_{10} e^{-\left(E_{N,N}^1 - E_{N,N}^0\right)t_1} + O_{11} e^{-\left(E_{N,N}^1 - E_{N,N}^0\right)(t_1+t_2)} + \dots, \end{aligned} \quad (3.88)$$

where

$$O_{00} = \langle \Psi_{N,N}^0 | O | \Psi_{N,N}^0 \rangle \quad (3.89)$$

$$O_{01} = \frac{c_0^* c_1}{|c_0|^2} \langle \Psi_{N,N}^0 | O | \Psi_{N,N}^1 \rangle \quad (3.90)$$

$$O_{10} = \frac{c_1^* c_0}{|c_0|^2} \langle \Psi_{N,N}^1 | O | \Psi_{N,N}^0 \rangle \quad (3.91)$$

$$O_{11} = \frac{|c_1|^2}{|c_0|^2} (\langle \Psi_{N,N}^1 | O | \Psi_{N,N}^1 \rangle - \langle \Psi_{N,N}^0 | O | \Psi_{N,N}^0 \rangle). \quad (3.92)$$

Therefore, the asymptotic form of the observable's expectation value is

$$\langle O \rangle(\tau) = \langle \Psi_{N,N}^0 | O | \Psi_{N,N}^0 \rangle + c e^{-\left(E_{N,N}^1 - E_{N,N}^0\right)\tau} + d e^{-\left(E_{N,N}^1 - E_{N,N}^0\right)t} \quad (3.93)$$

and $\tau = \min\{t_1, t_2\}$. To reach the fastest convergence, the best choice of τ is $t/2$ which requires $t_1 = t_2 = t/2$. In the following, we take a two-body operator as an example to show how well Eq. (3.93) describes the asymptotic behavior of $\langle O \rangle(t)$. We consider the following operator on the lattice,

$$O =: a_{\uparrow}^{\dagger}(\mathbf{r}'_1) a_{\downarrow}^{\dagger}(\mathbf{r}'_2) a_{\uparrow}(\mathbf{r}_1) a_{\downarrow}(\mathbf{r}_2) :, \quad (3.94)$$

and calculate it by [24],

$$O = \frac{\partial^2}{\partial \epsilon_1 \partial \epsilon_2} M(\epsilon_1, \epsilon_2), \quad (3.95)$$

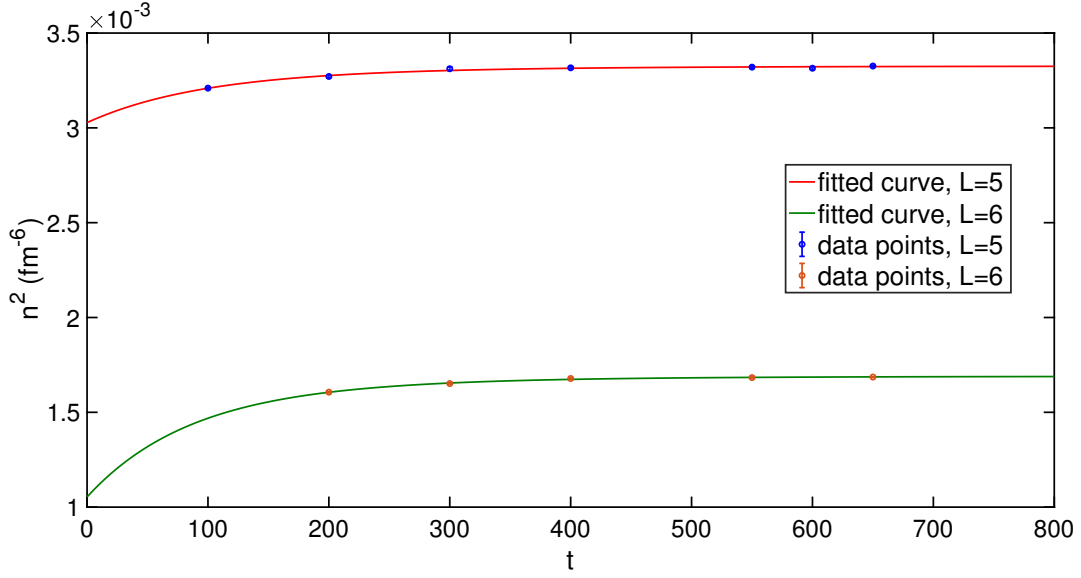


Figure 3.3: Two-body density versus projection time t for $L = 5, 6$. The data points are fitted by the function in form of Eq. (3.93). The projection time is in dimensionless lattice units.

where

$$M(\epsilon_1, \epsilon_2) =: \exp[\epsilon_1 a_{\uparrow}^{\dagger}(\mathbf{r}'_1) a_{\uparrow}(\mathbf{r}_1) + \epsilon_2 a_{\downarrow}^{\dagger}(\mathbf{r}'_2) a_{\downarrow}(\mathbf{r}_2)] : . \quad (3.96)$$

This is convenient because the matrix $M(\epsilon_1, \epsilon_2)$ looks like a transfer matrix of only one-body operators. We measure the two-body density $n^2 = \langle a_{\uparrow}^{\dagger}(0) a_{\downarrow}^{\dagger}(0) a_{\uparrow}(0) a_{\downarrow}(0) \rangle$ at each time step and show the result versus the projection time t in Fig. 3.3. The data points are fitted using the function Eq. (3.93). Since the excitation energy $E_{N,N}^1 - E_{N,N}^0$ is known from the ground-state energy fit, we only have three unknown parameters to be estimated. In the limit of an infinite projection time, the fitted curves show clear convergence and thus $\langle O \rangle(\infty)$ is a good estimate of $\langle \Psi_{N,N}^0 | O | \Psi_{N,N}^0 \rangle$. In general, calculating the observable's expectation value in the lowest-energy state of interest requires the extrapolation towards an infinite projection time.

3.6 Numerical methods

3.6.1 Monte Carlo methods

Monte Carlo (MC) algorithms⁵ are widely used computational techniques for calculating the numerical results if the problem at hand is deterministic in principle. By repeatedly generating random samples that might traverse all possibilities in the relevant phase space, the statistical average of the sampling can yield a good numerical evaluation of a problem's solution. Monte Carlo methods are used in three classes of problem – numerical integration, optimization, and generating samples from a distribution function.

In physics problems, we often use MC to calculate multi-dimensional integrals or expectation values of observables when the state of a system is not analytically known. For example, we might want to calculate the expectation value of an operator O in some unnormalized state $\Psi(x_1, x_2, \dots, x_n)$ via

$$\frac{\int \int \cdots \int \langle \Psi(x_1, x_2, \dots, x_n) | O | \Psi(x_1, x_2, \dots, x_n) \rangle dx_1 dx_2 \cdots dx_n}{\int \int \cdots \int \langle \Psi(x_1, x_2, \dots, x_n) | \Psi(x_1, x_2, \dots, x_n) \rangle dx_1 dx_2 \cdots dx_n}. \quad (3.97)$$

We can repeatedly generate samples for x_1, x_2, \dots, x_n , respectively, until the estimated result converges with a good variance. Furthermore, if the state $|\Psi(x_1, x_2, \dots, x_n)\rangle$ is difficult to calculate due to the complexity of system, we can still sample from the distribution of all possible states for a given Hamiltonian. In this chapter, we will introduce the basic techniques that are used in our Monte Carlo simulations and the ideas behind them.

⁵See Refs. [39–42] for details of Monte Carlo methods, theorems, proofs and a full list of references.

3.6.2 Importance sampling

To calculate an integral $\int f(x)dx$, we can always transform it to the following form, assuming $g(x) \neq 0$:

$$\int \frac{f(x)}{g(x)}g(x)dx. \quad (3.98)$$

If $g(x)$ is a probability function with input x , we can estimate the integral by generating samples from $g(x)$ and dividing the summation by the total number of sample points n . This quantity will converge to the value of the original integral as n goes to infinity,

$$\int f(x)dx = \lim_{N \rightarrow \infty} \frac{1}{N} \sum_{i=1}^N \frac{f(x_i)}{g(x_i)}. \quad (3.99)$$

Note that the function $g(x)$ provides a distribution of the sample points x_i . A good choice of $g(x)$ will have a similar shape to $f(x)$, so that we will spend more time on generating samples x_i with larger values of $f(x_i)$. In this way, important contributions from large-valued $f(x_i)$ are taken into account first and thus the numerical summation will converge more rapidly, and with small variance.

The variance of the estimate depends on the quality of the pseudo-random number generator and on how similar the importance function is to the integrand. In general, the variance of our estimate decreases as $\frac{1}{N}$, i.e. more sample points yields better results. An appealing feature is that we are able to sample in parallel according to Eq. (3.99) in groups of independent threads and then calculate the average over the independent estimates.

3.6.3 Markov chain

Importance sampling provides a way to generate samples from specifically chosen probability functions. We introduce Markov chain or Markov process here to solve the problem when we don't know the probability function upfront, but the transition probability is given between any pair of states of the system. Suppose we have an ensemble of states in the phase space, labeled by A, B, C, \dots . The transition probability, for instance, from state A to state B is denoted by $q(B|A)$ and it only depends on the two states involved. The constraint is $\sum_X q(X|Y) = 1$ by conservation of the probability for any state Y. In matrix form, the transition probability matrix is

$$Q = \begin{pmatrix} q(A|A) & q(A|B) & \dots & q(A|X) & \dots \\ q(B|A) & q(B|B) & \dots & q(B|X) & \dots \\ \vdots & \vdots & & \vdots & \\ q(X|A) & q(X|B) & \dots & q(X|X) & \dots \\ \vdots & \vdots & & \vdots & \end{pmatrix} \quad (3.100)$$

We start from an initial distribution of states $\Pi^{(0)} = [\pi^{(0)}(A), \pi^{(0)}(B), \dots]^T$ at $t = 0$ with $\sum_X \pi^{(t)}(X) = 1$. The distribution at $t = 1$, obviously, is $\Pi^{(1)} = Q * \Pi^{(0)}$. The partition of states at time t is $\Pi^{(t)} = Q * \Pi^{(t-1)} = \dots = Q^t * \Pi^{(0)}$. Applying this chain to a known partition at a given time step, we can generate the partition at any later time. When t goes to infinity, it will reach a stationary partition which satisfies $\Pi^{(t)} = \Pi^{(t-1)}$. This partition

is will be an eigenvector of the matrix Q with unit eigenvalue. We denote $\Pi^{(t)}$ as Π in the stationary case. Clearly, it is a dynamic equilibrium where $\pi(X)q(Y|X) = \pi(Y)q(X|Y)$ for any pair of X and Y . This is also called detailed balance. In continuous state space, the equation still holds.

3.6.4 Metropolis algorithm

In practice, it is difficult to find a transition matrix (or function), but the Markov chain process provides us a really useful way to generate samples. Given an initial sample, we can use this chain to generate an infinite number of samples. In order to reduce the variance while sampling, we might want to keep only the good samples and throw away the bad ones. The Metropolis method can provide us with a criterion for acceptance or rejection.

Suppose we generate samples according to certain function $p(x)$ and we also have a proposal function $q(x^{*(t)}|x^{(t-1)})$ that connects the current step and the proposed step with sample x^* . At time step $t - 1$, we use the proposal function to generate a proposed sample point at step t and then use the following criterion to accept or reject the new sample:

1. $p(x^{*(t)}) \geq p(x^{(t-1)})$, we accept the proposed sample point and $x^{(t)} = x^{*(t)}$;
2. $p(x^{*(t)}) < p(x^{(t-1)})$, we accept the proposed sample with a probability $\frac{p(x^{*(t)})}{p(x^{(t-1)})}$.

Since each step of movement only involves two states, we can drop the superscript t and $t - 1$ in the following. In short, the accept/reject criterion is that we accept the proposed sample with a probability $\alpha = \min\left(1, \frac{p(x^*)}{p(x)}\right)$. In practice, we generate a random number r from a uniform distribution $U[0, 1]$. If $r \leq \alpha$, x^* is accepted, otherwise, x^* is rejected and we generate a new x^* . In this way, we can generate samples according to the distribution $p(x)$ [43].

Notice that we do not require $p(x)$ to be normalized, since α is the ratio between $p(x^*)$ and $p(x)$, but we expect $p(x)$ to be positive. In order to satisfy the condition of detailed balance – $\pi(X)q(Y|X)\alpha_{YX} = \pi(Y)q(X|Y)\alpha_{XY}$, the proposal function must be symmetric, where α_{YX} is the probability of accepting the proposed configuration Y . To use an asymmetric proposal function, we need the following modifications on the previous accept/reject criterion:

1. Calculate the proposal correction factor $c = \frac{q(x|x^*)}{q(x^*|x)}$;
2. Now α is defined as $\alpha = \min\left(1, \frac{p(x^*)}{p(x)} \times c\right)$.

Other parts of the Metropolis method are unchanged and the detailed balance condition still holds. This new version of Metropolis method is called Metropolis-Hastings algorithm [43].

3.6.5 Weighted average calculation

Let us now revisit the importance sampling, but apply it to the calculation of an average $\frac{\int_a^b f(x)dx}{\int_a^b dx}$. We introduce the importance function $g(x)$ and do the following substitution,

$$\frac{\int_a^b f(x)dx}{\int_a^b dx} = \frac{\int_a^b \frac{f(x)}{g(x)}g(x)dx}{\int_a^b \frac{1}{g(x)}g(x)dx}. \quad (3.101)$$

The right hand side of the above equation can be understood as generating samples according to $g(x)$ and the integrand becomes $f(x)/g(x)$. In discretized form, we have

$$\frac{\int_a^b f(x)dx}{\int_a^b dx} = \frac{\sum_{i=1}^N \frac{f(x_i)}{g(x_i)}}{\sum_{i=1}^N \frac{1}{g(x_i)}}. \quad (3.102)$$

Using the Metropolis or the Metropolis-Hastings algorithms, any appropriate $g(x)$ we choose should be real and non-negative, otherwise $g(x)$ can not be used as the weight to do importance sampling.

3.6.6 The sign problem

Sign problem (or numerical sign problem) is one of the major unsolved problems in the physics of many-body systems, like nuclear physics, condensed physics, and quantum field theory. In this section, we will illustrate the sign problem in the context of the auxiliary-field path integral discussed in section 3.3 this chapter. We calculate the expectation value of the observable O , as follows

$$\langle O \rangle = \frac{\int O(s)Z(s)ds}{\int Z(s)ds}. \quad (3.103)$$

Here s denotes the real-valued auxiliary field on the lattice. We write the result of the path integral as $Z(s)$, which is still a function of the auxiliary field $s(n, n_t)$. Since we are dealing with a system of fermions at nonzero chemical potential, $Z(s)$ in general is a complex number. Thus, it is not possible to use $Z(s)$ as the weight in importance sampling. We can use the reweighting procedure and write

$$\langle O \rangle = \frac{\int O(s)|Z(s)|e^{i\theta(s)}ds}{\int |Z(s)|e^{i\theta(s)}ds} = \frac{\sum O(s)e^{i\theta(s)}}{\sum e^{i\theta(s)}} \quad (3.104)$$

with $Z(s) = |Z(s)|e^{i\theta}$. Now $|Z(s)|$ is non-negative and the summations are made according to sampling the weight $|Z(s)|$. In the last equality of Eq. (3.104), summations are made of oscillatory functions $O(s)e^{i\theta}$ and $e^{i\theta}$. Generally, the numerical evaluation of the integral of a oscillatory function, like $e^{i\theta}$ in our case, will result in a sign problem due to strong

cancellations between operands in the numerical integration. In particular, if $e^{i\theta}$ is purely real, the numerical cancellation will appear for θ oscillating between 0 or π .

For now, consider Eq. (3.70), which describes the path integral for a system with the same number of spin-up and spin-down particles interacting via an operator that is spin- and isospin-independent. We generate configurations of auxiliary field $s(n, n_t)$ according to the weight

$$\exp \left\{ -\frac{1}{2} \sum_{\mathbf{n}, n_t} [s(\mathbf{n}, n_t)]^2 + 2 \ln \det[\mathcal{M}_\uparrow(s, t)] \right\}. \quad (3.105)$$

Since $s(\mathbf{n}, n_t)$ and $\det[\mathcal{M}_\sigma]$ are real-valued⁶, this weight is always positive and hence there is no sign problem for simulations of this physical system. However, if either of the following conditions is satisfied, there appears the sign problem in our simulations:

1. The number of particles for up and down spins are different;
2. The interaction is dependent on spin or isospin.

In next section, we will show an example of the sign problem that comes with the spin- and isospin-dependent interaction and demonstrate that the eigenvector continuation (EC) method [45] can yield a much better numerical results for this problem.

3.6.7 Eigenvector continuation method

As illustrated in Eq. (3.104), strong or weak sign problem will appear when we numerically integrate an oscillatory function. In Monte Carlo simulations with weak sign oscillations, we can expect to reach numerical accuracy by simply performing more stochastic sampling. However, simulations will often break down when one or more parameters in the Hamiltonian

⁶Find the definition of matrix \mathcal{M}_σ in Eq. (3.69)

exceed some tolerance threshold. In the following, we demonstrate that when a control parameter in the Hamiltonian matrix is varied smoothly, the extremal eigenvectors do not explore the full dimensionality of the Hilbert space. Instead, they trace out the trajectories with significant displacements in only a small number of linearly-independent directions. Since the eigenvector trajectory is a low-dimensional manifold embedded in a very large space, we can describe the low-dimensional space using eigenvectors that are readily computable and apply eigenvector continuation to solve the problems where direct calculations involve severe sign problem.

Let us consider a family of Hamiltonian matrices represented in a finite-dimensional linear space,

$$H(c) = H_0 + cH_1, \tag{3.106}$$

where H_0 and H_1 are Hermitian and c is the control parameter. We write the eigenfunctions

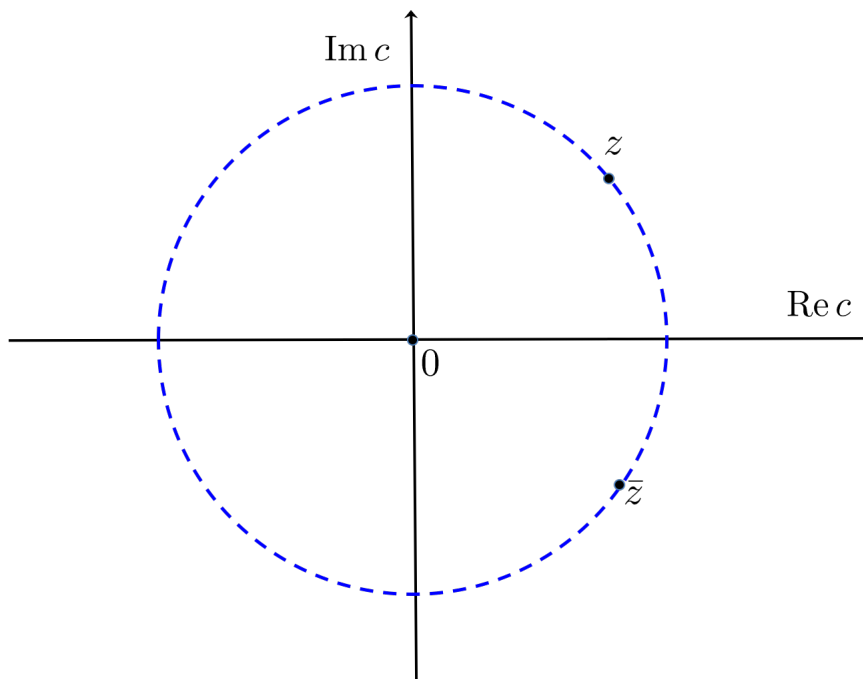


Figure 3.4: Convergence region of a function's series expansion about $c = 0$, with singularities z and \bar{z} .

for $H(c)$ as

$$H(c)|\psi_j(c)\rangle = E_j(c)|\psi_j(c)\rangle, \quad (3.107)$$

with j the index for the level of state. Since $H(c)$ is Hermitian for a real parameter c , $E_j(c)$ has no singularities on the real axis. We can define $|\psi_j(c)\rangle$ so that it has no singularities on the real axis, either. Performing a series expansion for eigenvectors around the point $c = 0$, we can write

$$|\psi_j(c)\rangle = \sum_{n=0}^{\infty} \frac{c^n}{n!} |\psi_j^{(n)}(0)\rangle, \quad (3.108)$$

where the superscript (n) denotes the n^{th} derivative. This is a standard strategy of perturbation theory for the calculations of eigenvectors $|\psi_j(c)\rangle$ when the eigenvectors of H_0 are computable or known. In Fig. 3.4, assuming z and its complex conjugate \bar{z} as the closest singularities to $c = 0$ in the complex plane, for all c in the convergence region $|c| < |z|$ the eigenvector $|\psi_j(c)\rangle$ is computable. What if a real parameter c' goes beyond the convergence region? We define an analytic extension by constructing a new series around another point $c = \omega$,

$$|\psi_j(c')\rangle = \sum_{n=0}^{\infty} \frac{(c' - \omega)^n}{n!} |\psi_j^{(n)}(\omega)\rangle, \quad (3.109)$$

where ω is real and $|\omega| < |z|$. The convergence region around $c = \omega$ (shaded area in Fig. 3.5) consists of a part inside $|c| < |z|$ and another part where c' is in. Since $|\omega| < |z|$, we can express each $|\psi_j^{(n)}(\omega)\rangle$ as a series expansion in terms of $|\psi_j^{(m)}(0)\rangle$ around $c = 0$. In this way we can approximate $|\psi_j(c')\rangle$ to arbitrary accuracy as a linear combination of the vectors $|\psi_j^{(n)}(0)\rangle$ in the region $|c' - \omega| < |z - \omega|$ centered at ω . Using this process of analytic continuation repeatedly, we can reach any value of c and express the corresponding vector $|\psi_j(c)\rangle$ as a linear combination of a finite number of vectors $|\psi_j^{(n)}(0)\rangle$. To achieve the

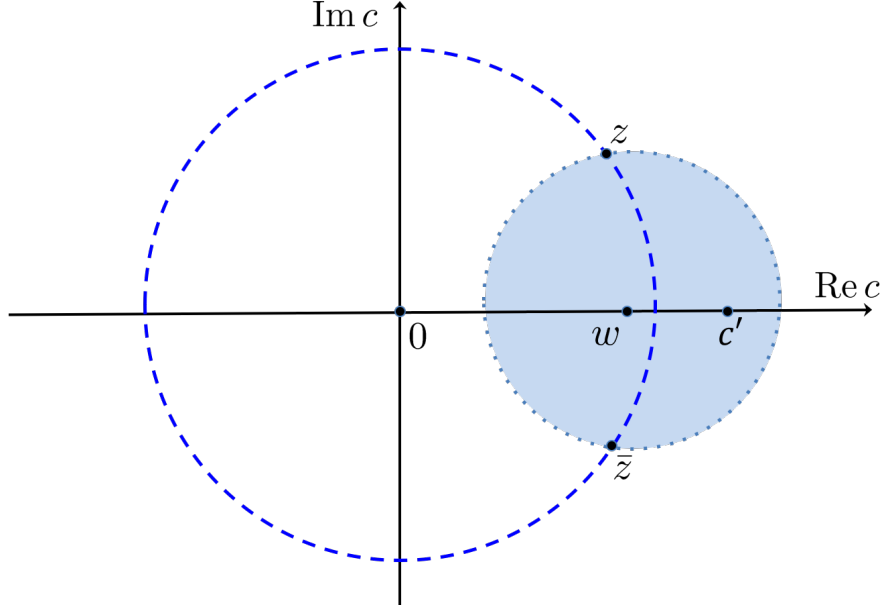


Figure 3.5: Analytic extension of a function's convergence region in the complex plane.

desired accuracy, the number of required vectors is determined by the number of different expansion centers in the repeated analytic expansion, and the rate of convergence of each series expansion.

The basic strategy of eigenvector continuation is to “learn” the low-dimensional subspace that contains the eigenvector trajectory $|\psi_j(c)\rangle$. For Hamiltonian $H(c)$, we pick several values $c = c_i$ with $i = 1, \dots, K$ and calculate the corresponding eigenvectors $|\psi_j(c_i)\rangle$. We usually start with the lowest eigenvalue and eigenvector in a given symmetry class. The values of c_i are chosen so that $|\psi_j(c_i)\rangle$ can be computed accurately with standard Monte Carlo simulations. The target value $c = c_\odot$ for which we want to compute $E_j(c_\odot)$ and $|\psi_j(c_\odot)\rangle$, often lies in a region where direct numerical calculation is not feasible. We then compute the norm kernel N via

$$N_{i',i} = \langle \psi_j(c_{i'}) | \psi_j(c_i) \rangle, \quad (3.110)$$

and represent the Hamiltonian kernel $H(c_\odot)$ in a finite-dimensional space spanned by the

different vectors $|\psi_j(c_i)\rangle$ with $i, i' = 1, 2, \dots, K$,

$$\mathcal{H}_{i',i} = \langle \psi_j(c_{i'}) | H(c_\odot) | \psi_j(c_i) \rangle. \quad (3.111)$$

Both N and \mathcal{H} are $K \times K$ matrices. Now we solve the Hill-Wheeler equation,

$$\mathcal{H}v = \lambda Nv, \quad (3.112)$$

where λ denotes the eigenvalue and v the corresponding eigenvector. For the lowest eigenvalue λ_0 and the corresponding eigenvector v_0 , it suffices to compute the lowest-energy eigenvectors of various c_i 's. To increase the accuracy of λ_0 and v_0 , we can proceed to the next-lowest eigenvector of different c_i 's. Continuing on in this manner, the exact values of λ_0 and v_0 can be reached with improved accuracy step by step⁷. In principle, any eigenvalue and eigenvector of $H(c_\odot)$ can be calculated in this way.

Let us apply eigenvector continuation method to the concrete example of neutron matter, where strong sign oscillation appears. Direct simulations cannot achieve accurate results for more than four neutrons and even the extrapolation methods discussed in Refs. [46, 47] provide no significant improvement. Simulations with an interaction that is softened at short distance are discussed in [48, 49], but we purposely use the computationally difficult lattice action in the following.

We consider the neutron matter in a $L \times L \times L$ lattice with leading-order lattice action [50] in chiral effective field theory. The lattice spacing, a , is 1.97 fm and time step, a_t , is 1.32 fm. We use $a_i(\mathbf{n})$ [$a_i^\dagger(\mathbf{n})$] to denote the annihilation (creation) operator with spin component i at lattice site \mathbf{n} . The shorthand $a(\mathbf{n})$ represents a column vector of $a_i(\mathbf{n})$ for all components

⁷See detailed discussion and proof in Ref. [45]

indexed by i , and $a^\dagger(\mathbf{n})$ represents a row vector of components $a_i^\dagger(\mathbf{n})$.

The free non-relativistic lattice Hamiltonian can be written as [155]

$$H_{free} = \sum_{k=0,1} \frac{(-1)^k}{2m} \sum_{\mathbf{n}} \sum_{l=1,2,3} a^\dagger(\mathbf{n}) \left[a(\mathbf{n} + k\hat{l}) + a(\mathbf{n} - k\hat{l}) \right], \quad (3.113)$$

where \hat{l} denotes each of the three lattice unit vectors, $\hat{1}$, $\hat{2}$, $\hat{3}$. We use the auxiliary-field formalism, hence there is no direct nucleon-nucleon interaction and nucleons only interact directly with the auxiliary field s and pion field π_0 . The Euclidean time projection operator over L_t time steps can be expressed as a product of transfer matrix operators dependent on s and π_0 ,

$$U(L_t, g^2) = \prod_{\mathbf{n}, n_t} \left[\int ds(\mathbf{n}, n_t) d\pi_0(\mathbf{n}, n_t) \right] \exp[-V_{ss}(s) - V_{\pi_0\pi_0}(\pi_0)] \quad (3.114)$$

$$\times \{M(s, \pi_0, g, L_t - 1) \cdots M(s, \pi_0, g, 0)\},$$

where g is a control parameter in the one-pion exchange potential (OPEP). When g assumes the value of the axial-vector coupling constant, $g_A = 1.29$, OPEP is fully considered in this system. We write the quadratic term of s coupling to itself as

$$V_{ss}(s) = \frac{1}{2} \sum_{\mathbf{n}, n_t} s^2(\mathbf{n}, n_t) \quad (3.115)$$

and the quadratic self-coupling for the pion field as

$$V_{\pi_0\pi_0}(\pi_0) = \frac{1}{2} \alpha_t m_\pi^2 \sum_{\mathbf{n}, n_t} \pi_0^2(\mathbf{n}, n_t) \quad (3.116)$$

$$+ \frac{1}{2} \alpha_t \sum_{k=0,1} (-1)^k \sum_{\mathbf{n}, n_t} \sum_{l=1,2,3} \pi_0(\mathbf{n}, n_t) \left[\pi_0(\mathbf{n} + k\hat{l}, n_t) + \pi_0(\mathbf{n} - k\hat{l}, n_t) \right].$$

In Eq. (3.114) the transfer matrix operator at time step n_t is defined by

$$M^{(n_t)} =: \exp \left[- H^{(n_t)}(s, \pi_0, g) \alpha_t \right] :, \quad (3.117)$$

where the Hamiltonian at time step n_t has the form [51]

$$H^{(n_t)}(s, \pi_0, g) \alpha_t = H_{free} \alpha_t + V_s^{(n_t)}(s) + V_{\pi_0}^{(n_t)}(\pi_0, g). \quad (3.118)$$

The auxiliary field s and pion field π_0 coupling to the particle density can be expressed as

$$V_s^{(n_t)}(s) = \sqrt{-c\alpha_t} \sum_{\mathbf{n}} s(\mathbf{n}, n_t) a^\dagger(\mathbf{n}) a(\mathbf{n}), \quad (3.119)$$

$$V_{\pi_0}^{(n_t)}(\pi_0) = \frac{g\alpha_t}{2f_\pi} \sum_{\mathbf{n}} \sum_{l=1,2,3} \frac{1}{2} [\pi_0(\mathbf{n} + \hat{l}, n_t) - \pi_0(\mathbf{n} - \hat{l}, n_t)] a^\dagger(\mathbf{n}) \sigma_l a(\mathbf{n}), \quad (3.120)$$

respectively. Here, c is the strength of contact interaction, which we set to be -4.8×10^{-5} MeV $^{-2}$. This is different from the value used in Ref. [47], but chosen to produce a more realistic equation of state for neutron matter at the densities we simulate here. σ_l for $l = 1, 2, 3$ denote the Pauli matrices.

We perform simulations of the ground state of six and fourteen neutrons in a $4 \times 4 \times 4$ lattice. In physical units this cubic box has side length $L = 7.9$ fm, and the corresponding number densities are 0.012 fm $^{-3}$ for six neutrons and 0.028 fm $^{-3}$ for fourteen neutrons. We take the initial and final states to be a Fermi gas of neutrons, which we write as $|\Psi\rangle$. Thus, the Euclidean time-projected ground state is defined as

$$|\Phi, L_t, g^2\rangle = U(L_t, g^2)|\Psi\rangle. \quad (3.121)$$

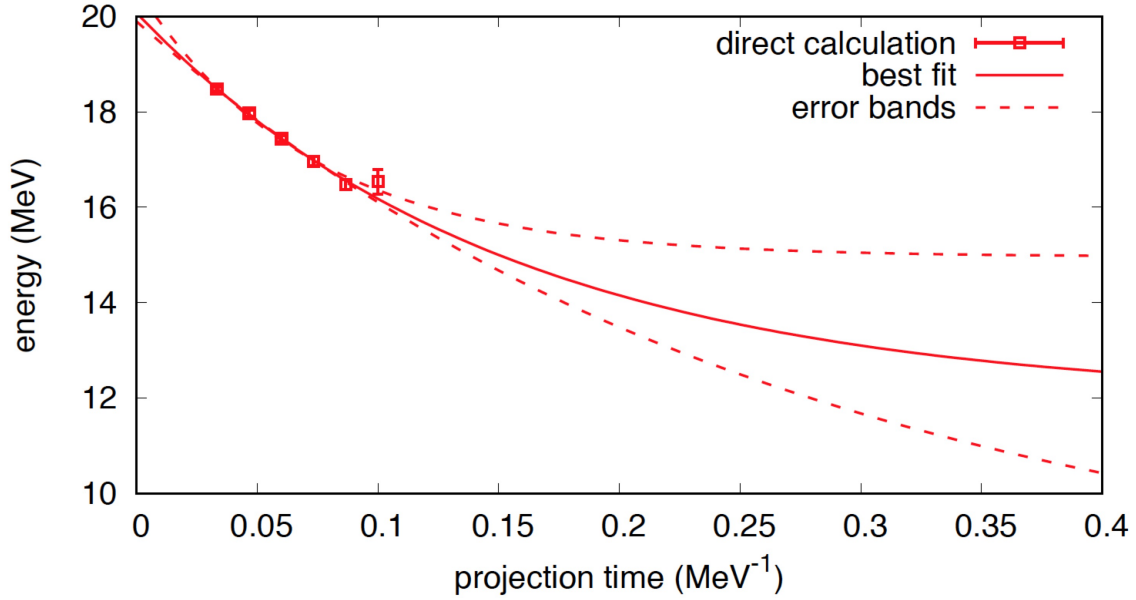


Figure 3.6: Direct calculations of the ground-state energy for six neutrons as a function of projection time. The red open squares are the raw data, solid line is the fitted curve, and the dashed lines indicate the one σ error of the fitted curve.

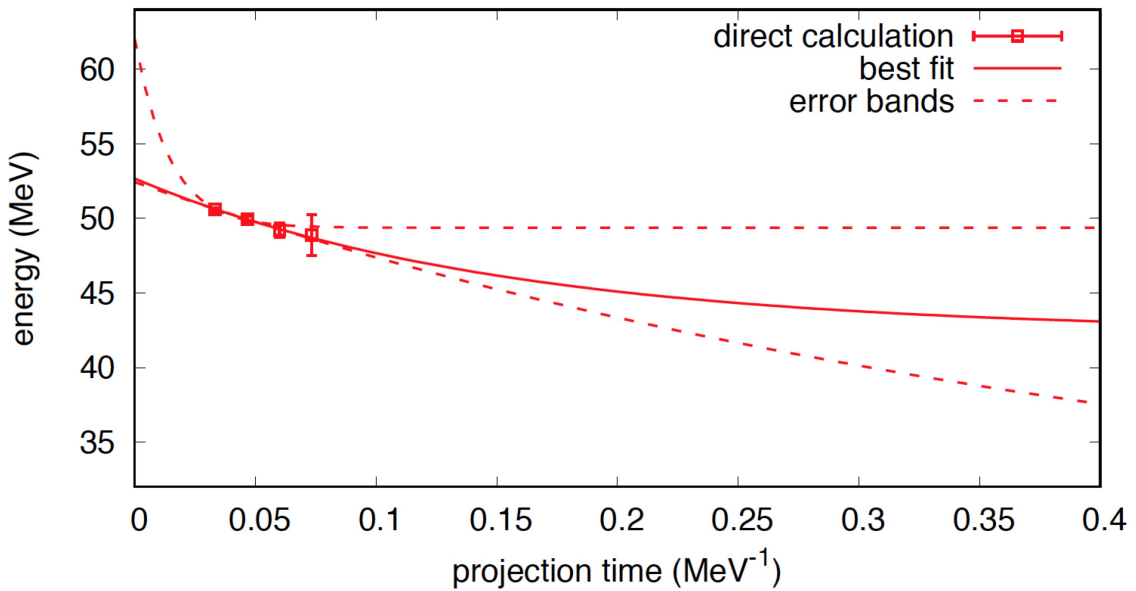


Figure 3.7: Direct calculations of the ground-state energy for fourteen neutrons as a function of projection time. The red open squares are the raw data, solid line is the fitted curve, and the dashed lines indicate the one σ error of the fitted curve.

In the limit of large L_t , we obtain the ground state for the selected value of control parameter g and the corresponding energy is calculated by

$$E(L_t) = -\alpha_t^{-1} \ln \frac{\langle \Phi | U(L_t, g^2) | \Phi \rangle}{\langle \Phi | U(L_t - \alpha_t, g^2) | \Phi \rangle}. \quad (3.122)$$

The ground state energy E_0 is determined by the asymptotic form

$$E(L_t) \approx E_0 + be^{-\delta E \cdot t}, \quad (3.123)$$

with the projection time $t = L_t \alpha_t$, as discussed in section 3.5.2.

In Fig. 3.6 and Fig. 3.7 we show the results of direct calculations for six neutrons and for fourteen neutrons, respectively, with $g = g_A$. Due to large sign oscillations, it is not possible to do simulations at large projection times. This is reflected in the large uncertainties of the ground-state energy extrapolations.

To use the eigenvector continuation method, we calculate the norm kernel N at time step n_t according to Eq. (3.110), for sampling values $g^2 = c_1, c_2, c_3$, where $c_1 = 0.25$, $c_2 = 0.60$, and $c_3 = 0.95$,

$$N_{i',i}(n_t) = \langle \Phi, n_t, c_{i'} | \Phi, n_t, c_i \rangle. \quad (3.124)$$

We then calculate the Hamiltonian kernel \mathcal{H} for the target value $g^2 = c_\odot = g_A^2 = 1.66$,

$$\mathcal{H}_{i',i} = \langle \Phi, n_t, c_{i'} | U(1, c_\odot) | \Phi, n_t, c_i \rangle, \quad (3.125)$$

where $U(1, c_\odot)$ is the Euclidean time projection operator for one time step. We solve the Hill-Wheeler equation (Eq. (3.112)) and find the largest eigenvalue, $\lambda(n_t)$. This corresponds

to finding the ground state energy using the relation

$$E(n_t) = -\alpha_t^{-1} \ln[\lambda(n_t)]. \quad (3.126)$$

We then extrapolate the measured $E(n_t)$ towards the limit of infinite projection time using the following asymptotic form

$$E(n_t) \approx E_0 + be^{\delta E \cdot t}, \quad (3.127)$$

where $t = (2n_t + 1)\alpha_t$ is the projection time. In these calculations we consider seven different choices of eigenvector subspace. For the first three we consider one-dimensional subspaces spanned by the single vector $|\Psi, n_t, c_i\rangle$ for all i . For the next three we consider the two-dimensional subspaces spanned by two vectors $|\Psi, n_t, c_i\rangle$ and $|\Psi, n_t, c_{i'}\rangle$ for all $i' \neq i$. For the last one we consider the three-dimensional subspace spanned by $|\Psi, n_t, c_1\rangle$, $|\Psi, n_t, c_2\rangle$, and $|\Psi, n_t, c_3\rangle$.

In Fig. 3.8, the estimated ground-state energies of six neutrons are shown versus projection time with sampling data $g^2 = c_1, c_2, c_3$. We report the results measured by using one vector, two vectors, and all three vectors. The error bars of data points are calculated by the jackknife analysis [44] in our Monte Carlo simulations. We have imposed the variational constraint that the ground-state energy cannot go higher as more sampling points of c_i are used. The results for fourteen neutrons are reported in Fig. 3.9 with sampling data $g^2 = c_1, c_2$, and c_3 . The results are again obtained using one vector, two vectors, and all three vectors. In table 3.1, we summarize the results of the direct calculations and EC calculations for six- and fourteen-particle systems. It is evident that EC results converge

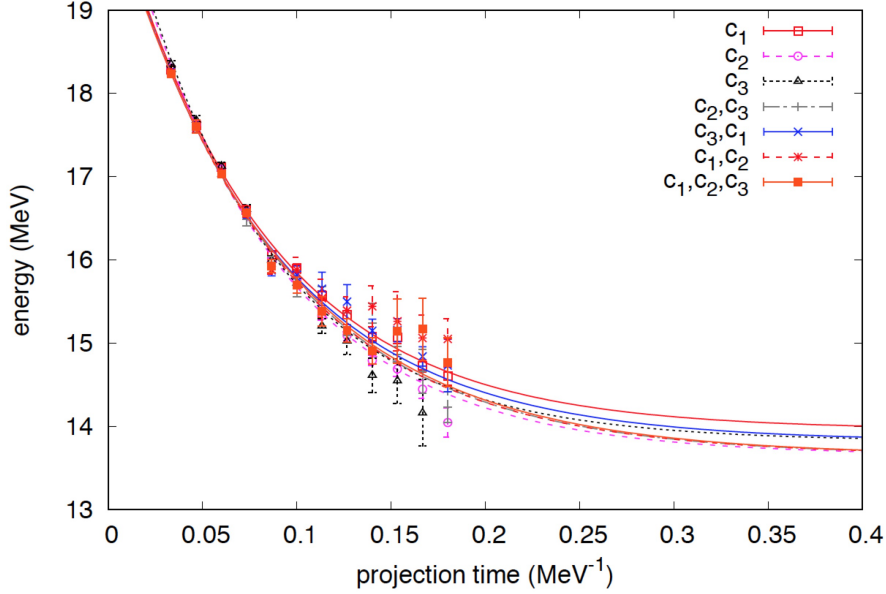


Figure 3.8: Eigenvector continuation measurements of the ground-state energy for six neutrons versus projection time, using sampling data $g^2 = c_1, c_2, c_3$, where $c_1 = 0.25$, $c_2 = 0.60$, and $c_3 = 0.95$. We show results obtained using one vector: c_1 (red open squares), c_2 (magenta open circles), c_3 (black open triangles); two vectors: c_1, c_2 (red asterisks), c_2, c_3 (grey pluses), c_1, c_3 (blue crosses); three vectors: c_1, c_2, c_3 (orange filled squares).

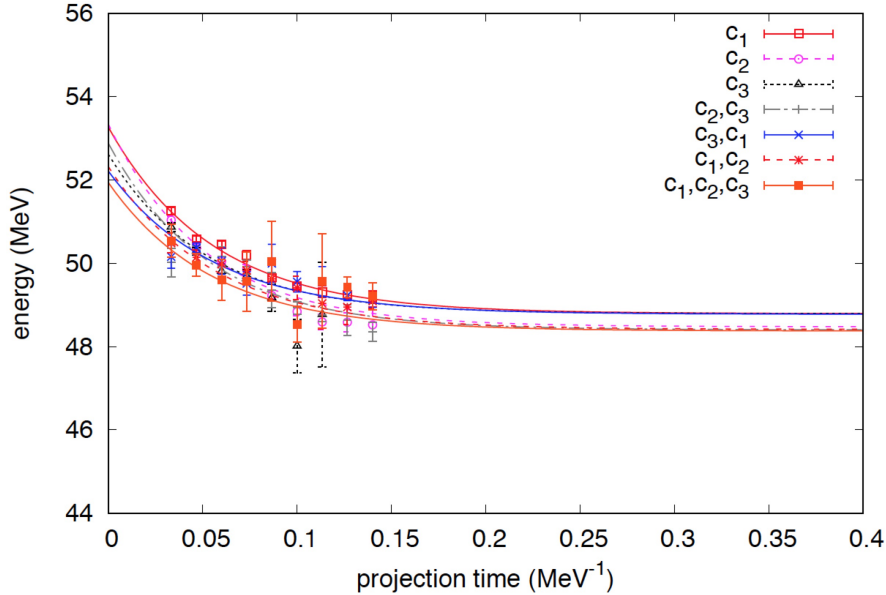


Figure 3.9: Eigenvector continuation measurements of the ground-state energy for fourteen neutrons versus projection time, using sampling data $g^2 = c_1, c_2, c_3$, where $c_1 = 0.25$, $c_2 = 0.60$, and $c_3 = 0.95$. We show results obtained using one vector: c_1 (red open squares), c_2 (magenta open circles), c_3 (black open triangles); two vectors: c_1, c_2 (red asterisks), c_2, c_3 (grey pluses), c_1, c_3 (blue crosses); three vectors: c_1, c_2, c_3 (orange filled squares).

rapidly as the number of vectors included increases. The extrapolated results agree with the direct calculation results and have smaller deviations by an order of magnitude.

Table 3.1: Direct calculations and eigenvector continuation results for the ground state energy for six and fourteen neutrons using sampling data $g^2 = c_1, c_2, c_3$, where $c_1 = 0.25$, $c_2 = 0.60$, and $c_3 = 0.95$.

Control parameter	$E_0(N = 6)$ [MeV]	$E_0(N = 14)$ [MeV]
c_1	14.0(4)	48.8(6)
c_2	13.7(4)	48.5(7)
c_3	13.8(6)	48.8(8)
c_1, c_2	13.7(4)	48.4(7)
c_2, c_3	13.7(4)	48.4(7)
c_1, c_3	13.8(4)	48.8(6)
c_1, c_2, c_3	13.7(4)	48.4(7)
Direct calculation	$12^{(+3}_{-4)}$	$42^{(+7}_{-15)}$

In conclusion, we can use the eigenvector continuation method to avoid direct calculations in the domain with strong sign problem, which are not computationally efficient. Instead, eigenvectors calculated in the domains with fairly weak sign oscillation can generate a low-dimensional subspace where stable results can be obtained to expected accuracy. Eigenvector continuation can also be used to significantly extend the convergence region for perturbation theory [45]. While EC is not applicable to Krylov space methods like the Lanczos algorithm [52, 53], which uses a truncated basis with fixed dimensions, it could be used to extend the reach of techniques that reduce the basis truncation errors [54].

Chapter 4

Systems of Fermions

4.1 Introduction

In 1908, Kamerlingh Onnes found superfluidity in ${}^4\text{He}$ at a transition temperature $T_\lambda = 2.2$ K (the λ -point) [55]. It is because the zero-point motion of ${}^4\text{He}$ is large enough to prevent the forming of solids, we still can have a liquid ${}^4\text{He}$ at such a low temperature. Onnes then used ${}^4\text{He}$ to cool down mercury in 1911 and found the non-measurable resistivity at $T_C = 4.2$ K. Tin (at $T_C = 3.8$ K) and lead (at $T_C = 6$ K) were then found to show the same property of zero resistivity. This was the discovery of superfluidity in electronic gases.

It was believed that bosonic and fermionic superfluidity occurs at the degeneracy temperature, at which the inter-particle distance $n^{-\frac{1}{3}}$ at density n is comparable with the de Broglie wavelength $\lambda = \sqrt{\frac{2\pi\hbar^2}{mk_B T}}$. For liquid ${}^4\text{He}$ at typical density $n = 10^{22}$ cm^{-3} , the theoretical transition temperature of $T_\lambda \sim \frac{2\pi^2}{m} n^{2/3} \approx 3$ K agrees well with the measured value. However, for fermionic superfluidity, the degeneracy temperature is predicted to be much higher than the observed value due to the large mass ratio $\frac{m({}^4\text{He})}{m_e} \sim 10^4$. It is intuitive to think that two electrons might form a bound pair and behave like a bosonic particle, but there was no known interaction at the time which could be stronger than Coulomb repulsion and allow the electrons to form bound pairs [56].

In 1950, it was demonstrated that the vibration of crystal lattice can provide the needed

attractive interaction between electrons. The isotope effect predicted by H. Fröhlich [57–59] made a prediction of T_C closer to the measured value, but it was still one or two orders of magnitude higher. It was in 1956 that L. Cooper found that fermions on the top of a filled Fermi sea could form bound pairs in the presence of an arbitrarily weak attractive interaction [175]. The pairs are formed across a quite long distance, much larger than the inter-particle separation. Ensembles of those so-called Cooper pairs overlap strongly in space: since Cooper pairs are composite bosons, those pairs can all occupy the same quantum state. One year later, Bardeen, Cooper and Schrieffer (BCS) developed a full theory of superconductivity that includes the pair formation in a self-consistent way [60]. It states that due to the attractive electron-phonon interaction, there appears an effective attraction between electrons. Consequently, electrons can form pairs and the pairing opens up a gap in the continuous spectrum of electron energy states. Therefore, excitations of the systems need a minimum amount of energy. At a very low temperature, collisions with the solid lattice do not have sufficient energy to overcome the gap, hence Cooper pairs exhibit zero resistivity while the electron are in motion through a solid. The pair gap was found to be $\Delta = 2k_B T_D e^{-1/\rho_F |V|}$, with V the electron-electron interaction and $\rho_F = m_e k_F / 2\pi^2 \hbar^2$ the density of states at the Fermi energy.

In BCS theory, a pair is formed with zero total momentum if the Fermi momenta for two spin species are identical. A system with this feature is called balanced or unpolarized. Still, pair formation in polarized system with mismatched Fermi momenta is possible, which results in pairs with finite momentum. This situation was envisioned by B.S. Chandrasekhar [61] and A.M. Clogston [62] a few years after BCS theory. Based on this idea, Fulde and Ferrell [63] and Larkin and Ovchinnikov [64] proposed an exotic pairing mechanism that is characterized by a spatially non-uniform order parameter. This special phase is called FFLO (or LOFF)

phase, named after its discoverers. In principle, it can arise in a superconductor if a strong magnetic field is imposed. Early experiments showed seemingly conflicting results [65, 66], which have motivated many theoretical studies [67–74]. FFLO phase in one-dimensional systems has been first observed [95] with a finite spin-imbalance in the Fermi gas in 2010. In two-dimensional systems, extensive efforts have been devoted to the discovery of the FFLO phase [75–84], especially for the layered superconductors. In three dimensions, however, the experiments [96–99] showed no evidence of the FFLO phase and theoretical calculations found [100, 101] a strong shrinkage of available phase space for FFLO phase.

So far, we have discussed the pairing in Fermi systems and the effective attraction between fermions could be arbitrarily weak according to BCS theory. If we continually increase the strength of interaction to very large, the two fermions will form a deeply bound state – a composite boson, which will obey Bose-Einstein statistics. Even though BCS and BEC pairs obey different thermal statistics [102], there still might exist intermediate strength of interaction that can connect those two regimes. It was realized [103–105] that the BCS formalism and its ground-state wave function can describe the condensate of a dilute gas of tightly bound pairs as well. In 1969, Eagles [105] showed that, in the limit of very high density, BCS pairs become a condensate of pairs of which the size is smaller than the inter-particle distance and should follow BEC formalism. In the language of generic two-body potential, in 1980, Leggett showed that there is a smooth crossover between large-sized Cooper pairs and tightly bound molecules as the strength of the interaction is varied smoothly [106]. Here the particle density was fixed. He noted that the correlation length between fermions in a pair is much larger than the inter-particle distance in BCS limit and decreases smoothly towards the bound molecules in BEC limit (See Fig. 4.1). Correspondingly, the pair binding energy is small in the BCS limit, but it becomes larger as the strength of

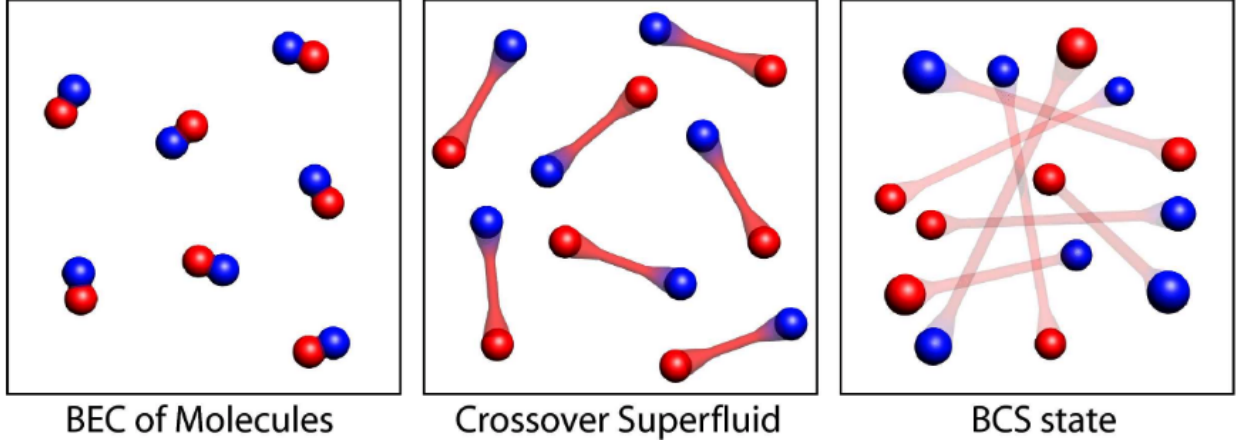


Figure 4.1: The BEC-BCS crossover [107]. The two-body interaction is varied; when the interaction is strong, the pair is in bound state as BEC state of molecules (left); when the interaction is arbitrarily weak, Cooper pairs are formed and the system reaches the BCS limit (right); the intermediate regime at the crossover shows the pair size is comparable with inter-particle spacing (middle).

interaction gets stronger and the pair turns into a BEC molecule state.

As the strength of two-body interaction is smoothly varied, the regime around an infinite scattering length is of special interest, where the two-body interaction is the strongest, beyond which the pair is bound. This is the unitary limit. At low density, the S-wave interaction dominates and the effective range of interaction r_e is small compared to the inter-particle distance $n^{-\frac{1}{3}}$. Now we have a separation of scales $r_e \ll n^{-\frac{1}{3}} \ll a_s$, with a_s the scattering length. In this circumstance, physics is said to be universal [108]. There is no energy scale and the only length scale is $n^{-\frac{1}{3}}$ or equivalently k_F^{-1} . Consequently, the binding energy of the pair and the ground-state energy are related to the Fermi energy by universal constants. Similarly, the size of a Cooper pair is related to the inter-particle spacing by a universal constant, as well.

4.2 Universal parameter in the unitary limit

In experiments with ultracold atoms, the so-called Feshbach resonance [110] is a useful tool for tuning the interaction of the two-body interaction. Basically, the scattering length can be varied through a magnetic field,

$$a(B) = a_{bg}\left(1 - \frac{\Delta B}{B - B_0}\right), \quad (4.1)$$

where ΔB is the width of the magnetic field with strength B and a_{bg} is the background scattering length. With this tool it is possible to alter the scattering length of interactions between fermions and study the physics over many length scales. It is obvious that at $B = B_0$, a resonance appears and the scattering length becomes infinite, realizing the unitary limit. As we mentioned in the introduction, in this limit only the particle density provides a relevant length scale, and ground-state energy E_0 can be written as

$$E_0 = \xi E_{FG}, \quad (4.2)$$

where ξ is an universal parameter (also called Bertsch parameter) and E_{FG} is the energy of free Fermi gas. The Bertsch parameter have been measured by many experiments using the ultracold trapped atoms [97, 121–131] and also calculated by analytical methods [132–145]. In addition, a substantial number of numerical studies of fermions at unitarity has been made using Quantum Monte Carlo and other techniques [146–163]. In section 4.2, we will calculate the Bertsch parameter in a Fermi system with an equal number of spin-up and spin-down particles. The system is built on a $L \times L \times L$ periodic lattice.

4.2.1 Free particles on the lattice

As in Eq. (3.26), we consider the hopping terms up to the 3rd nearest neighbors along axes for the kinetic-energy operator in order to reduce the effect of a finite lattice spacing. Since particles live in a periodic box, the momentum space is not continuous and we can only fill in particles with quantized momenta $k\frac{2\pi}{L}$, where k is integer. Table 4.1 shows the order that particles fill in the momentum states for each spin. The “closed shells” on the lattice are at $N_\sigma = 1, 7, 19, 27, 33, 57, 81, \dots$, where σ denotes the spin species. In realistic simulations, we prefer to choose N_σ to be at the “closed shell” and L^3 to be sufficiently large compared to the lattice spacing.

Now let us compare our lattice-based calculations and the analytic results for the ground-state energy of a free gas with the same number of particles for two spin species, $N_\uparrow = N_\downarrow$. From this comparison, we will determine a best choice of particle number for later calculations. We know the analytic form of the ground-state energy for a free gas is $E_{N_\uparrow, N_\downarrow}^{thermo} = (N_\uparrow + N_\downarrow)\frac{3}{5}\frac{k_F^2}{2m}$ with $k_F = \frac{(3\pi^2 N_\sigma)^{1/3}}{L}$, where “thermo” denotes the thermodynamic limit. To quantify the non-interacting ground-state energy $E_{N_\uparrow, N_\downarrow}^{0, free}$ on the lattice, we calculate the absolute value of the relative difference $\gamma(N, L) = \frac{|E_{N_\uparrow, N_\downarrow}^{0, free} - E_{N_\uparrow, N_\downarrow}^{thermo}|}{E_{N_\uparrow, N_\downarrow}^{thermo}}$ at closed shells,

Table 4.1: Sequence of momentum states filled for each spin

N	additional momenta filled	N	additional momenta filled
1	$\langle 0, 0, 0 \rangle$	11	$\langle \frac{2\pi}{L}, \frac{2\pi}{L}, 0 \rangle, \langle \frac{2\pi}{L}, -\frac{2\pi}{L}, 0 \rangle, \langle -\frac{2\pi}{L}, \frac{2\pi}{L}, 0 \rangle, \langle -\frac{2\pi}{L}, -\frac{2\pi}{L}, 0 \rangle$
3	$\langle \frac{2\pi}{L}, 0, 0 \rangle, \langle -\frac{2\pi}{L}, 0, 0 \rangle$	15	$\langle \frac{2\pi}{L}, 0, \frac{2\pi}{L} \rangle, \langle \frac{2\pi}{L}, 0, -\frac{2\pi}{L} \rangle, \langle -\frac{2\pi}{L}, 0, \frac{2\pi}{L} \rangle, \langle -\frac{2\pi}{L}, 0, -\frac{2\pi}{L} \rangle$
5	$\langle 0, \frac{2\pi}{L}, 0 \rangle, \langle 0, -\frac{2\pi}{L}, 0 \rangle$	19	$\langle 0, \frac{2\pi}{L}, \frac{2\pi}{L} \rangle, \langle 0, \frac{2\pi}{L}, -\frac{2\pi}{L} \rangle, \langle 0, -\frac{2\pi}{L}, \frac{2\pi}{L} \rangle, \langle 0, -\frac{2\pi}{L}, -\frac{2\pi}{L} \rangle$
7	$\langle 0, 0, \frac{2\pi}{L} \rangle, \langle 0, 0, -\frac{2\pi}{L} \rangle$

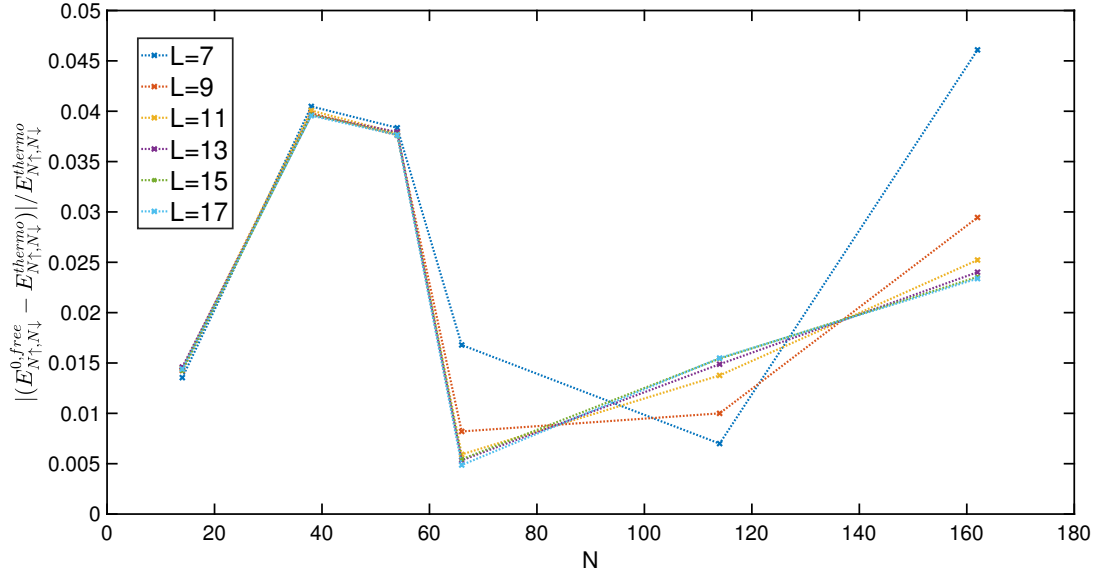


Figure 4.2: The absolute value of the relative difference between $E_{N_{\uparrow}, N_{\downarrow}}^{0, free}$ and $E_{N_{\uparrow}, N_{\downarrow}}^{thermo}$ versus the total particle number N ($= 2N_{\uparrow} = 2N_{\downarrow}$) for different lattice side length L .

$N = 14, 38, 54, 66, 114, 162$, for various lattice sizes.

In Fig. 4.2, with lattice size fixed to certain values, $L = 7, 9, 11, 13, 15, 17$, the absolute value of relative difference, $\gamma(N, L)$, is oscillating as we fill more and more particles in momentum space. This is due to the finite size of the lattice. It can be remedied by the twist-averaged boundary conditions¹ (TABCs), while in practice, we fix the total particle number to a good value so that the system is close to that at the thermodynamic limit.

It is apparent in Fig. 4.3 that expanding the lattice size does not necessarily mean the result is getting closer to the thermodynamic limit. For the listed closed shells, only at $N = 66$ the relative difference is definitely decreasing with the expanding lattice size. For later calculations, we need to extrapolate to the infinite lattice volume, using a limited number of particles and a finite lattice volume; therefore, 66 particles appears to be the best

¹TABCs are successfully applied in the context of many-electron systems [111–113], nucleonic matter [114, 115], lattice QCD [116, 117], and neutron star [118, 119].

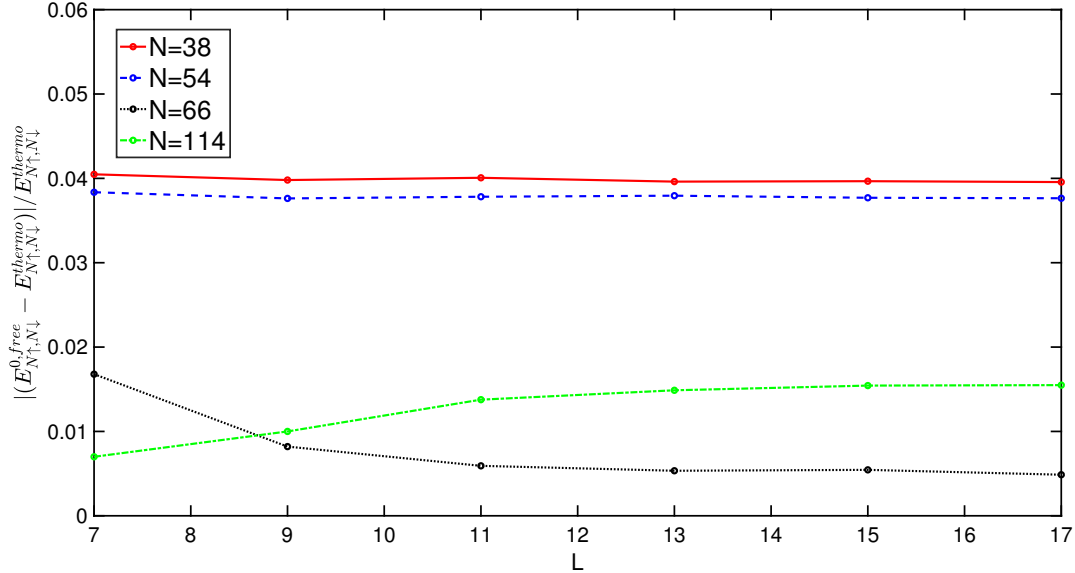


Figure 4.3: The absolute value of relative difference between $E_{N_{\uparrow}, N_{\downarrow}}^{0, free}$ and $E_{N_{\uparrow}, N_{\downarrow}}^{thermo}$ versus L for different total particle number N with $N_{\uparrow} = N_{\downarrow}$.

choice.

4.2.2 Bertsch parameter in the continuum limit

We consider a system of fermions with $N_{\uparrow} = N_{\downarrow} = 33$ on a $L \times L \times L$ periodic lattice. L varies from 5 through 11 and we do calculations for each lattice size. The Hamiltonian² consists of the kinetic energy operator (Eq. (3.26)) and the contact interaction between two spin species (Eq. (3.22)),

$$H = H_{free} + V_0. \quad (4.3)$$

In order to be in the unitary limit, we tune the parameters in V_0 . Parameter s_{NL} is set to -0.0100 ; c_0 is -5.733×10^{-5} MeV⁻² in physical units or -0.5733 in dimensionless lattice unit. Scattering length $a_s \sim 10^8$ and effective range of interaction $r_e \sim 0.05$ are both in

²See details in section 3.2

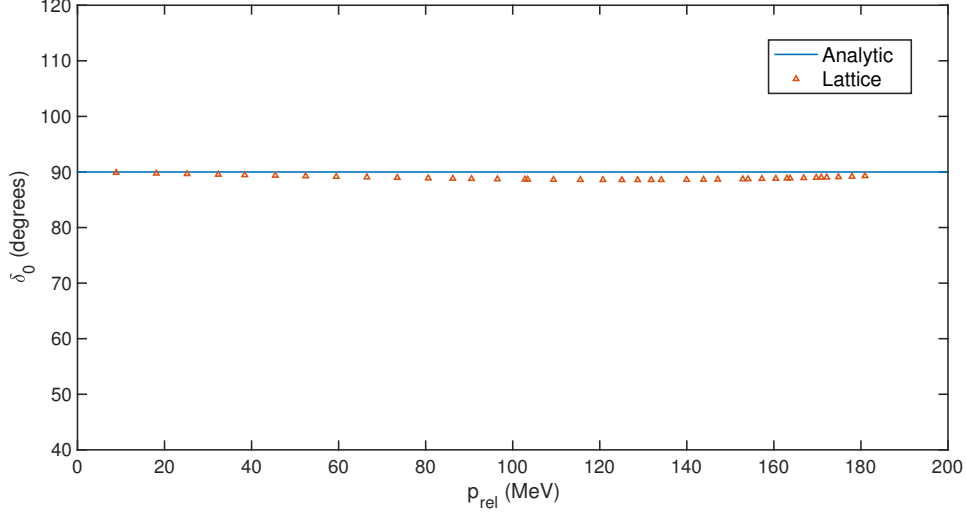


Figure 4.4: Phase shift of s-wave at unitary limit: analytic value of phase shift (blue line) and the phase shift measure on the lattice (orange triangle).

dimensionless lattice unit and determined according to paper [120]. In Fig. 4.4 we show the s-wave scattering phase shift on the lattice compared to the analytic results and the fitting is very good. We include 66 particles into the system and the condition $r_e \ll n^{-\frac{1}{3}} \ll a_s$ is readily satisfied.

Considering both spin species are filled in momentum space in the same way via table 4.1, according to Eq. (3.70), the path integral \mathcal{Z} is real and non-negative. Therefore, there is no sign problem for our simulations of these physics systems. We use the Euclidean time projection method to calculate the ground-state wave function, starting with an initial wave function $|\Phi_{N_\uparrow, N_\downarrow}^{0, free}\rangle$ that is the Slater-determinant ground state of non-interacting system with $N_\uparrow = N_\downarrow = 33$.

In our simulations, we measure the ground-state energy $E_{N_\uparrow, N_\downarrow}^0(t)$ and the corresponding ratio $E_{N_\uparrow, N_\downarrow}^0(t)/E_{FG}$ at different projection time t . The free-gas energy E_{FG} can be evaluated using $E_{N_\uparrow, N_\uparrow}^{thermo}$ and $E_{N_\uparrow, N_\uparrow}^{0, free}$, which also gives us two ways to extract the Bertsch parameter, namely the thermodynamical-limit definition $\xi_{N_\uparrow, N_\uparrow}^{thermo} = E_{N_\uparrow, N_\downarrow}^0/E_{N_\uparrow, N_\uparrow}^{thermo}$ and

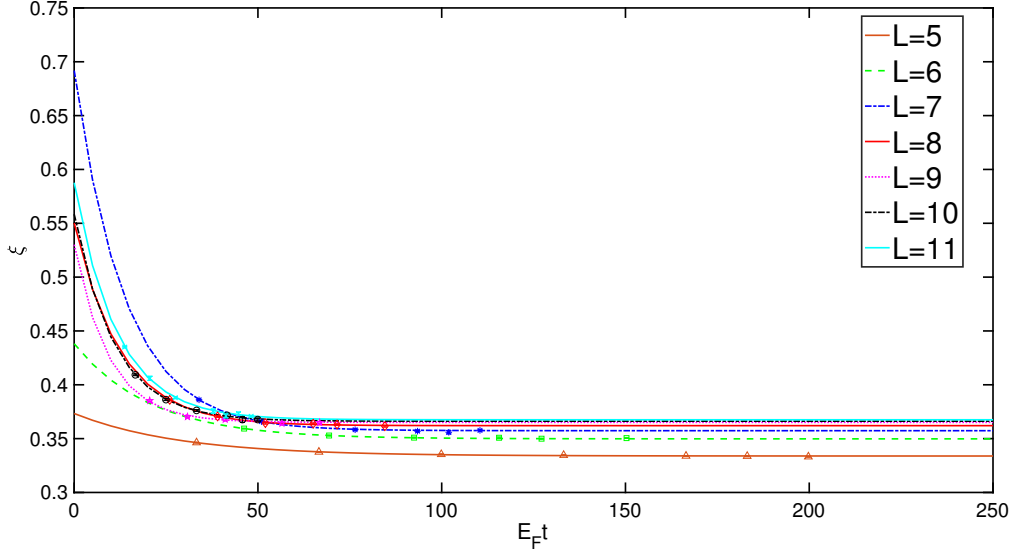


Figure 4.5: Bertsch parameter $\xi_{N_{\uparrow}, N_{\uparrow}}^{thermo}(t) = E_{N_{\uparrow}, N_{\uparrow}}^0(t)/E_{N_{\uparrow}, N_{\uparrow}}^{thermo}$ with $N_{\uparrow} = N_{\downarrow} = 33$ for various L and fitted curves extrapolated to infinite t . Note that we use dimensionless variable $E_F t$ instead of t as horizontal axis.

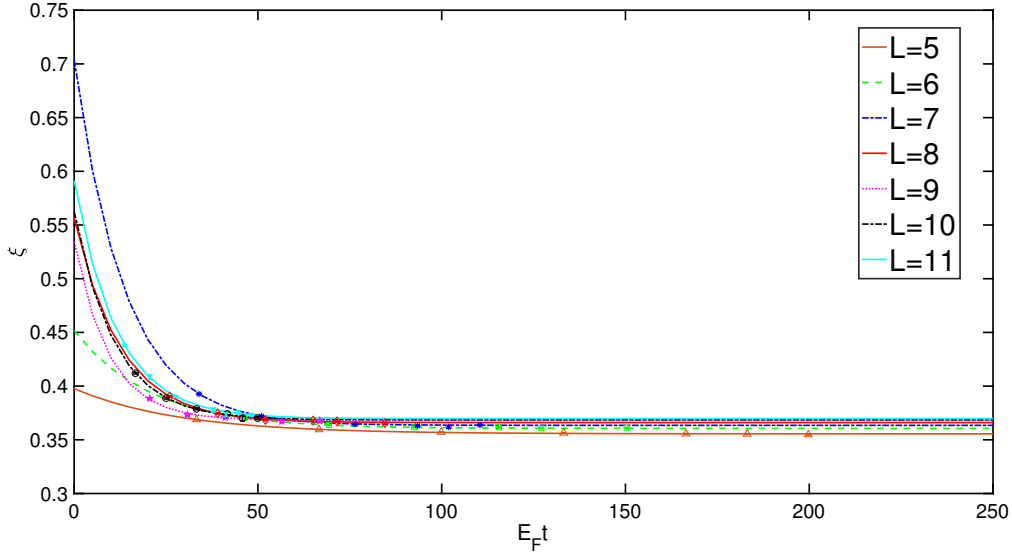


Figure 4.6: Bertsch parameter $\xi_{N_{\uparrow}, N_{\uparrow}}(t) = E_{N_{\uparrow}, N_{\uparrow}}^0(t)/E_{N_{\uparrow}, N_{\uparrow}}^{0, free}$ with $N_{\uparrow} = N_{\downarrow} = 33$ for various L and fitted curves extrapolated to infinite t . Note that we use dimensionless variable $E_F t$ instead of t as horizontal axis.

the few-body definition $\xi_{N_{\uparrow}, N_{\downarrow}} = E_{N_{\uparrow}, N_{\downarrow}}^0/E_{N_{\uparrow}, N_{\downarrow}}^{0, free}$. In Fig. 4.5 and Fig. 4.6, we show $\xi_{N_{\uparrow}, N_{\downarrow}}^{thermo}$ and $\xi_{N_{\uparrow}, N_{\downarrow}}$ measured in various volumes as functions of the projection time t .

Table 4.2: Bertsch parameter extrapolation to infinite volume for fixed particle number $N = 66$ with different fitting functions. The highlighted rows are for $\xi_{N_{\uparrow}, N_{\downarrow}}^{thermo}$ and the unhighlighted rows for $\xi_{N_{\uparrow}, N_{\downarrow}}$.

Function	A	B	C	ξ	err	χ^2/DOF
$A\rho^{2/3} + B\rho + \xi$	0.0824	-0.7046		0.3685	0.0016	1.2
	-0.0100	-0.0040		0.3726	0.0016	1.2
$B\rho + C\rho^{4/3} + \xi$		-0.3447	-0.4283	0.3696	0.0010	1.1
		-0.4130	0.4604	0.3710	0.0010	1.3

We fit the usual exponentials to the calculated data, since the Euclidean time projection method³ is employed here. Using Eq. (3.85), each fitted curve also yields an excitation energy $E_{N_{\uparrow}, N_{\downarrow}}^1 - E_{N_{\uparrow}, N_{\downarrow}}^0$, which can be used as a known parameter for the fitting of other observables versus projection time.

Our estimates of the Bertsch parameter at $t \rightarrow \infty$ are all calculated on a finite-sized lattice, hence we need to extrapolate the data to the infinite volume limit. In Fig. 4.7, we report our calculations of Bertsch parameter as a function of density ρ , where $\rho = N(aL)^{-3}$. Since the range of two-body interactions is small compared to the lattice spacing, the leading term in the fitting function is a least of order L^{-2} . Least-squares method is used for the curve fitting and we have used two fitting functions. In table 4.2, we show the estimated parameters and error bars for ξ . χ^2/DOF is the reduced chi-squared, where DOF represents the degrees of freedom of the fitting. The highlighted rows are for $\xi_{N_{\uparrow}, N_{\downarrow}}^{thermo}$ and the unhighlighted rows for $\xi_{N_{\uparrow}, N_{\downarrow}}$.

Our estimates of the Bertsch parameter are clearly consistent and the results are accurate with regard to the error bars provided in the table. Our results are also in agreement with the auxiliary-filed Monte Carlo result 0.372(5) [163] and the upper bound 0.383(1) calculated by

³See rigorous derivation and discussion in section 3.4

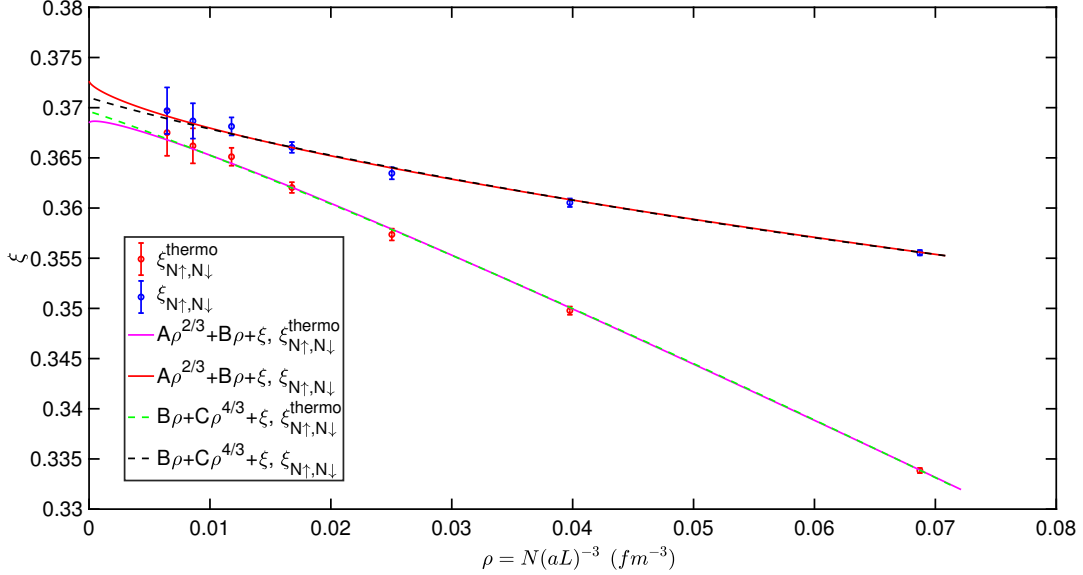


Figure 4.7: $\xi_{N_{\uparrow}, N_{\downarrow}}^{thermo}$ and $\xi_{N_{\uparrow}, N_{\downarrow}}$ measured in various lattice volumes are fitted to different functions of density ρ .

fixed-node diffusion Monte Carlo combined with density functional theory [159,161]. Lattice QMC calculations extrapolated to low-density range from 0.3-0.4 [155, 157] and they are consistent with the analytic results [140,142]. Our results agree with the experimental value 0.376(4) determined by the MIT group [131], but lie below earlier measurements [128, 129, 164]. Note that in table 4.2 (and Fig. 4.7), $\xi_{N_{\uparrow}, N_{\downarrow}}^{thermo}$ appears systematically smaller than $\xi_{N_{\uparrow}, N_{\downarrow}}$ for both of the fitting functions. This, in fact, reveals the effect of the finite number of particles in this system. We demonstrate this through a comparison of $\xi_{N_{\uparrow}, N_{\downarrow}}^{thermo}$ and $\xi_{N_{\uparrow}, N_{\downarrow}}$, by calculating $\xi_{N_{\uparrow}, N_{\downarrow}}^{thermo} / \xi_{N_{\uparrow}, N_{\downarrow}}$ for various lattice sizes (see table 4.3). The ratio gets larger as the lattice expands and we find a value of 0.9954(2) when $L \rightarrow \infty$.

In any one of the Monte Carlo simulations, we use up to 4096 parallel threads, each one of which involves about 800 independent Euclidean time projections, to achieve accurate results and good statistics. GPU-based algorithms boost the computation speed compared to the traditional CPU-based simulations. Especially when the system gets larger, the increase

Table 4.3: Ratios between $\xi_{N_\uparrow, N_\downarrow}^{thermo}$ and $\xi_{N_\uparrow, N_\downarrow}$ for various lattice sizes with $N_\uparrow = N_\downarrow = 33$.

L	$\xi_{N_\uparrow, N_\downarrow}^{thermo} / \xi_{N_\uparrow, N_\downarrow}$	L	$\xi_{N_\uparrow, N_\downarrow}^{thermo} / \xi_{N_\uparrow, N_\downarrow}$
5	0.9390	9	0.9918
6	0.9702	10	0.9933
7	0.9832	11	0.9941
8	0.9891	∞	0.9954(2)

of computation speed is more significant. In Fig. 4.8, we compare the performance of the GPU and CPU versions of our program with fixed particle density $\rho = 0.012 \text{ fm}^{-3}$. The y-axis is the logarithm of time consumed for generating an update for $s(\mathbf{n}, n_t)$ over \mathbf{n} and n_t per particle per unit volume and along x-axis we list the different systems. For instance, “N6L4” has 6 particles, half spin-up and half spin-down, in a $4 \times 4 \times 4$ lattice. For smaller systems (left side of x-axis), CPU is faster, but as the lattice and particle number increase (right side of x-axis) the efficiency of the CPU is reduced, while that of the GPU improves by orders of magnitude. In the system of 48 particles in a $8 \times 8 \times 8$ lattice, for instance, the GPU-based simulation is a factor of ten faster than the CPU-based simulation. Thus, GPU could provide significant speedups for large systems in this part of the calculation, but a drawback of using GPU is their relatively small memory compared to the CPU’s main memory. We need to figure out a more memory-efficient way in building GPU-based algorithms. In our calculations, we exploit the fact that the Hamiltonian commutes with time reversal operator⁴,

$$T = \pm i\sigma_y K, \quad (4.4)$$

⁴The choice of plus or minus sign depends on the convention of the specific theory and we use the minus sign in our case.

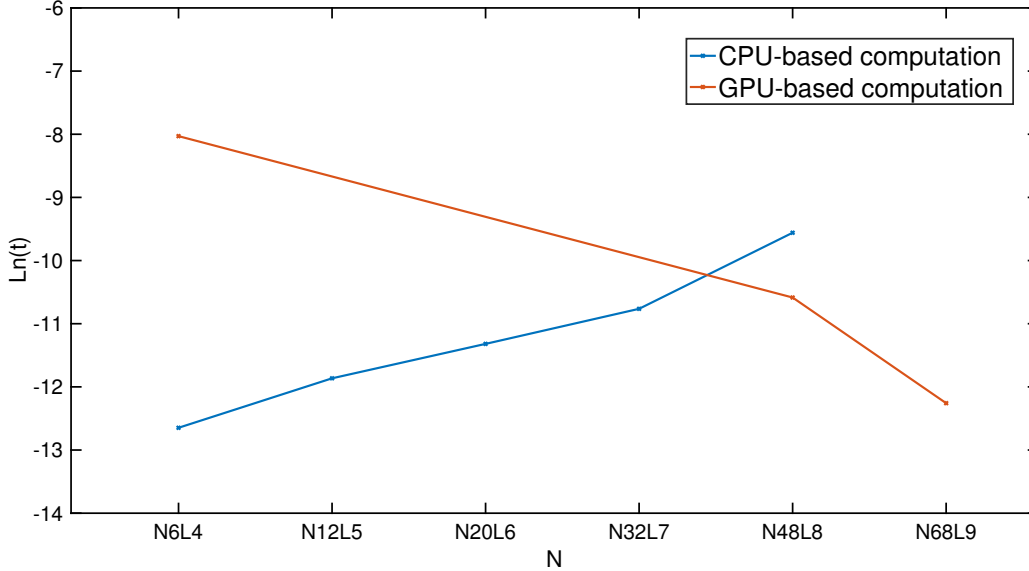


Figure 4.8: Logarithm of the computation time per particle per unit volume for updating auxiliary field $s(\mathbf{n}, n_t)$ at all spatial points at certain time step.

and only propagate the up-spin fermion wave functions, but generate the corresponding down-spin parts by using $T = -i\sigma_y K$. In this way, we can reduce the GPU memory requirement by up to 75% for our algorithms.

4.3 Superfluidity in the unitary limit

According to BCS theory [60], ultracold fermions close to the Fermi surface can form Cooper pairs if an arbitrarily weak (effective) attraction is present and hence a fermionic superfluid appears. When the interaction is smoothly increased until the pairs are tightly bound, the bosonic pairs must follow Bose-Einstein statistics and a bosonic condensate emerges. It is believed that the crossover from the BCS superfluid to the Bose-Einstein condensate is smooth and the physics at Feshbach resonance is universal. In this section, we will study the superfluid phase at unitarity in a dilute ultracold Fermi gas.

4.3.1 One- and two-body density matrices

The occurrence of the off-diagonal long-range order (ODLRO) in one- and two-body density matrices was investigated by C.N. Yang in interacting systems of bosons and fermions [165]. ODLRO of two-body density matrix is often used to characterize the superfluid phase in Fermi systems. For a system of spin-1/2 fermions, the coordinate-space two-body density matrix (TBDM) can be written as

$$\rho_2(\mathbf{r}'_1, \mathbf{r}'_2, \mathbf{r}_1, \mathbf{r}_2) = \langle a_{\uparrow}^{\dagger}(\mathbf{r}'_1) a_{\downarrow}^{\dagger}(\mathbf{r}'_2) a_{\downarrow}(\mathbf{r}_2) a_{\uparrow}(\mathbf{r}_1) \rangle, \quad (4.5)$$

where $a_{\sigma}^{\dagger}(\mathbf{r})$, $a_{\sigma}(\mathbf{r})$ denote the creation and annihilation operators of a fermion at site \mathbf{r} with spin σ . The one-body density matrix (OBDM) for spin σ is defined, analogously:

$$\rho_{1,\sigma}(\mathbf{r}', \mathbf{r}) = \langle a_{\sigma}^{\dagger}(\mathbf{r}') a_{\sigma}(\mathbf{r}) \rangle. \quad (4.6)$$

For fermions, $\rho_{1,\sigma}(\mathbf{r}', \mathbf{r})$ vanishes [166, 167] as $|\mathbf{r} - \mathbf{r}'| \rightarrow \infty$, since there is no long-range correlation for fermions. One example is the He II phase of liquid He. In molecular Bose-Einstein condensate, on the other hand, the long-range order of $\rho_{1,\sigma}(\mathbf{r}', \mathbf{r})$ is nonzero.

For ultracold Fermi gas in the unitary limit, we measure the spatial pair correlation to characterize the superfluid phase. When the primed and unprimed coordinates are far apart, a non-vanishing $\rho_2(\mathbf{r}'_1, \mathbf{r}'_2, \mathbf{r}_1, \mathbf{r}_2)$ indicates the existence of a superfluid phase. We can perform a spectral decomposition of the TBDM,

$$\rho_2(\mathbf{r}'_1, \mathbf{r}'_2, \mathbf{r}_1, \mathbf{r}_2) = \alpha N/2 \phi^*(|\mathbf{r}'_1 - \mathbf{r}'_2|) \phi(|\mathbf{r}_1 - \mathbf{r}_2|), \quad (4.7)$$

where $\phi^*(|\mathbf{r}'_1 - \mathbf{r}'_2|)$, $\phi(|\mathbf{r}_1 - \mathbf{r}_2|)$ are the normalized wave functions of the condensate state of pairs. α is a constant defined as the percentage of pairs in condensation, the so-called condensate fraction. When the primed and unprimed coordinates are at intermediate separation or close to each other, a residual component appears in the decomposition due to the single particle correlation. Therefore, in the vicinity of $|\mathbf{r}'_1 - \mathbf{r}_1| = |\mathbf{r}'_2 - \mathbf{r}_2| = 0$, the contribution of the product $\rho_{1,\uparrow}(\mathbf{r}'_1, \mathbf{r}_1)\rho_{1,\downarrow}(\mathbf{r}'_2, \mathbf{r}_2)$ should be taken into account. We will discuss this in section 4.3.2.

To study the long-range order of the TBDM, let us consider the case where $|\mathbf{r}'_1 - \mathbf{r}'_2| = |\mathbf{r}_1 - \mathbf{r}_2| = 0$. Since the ground state is translationally invariant ($\mathbf{P} = 0$), we measure the pair correlation function (PCF) with $\mathbf{r}'_1 = \mathbf{r}'_2 = 0$,

$$\rho_2(\mathbf{r}) = \langle a_{\uparrow}^{\dagger}(\mathbf{r})a_{\downarrow}^{\dagger}(\mathbf{r})a_{\downarrow}(\vec{0})a_{\uparrow}(\vec{0}) \rangle. \quad (4.8)$$

Note that the pair correlation function only depends on \mathbf{r} . In Fig. 4.9, we show the renormalized correlation function

$$\rho'_2(\mathbf{r}) = \frac{1}{\Gamma}\rho_2(\mathbf{r}), \quad (4.9)$$

where $\Gamma = \langle a_{\uparrow}^{\dagger}(\vec{0})a_{\downarrow}^{\dagger}(\vec{0})a_{\downarrow}(\vec{0})a_{\uparrow}(\vec{0}) \rangle$. We make measurements in lattices of different volumes, with L from 5 through 11. Each measurement is averaged over different directions on the lattice, so ρ'_2 is plotted as a function of r ($= |\mathbf{r}|$), which is the distance between two points in lattice. It is obvious that there is no long-range correlation for non-interacting systems, while for interacting fermions the PCF does not decay to zero at long range of r . Interacting systems with different volumes all have a plateau at a nonzero value. Since we have averaged the measurements over all directions, we check if the plateau is still there along one single direction. In the lattice, we choose two different directions for the calculations. The first

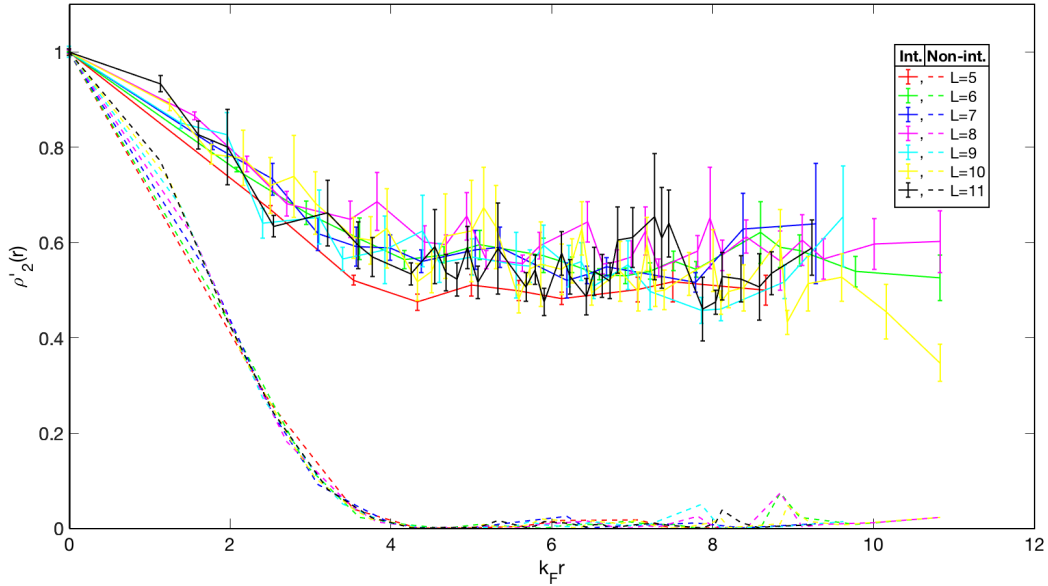


Figure 4.9: Renormalized pair correlation function of interacting (solid curves) and non-interacting (dashed curves) ultracold Fermi gas at unitarity. Systems in same lattice, with or without interaction, are plotted with same color.

one is along a certain axis, like $(0, 0, \pm 1)$, $(0, \pm 1, 0)$, or $(\pm 1, 0, 0)$. The second direction is along a diagonal, such as $(0, \pm 1, \pm 1)$, $(\pm 1, 0, \pm 1)$ and $(\pm 1, \pm 1, 0)$. We report the results in Fig. 4.10 for two lattice volumes, $L = 10$ and $L = 11$. Both lattices see the non-vanishing long-range order of PCF, and in each lattice the same pattern appears along both the axis and the diagonal. This confirms the existence of a superfluid phase in the ultracold Fermi gas at unitarity.

4.3.2 Condensate fraction

According to C. N. Yang's work [165], the ODLRO in the two-body density matrix can be used to calculate the condensate fraction α . In Eq. (4.8), we set $\mathbf{r}'_1 = \mathbf{r}_1 + \mathbf{r}$ and $\mathbf{r}'_2 = \mathbf{r}_2 + \mathbf{r}$ and obtain

$$\rho_2(\mathbf{r}, \mathbf{r}_1, \mathbf{r}_2) = \alpha N/2 \phi^*(|(\mathbf{r}_1 + \mathbf{r}) - (\mathbf{r}_2 + \mathbf{r})|) \phi(|\mathbf{r}_1 - \mathbf{r}_2|). \quad (4.10)$$

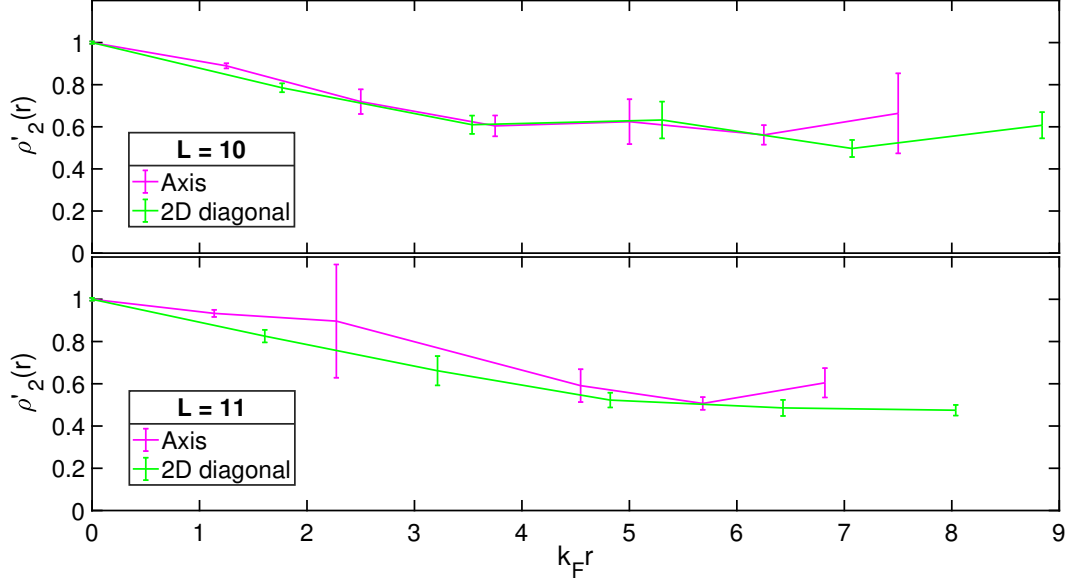


Figure 4.10: Renormalized pair correlation function along two particular directions: axial direction and 2D diagonal direction. The upper panel is for $L = 10$ and the lower one for $L = 11$.

Since $\phi^*(|\mathbf{r}_1 - \mathbf{r}_2|)$, $\phi(|\mathbf{r}_1 - \mathbf{r}_2|)$ are normalized wave functions, we can integrate over both \mathbf{r}_1 and \mathbf{r}_2 on both sides of the equation,

$$\begin{aligned} \int \rho_2(\mathbf{r}, \mathbf{r}_1, \mathbf{r}_2) d\mathbf{r}_1 d\mathbf{r}_2 &= \alpha N/2 \int |\phi(|\mathbf{r}_1 - \mathbf{r}_2|)|^2 d\mathbf{r}_1 d\mathbf{r}_2 \\ &= \alpha \frac{N}{2}. \end{aligned} \quad (4.11)$$

Therefore, the condensate fraction α can be obtained from the projected TBDM, defined as [168, 169]

$$h(\mathbf{r}) = \frac{2}{N} \int \rho_2(\mathbf{r}, \mathbf{r}_1, \mathbf{r}_2) d\mathbf{r}_1 d\mathbf{r}_2, \quad (4.12)$$

where

$$\rho_2(\mathbf{r}, \mathbf{r}_1, \mathbf{r}_2) = \langle a_{\uparrow}^{\dagger}(\mathbf{r}_1 + \mathbf{r}) a_{\downarrow}^{\dagger}(\mathbf{r}_2 + \mathbf{r}) a_{\uparrow}(\mathbf{r}_1) a_{\downarrow}(\mathbf{r}_2) \rangle. \quad (4.13)$$

The projected TBDM $h(\mathbf{r})$ will converge to condensate fraction α in the limit $|\mathbf{r}| \rightarrow \infty$. As mentioned above, in the neighborhood of $|\mathbf{r}'_1 - \mathbf{r}_1| = |\mathbf{r}'_2 - \mathbf{r}_2| = 0$, the decomposition of TBDM has contributions from $\rho_{1,\uparrow}(\mathbf{r}'_1, \mathbf{r}_1)\rho_{1,\downarrow}(\mathbf{r}'_2, \mathbf{r}_2)$. Setting $\mathbf{r}'_1 = \mathbf{r}_1 + \mathbf{r}$ and $\mathbf{r}'_2 = \mathbf{r}_2 + \mathbf{r}$, we obtain

$$\rho_{1,\uparrow}(\mathbf{r}, \mathbf{r}_1) = \langle a_{\uparrow}^{\dagger}(\mathbf{r}_1 + \mathbf{r})a_{\uparrow}(\mathbf{r}_1) \rangle, \quad (4.14)$$

$$\rho_{1,\downarrow}(\mathbf{r}, \mathbf{r}_2) = \langle a_{\downarrow}^{\dagger}(\mathbf{r}_2 + \mathbf{r})a_{\downarrow}(\mathbf{r}_2) \rangle. \quad (4.15)$$

The choices of \mathbf{r}_1 and \mathbf{r}_2 are independent and arbitrary, since the one-body correlation function (OCF) only depends on \mathbf{r} . Consequently, we can omit \mathbf{r}_1 and \mathbf{r}_2 in the OCF and write $\rho_{1,\uparrow}(\mathbf{r})$ and $\rho_{1,\downarrow}(\mathbf{r})$ instead. Let us define the residual of projected TBDM $h_{res}(\mathbf{r})$,

$$\begin{aligned} h_{res}(\mathbf{r}) &= \frac{2}{N} \int \left[\rho_2(\mathbf{r}, \mathbf{r}_1, \mathbf{r}_2) - \rho_{1,\uparrow}(\mathbf{r}, \mathbf{r}_1)\rho_{1,\downarrow}(\mathbf{r}, \mathbf{r}_2) \right] d\mathbf{r}_1 d\mathbf{r}_2 \\ &= h(\mathbf{r}) - \frac{2}{N} [\rho_1(\mathbf{r})L^3]^2, \end{aligned} \quad (4.16)$$

where we use $\rho_{1,\uparrow}(\mathbf{r}) = \rho_{1,\downarrow}(\mathbf{r}) = \rho_1(\mathbf{r})$, since the spatial parts of the wave functions for the two spin species are exactly the same. We calculate the projected TBDM, $h(r)$, the contribution from OCF, $\frac{2}{N}[\rho_1(\mathbf{r})L^3]^2$, and the residual of projected TBDM, $h_{res}(r)$ and report them in Fig. 4.11 for sufficiently large Euclidean projection time t . The dashed lines show that the asymptotic behavior of $h(r)$ is stable at a nonzero value, while OCF, shown in triangle symbols, decays to zero at long range of r . Consequently, $h(r)$ reveals the condensate fraction α in the limit $r \rightarrow \infty$. At small r , $h(r)$ is not even close to the condensate fraction, but the residual projected TBDM (in solid line), $h_{res}(r)$, provides as a good estimate of α over a wide range of r .

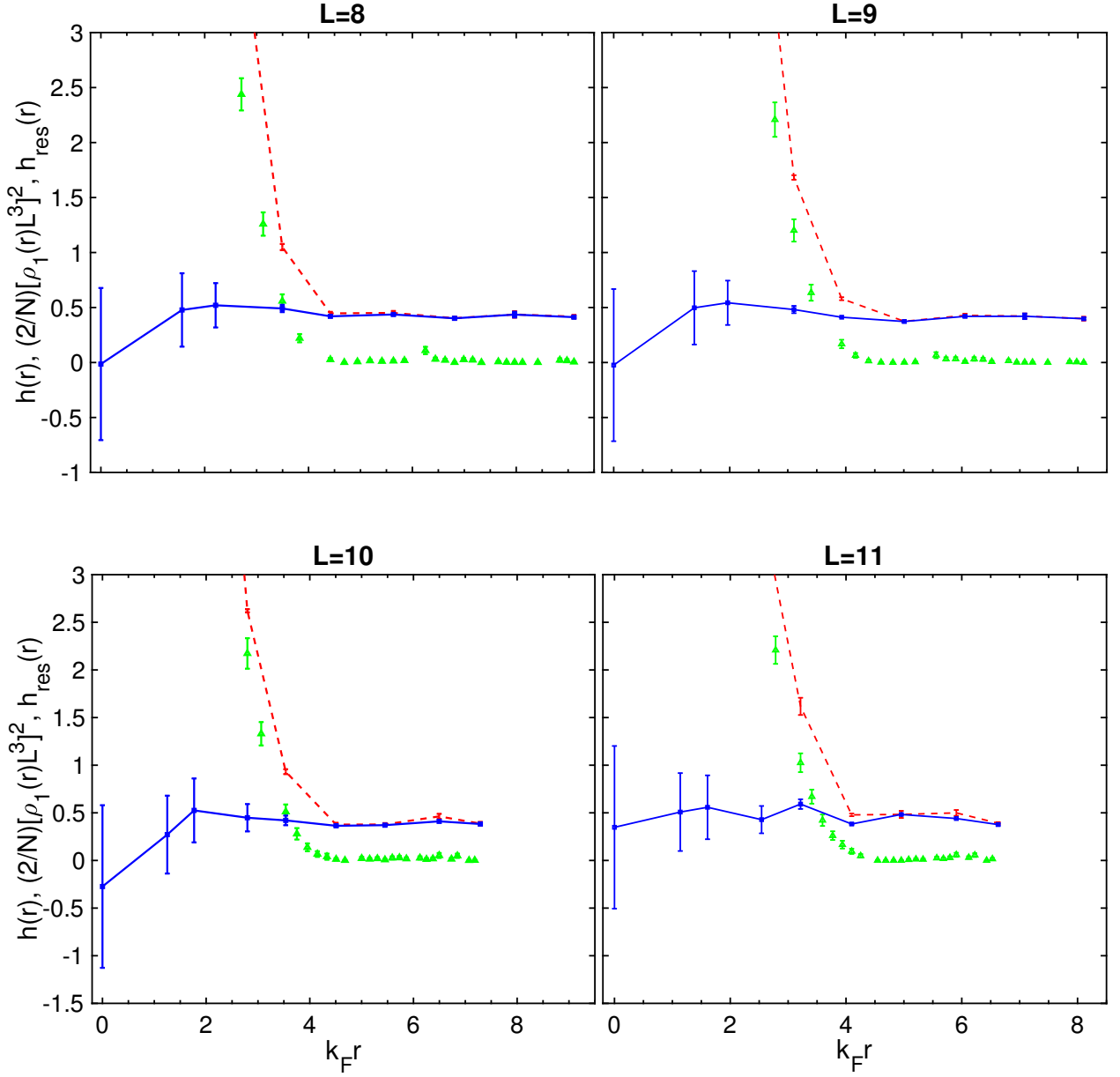


Figure 4.11: Projected TBDM, $h(r)$, (dashed lines), $(2/N)[\rho_1(r)L^3]^2$ (triangle symbols) and $h_{res}(r)$ (solid lines) for different lattice volumes: $L = 8$ (upper left), $L = 9$ (upper right), $L = 10$ (lower left) and $L = 11$ (lower right). All calculations are performed at large Euclidean projection time t .

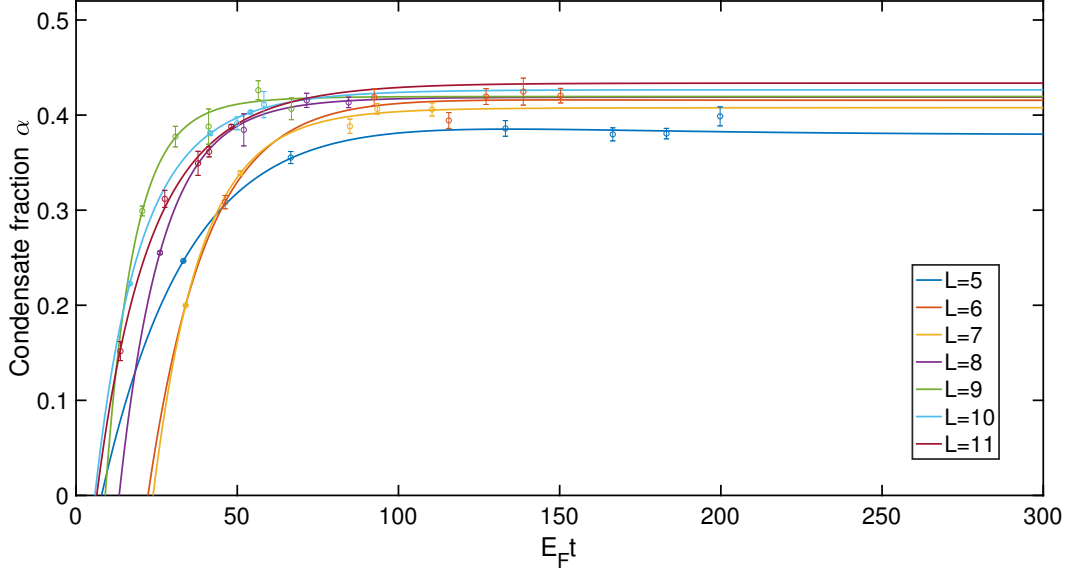


Figure 4.12: Condensate fraction α for various L and fitted curves extrapolated to large projection time t . Note that we use $E_F t$ instead of t as horizontal axis.

The pattern is the same for different lattice sizes and the estimates of the condensate fraction are quite stable at large r . The calculations of OBDM and TBDM are all based on Euclidean time projection, therefore the estimates of condensate fraction α should be a function of the projection time t . In Fig. 4.12, we show the condensate fraction for various lattice volumes and extrapolate the measurements to infinite projection time. The extrapolation function uses Eq. (3.93):

$$\alpha(t) = \alpha_{t=\infty} + ce^{-(E_{N,N}^1 - E_{N,N}^0)\frac{t}{2}} + de^{-(E_{N,N}^1 - E_{N,N}^0)t}, \quad (4.17)$$

where the excitation energy $E_{N,N}^1 - E_{N,N}^0$ is already known from the fitting of Bertsch parameter in sec. 4.2.2. For each lattice size, we only have three unknown parameters to fit. This allows us to extract $\alpha_{t=\infty}$, the condensate fraction at infinite projection time.

Since the condensate fractions are all calculated in finite lattice volumes, we also study

the extrapolation towards infinite lattice size $L \rightarrow \infty$ (see table 4.4). We use an extrapolation function of form $A\rho + B\rho^{4/3} + \alpha$, where B is allowed to be zero. We use the least-squares method to fit the data with 1σ error and compute the reduced chi-squared, χ^2/DOF , for each fitted curve. In Fig. 4.13, we report the calculated condensate fraction as a function of the density ρ , where $\rho = N(aL)^{-3}$. Our results are in agreement with the experiments reported in Refs. [170,171], in which the initial pair condensate fraction is $46\% \pm 7\%$ before a magnetic field ramp is applied. A high condensate fraction of up to 80% is observed due to the short-range atom pairs and the transfer from condensed fermion pairs into molecules. Based on the BCS theory the zero-temperature calculations [169,172] agree with the result of fixed-node diffusion Monte Carlo [173] that incorporates BCS-type wave function into the trial wave function, while our result is lower than their calculations at unitary limit. For the diffusion Monte Carlo calculation using one-sided BCS-Jastrow guiding wave functions [162], the condensate fraction is estimated to be 0.56(1), but is still a bit higher than our results.

We have measured the condensate fraction α according to Eq. (4.12), where the identity $\int |\phi(|\mathbf{r}_1 - \mathbf{r}_2|)|^2 d\mathbf{r}_1 d\mathbf{r}_2 = 1$ is used, but the details of the pair wave function $\phi(|\mathbf{r}_1 - \mathbf{r}_2|)$ have not been discussed yet. Let us consider the calculation of integral $\int |\phi(|\mathbf{r}_1 - \mathbf{r}_2|)|^2 d\mathbf{r}_1 d\mathbf{r}_2$, where \mathbf{r}_1 and \mathbf{r}_2 are independent of each other. In our discrete lattice, the integral should

Table 4.4: Condensate fraction at unitary limit extrapolated to infinite volume for fixed particle number $N = 66$ with different fitting functions.

Function	A	B	α	err	χ^2/DOF
$A\rho + B\rho^{4/3} + \alpha$	-0.7750	0.0623	0.4319	0.0109	0.9
$A\rho + \alpha$	-0.7474		0.4317	0.0047	0.7

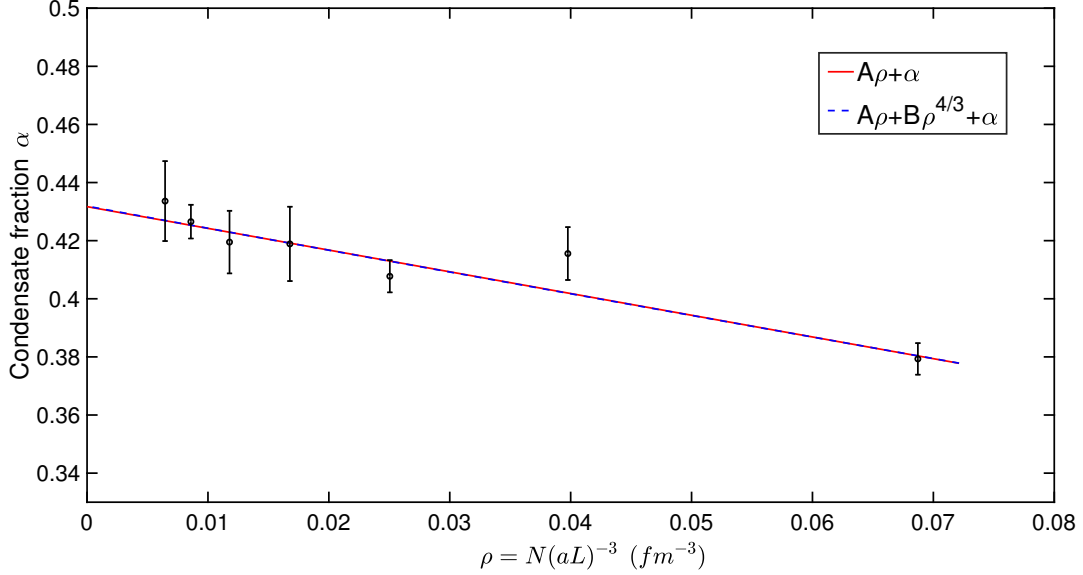


Figure 4.13: Condensate fraction α extrapolated to infinite volume of lattice with different functions of density ρ .

be calculated as

$$\sum_{\mathbf{n}_1, \mathbf{n}_2} |\phi(|\mathbf{n}_1 - \mathbf{n}_2|)|^2 = \sum_{\mathbf{n}} \sum_{\mathbf{r}} |\phi(|\mathbf{r}|)|^2, \quad (4.18)$$

which gives us two evaluation methods. One is to calculate the summation over the lattices sites denoted by \mathbf{n}_1 and \mathbf{n}_2 independently. The other one is to sum over the lattice site labeled by \mathbf{n} , and for each site of \mathbf{n} the summation is made over its neighbors characterized by the relative distance \mathbf{r} . Since the pair wave function only depends on the relative distance, the two ways of calculation are equivalent. In Fig. 4.14, we show the pair wave functions in various lattices at large projection time t .

Evaluating Eq. (4.19) further, we have

$$\sum_{\mathbf{n}} \sum_{\mathbf{r}} |\phi(|\mathbf{r}|)|^2 = \Omega \sum_{\mathbf{r}} |\phi(|\mathbf{r}|)|^2, \quad (4.19)$$

where Ω is the volume of the lattice. We can think of the squared pair wave function as the

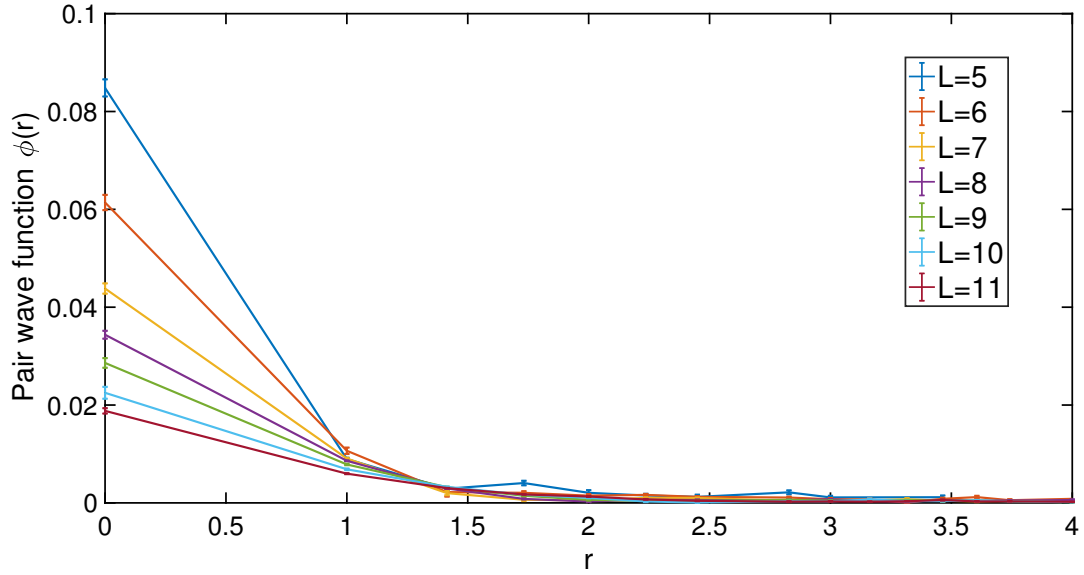


Figure 4.14: Radial part of the pair wave function, $\phi(r)$, for a pair of fermions with distance r in different lattices. Our measurements are made at large projection time t .

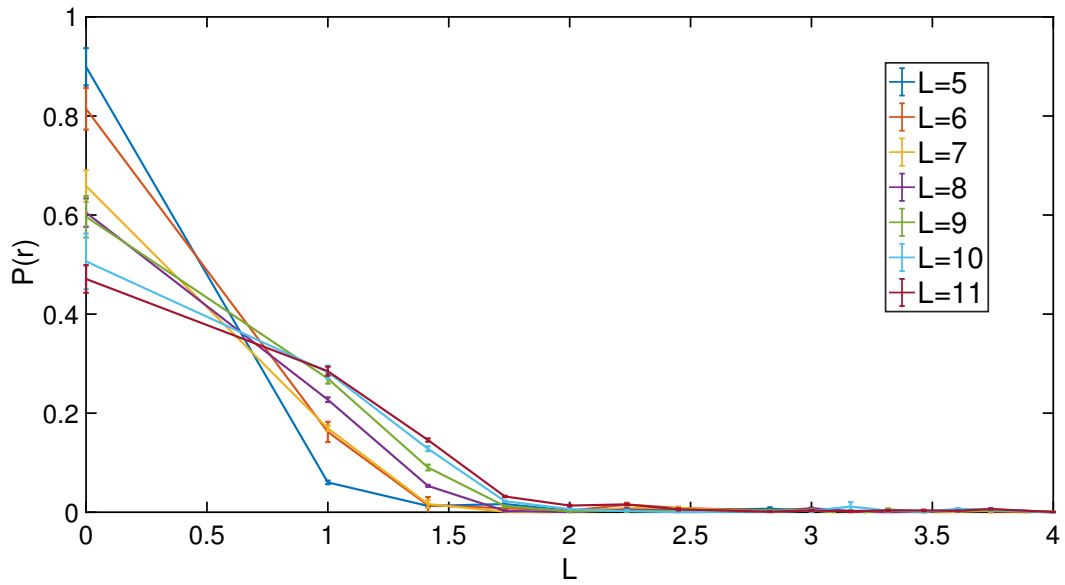


Figure 4.15: The probability of finding a pair of fermions with size r . Our measurements are made at large projection time t .

probability of finding a pair of fermions with relative coordinate \mathbf{r} , if it is normalized to one.

Let us define the normalized pair wave function,

$$\Phi(|\mathbf{r}|) = \frac{1}{\sqrt{\Omega}}\phi(|\mathbf{r}|), \quad (4.20)$$

and the probability of observing a pair with relative distance r between two fermions,

$$P(r) = \sum_{|\mathbf{r}|=r} |\Phi(|\mathbf{r}|)|^2. \quad (4.21)$$

In Fig. 4.15, we show the probability $P(r)$ as a function of r in lattice units. The probability distributions all peak at $r = 0$ and decay to zero as r becomes large, which indicate a finite size of the fermion pairs. Focusing on the shape of $P(r)$, when the peak is higher, it decays faster, which implies a smaller size of the pairs and this corresponds to a smaller L . Since we fix the total number of particles, a smaller L means a denser system. In conclusion, smaller size of the fermion pairs is expected in denser systems. As mentioned in the introduction, the pair size should be proportional to k_F^{-1} in the unitary limit. To quantify this relation, we calculate the expectation value of the size using $P(r)$,

$$\langle r_{pair} \rangle = \sum_r r P(r), \quad (4.22)$$

where r is the separation between two fermions in a pair. Note that all points at $\mathbf{r} = r$ count as one (see the definition of $P(r)$ in Eq. (4.22)). The measured fermion pair sizes are reported in Fig. 4.16, where the dependence of measured observables on the projection time

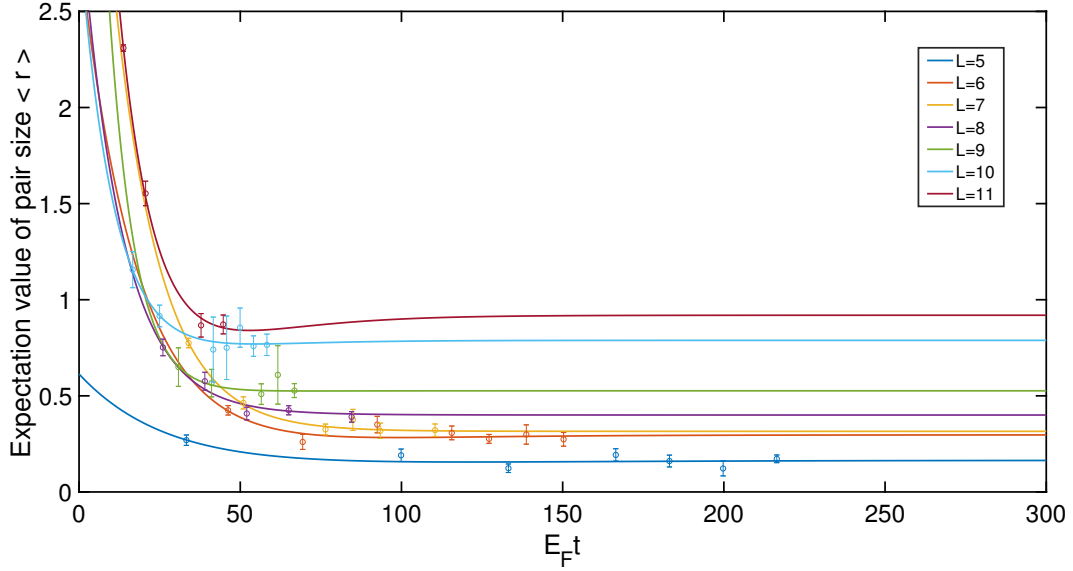


Figure 4.16: Expectation value of fermion pair size as a function of projection time t with various lattice volumes.

t is considered:

$$\langle r_{pair}(t) \rangle = ae^{-\frac{(E_{N,N}^1 - E_{N,N}^0)t}{2}} + be^{-(E_{N,N}^1 - E_{N,N}^0)t} + \langle r_{pair}(t = \infty) \rangle. \quad (4.23)$$

The excitation energy is already known from the fitting of Bertsch parameters⁵. In the limit $t \rightarrow \infty$, the pair size is estimated by $\langle r_{pair}(t = \infty) \rangle$ and the results in different volumes agree with our expectation that denser systems have smaller pair size. In Fig. 4.17, we show $\langle r_{pair}(t = \infty) \rangle$ as a function of k_F^{-1} . It is clear that pair size is monotonically increasing with k_F^{-1} , but the relation is not linear. The reason is that the pair wave function $\Phi(|\mathbf{r}|)$ at short range r strongly depends on the lattice size. We use a function of the form $c \frac{\exp[-2r/\zeta_p]}{r^2}$ to fit $|\Phi(r)|^2$ at $r \neq 0$, where ζ_p denotes the pair size and c carries the overall amplitude of the

⁵See appendix for derivation of the form of fitting function

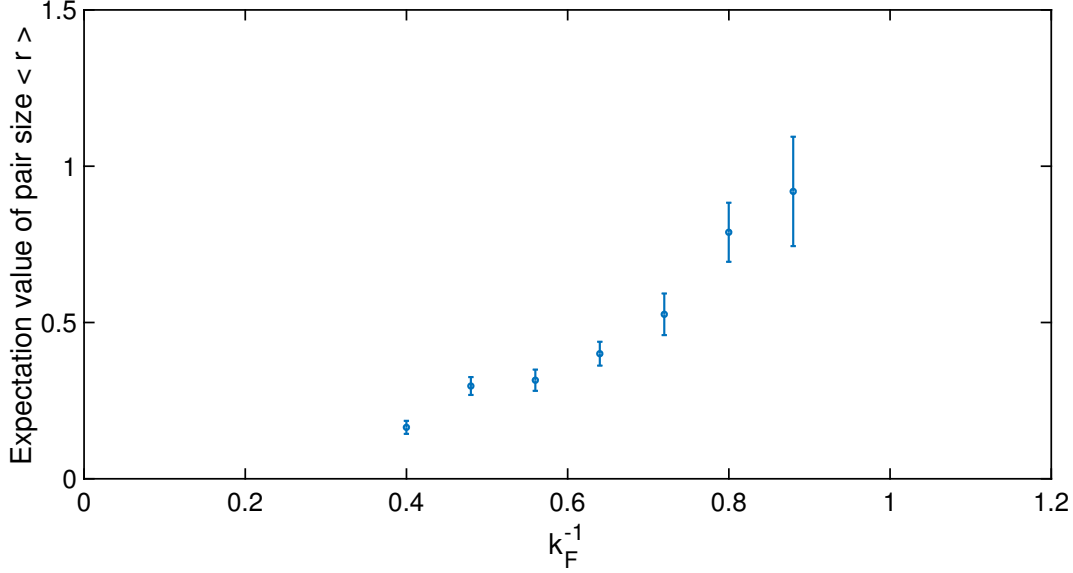


Figure 4.17: Expectation value of pair size as a function of inverse Fermi momentum k_F^{-1} . Our measurements are made at large projection time t and the values are all in lattice units.

function. Accounting for our finite lattice spacing, the following form is used in practice,

$$|\Phi(\mathbf{r})|^2 = \left| \frac{c}{L^3} \sum_{\mathbf{k}} e^{i\mathbf{k}\cdot\mathbf{r}} \frac{4\pi}{\mathbf{k}^2 + \zeta_p^{-2}} \right|^2, \quad (4.24)$$

where \mathbf{k} is the momentum in the inverse space of our lattice⁶. Since our calculation directly yields the square of the pair wave function, a squared form is used in the equation above. We report ζ_p as a function of the projection time t for various sizes of the lattice in Fig. 4.18. For all lattices of different sizes, ζ_p shows clear convergence as projection time t becomes long enough. The relative heights of the plateaus also reveal that more dilute systems have bigger pair sizes.

Since the inter-particle separation or equivalently the inverse of Fermi momentum is the only length scale in the unitary limit, the size of the fermion pairs should be proportional to k_F^{-1} by a universal constant. To extract this constant, we consider the ratio ζ_p/k_F^{-1} and use

⁶See table 4.1 for the possible momenta in the lattice

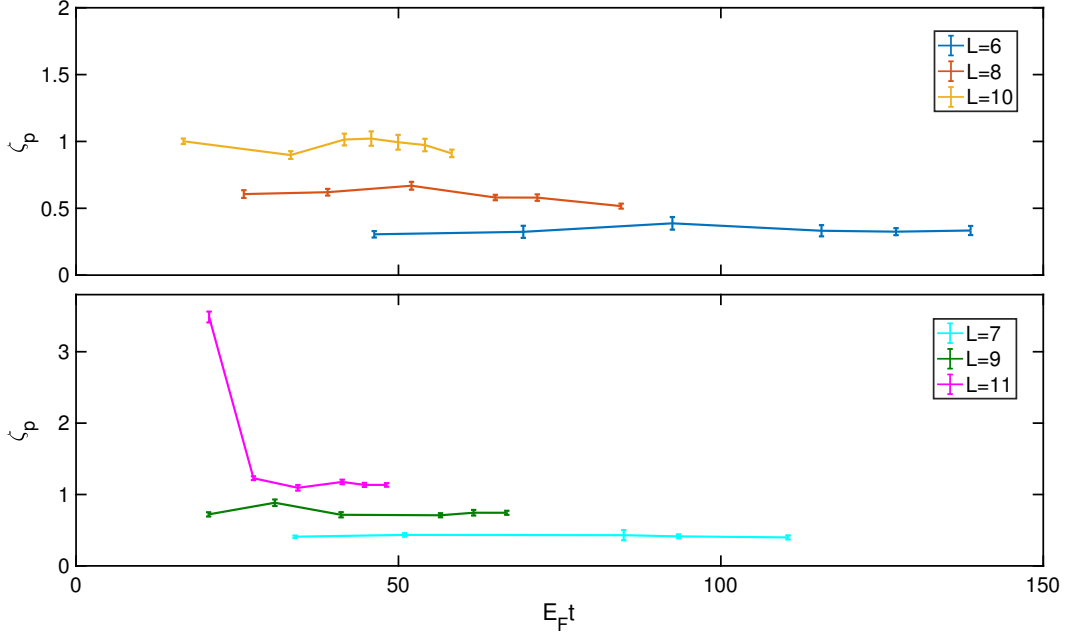


Figure 4.18: Parameter ζ_p as a function of projection time t for various lattice sizes. All values are in lattice units.

a fitting function of the form $\zeta_p k_F = A + B k_F$. In Fig. 4.19, $\zeta_p k_F$ is shown as a function of k_F and the pair sizes are all measured at sufficiently long projection time. In the infinite-volume limit, the universal constant $\zeta_p k_F$ is found and the fitted parameters are listed in table 4.5. The method of least squares is used here and the reduced chi-squared χ^2/DOF appears close to one which means our fit is very good. We believe that the tiny value of parameter B comes from the limited number of particles and the effect of a finite volume.

Table 4.5: $\zeta_p k_F$ as a linear function of the Fermi momentum k_F with fixed particle number $N = 66$.

Function	A	B	err _A	err _B	χ^2/DOF
$A + B k_F$	1.9305	-0.0064	0.0913	0.0006	1.1

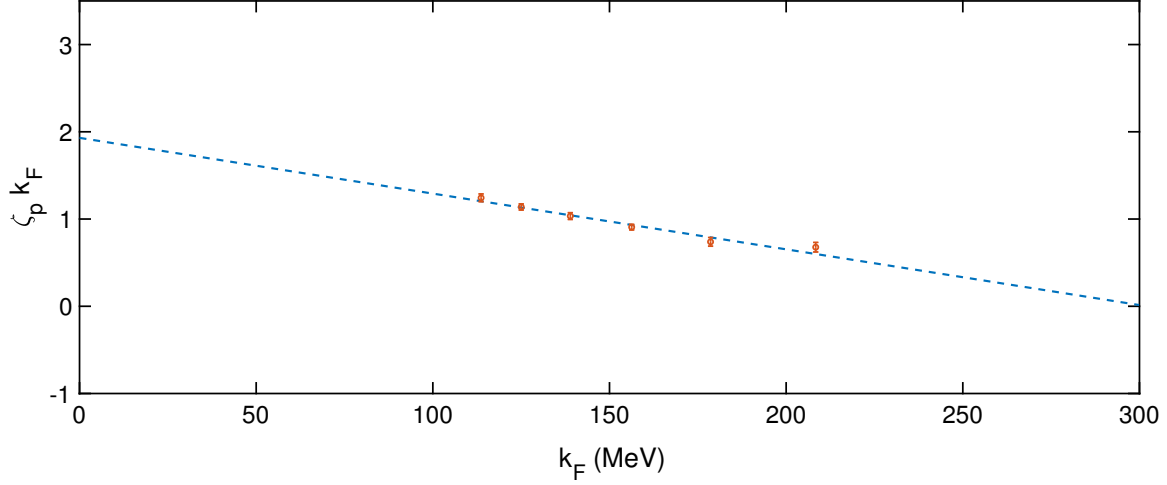


Figure 4.19: Values of $\zeta_p k_F$ as a function of k_F . All calculations are made at large projection time t .

4.4 Fulde-Ferrell-Larkin-Ovchinnikov phase

4.4.1 One-dimensional system

Let us consider a periodic one-dimensional system of two-component fermions. The lattice size is L and the total number of particles is N , with spin up N_\uparrow and spin down N_\downarrow . A contact interaction is considered for up and down spins and the full Hamiltonian is written as

$$H = H_{free} + c_0 \sum_{i=0}^{L-1} \rho_\uparrow(i) \rho_\downarrow(i), \quad (4.25)$$

where $\rho_\sigma [= a_\sigma^\dagger(i) a_\sigma(i)]$ is the single particle density of spin σ at site i . For the free Hamiltonian H_{free} , the nearest-neighbor hopping terms are taken into account and we write

$$H_{free} = -\frac{1}{2m} \sum_{\sigma=\uparrow,\downarrow} \sum_{i=0}^{L-1} [a_\sigma^\dagger(i+1) a_\sigma(i) + a_\sigma^\dagger(i) a_\sigma(i+1) - 2a_\sigma^\dagger(i) a_\sigma(i)]. \quad (4.26)$$

In our Hamiltonian, the interaction strength c_0 and the particle numbers N_\uparrow and N_\downarrow all can be tuned. We calculate the one-body and pair correlation functions in the ground state of this system. The one-body correlation function is defined as

$$G_\sigma(|i-j|) = \langle a_\sigma^\dagger(i) a_\sigma(j) \rangle, \quad (4.27)$$

and the pair correlation function is

$$G_{pair}(|i-j|) = \langle a_\uparrow^\dagger(i) a_\uparrow(j) a_\downarrow^\dagger(i) a_\downarrow(j) \rangle, \quad (4.28)$$

where i and j denote the sites on this one-dimensional lattice. The corresponding correlation functions in momentum space can be obtained by

$$n_\sigma(k) = \sum_l e^{-ikl} G_\sigma(l), \quad (4.29)$$

$$n_{pair}(k) = \sum_l e^{-ikl} G_{pair}(l), \quad (4.30)$$

respectively, where l is the distance between sites i and j .

In a periodic system, the particle momenta are quantized. The possible momenta for each spin are given by $\pm \frac{N-1}{2} \frac{2\pi}{L}$, with $N = 1, 2, \dots, N_\sigma$. N_σ is the number of particles of spin σ and its upper limit is L . Apparently, the Fermi momentum k_F for spin σ can be obtained by

$$k_F = \pm \frac{N_\sigma - 1}{2} \frac{2\pi}{L}. \quad (4.31)$$

Now we consider an spin-unpolarized system, $N_\uparrow = N_\downarrow = 15$, in one-dimensional lattice with $L = 32$. Calculations are made for the one-body and pair correlation functions at different

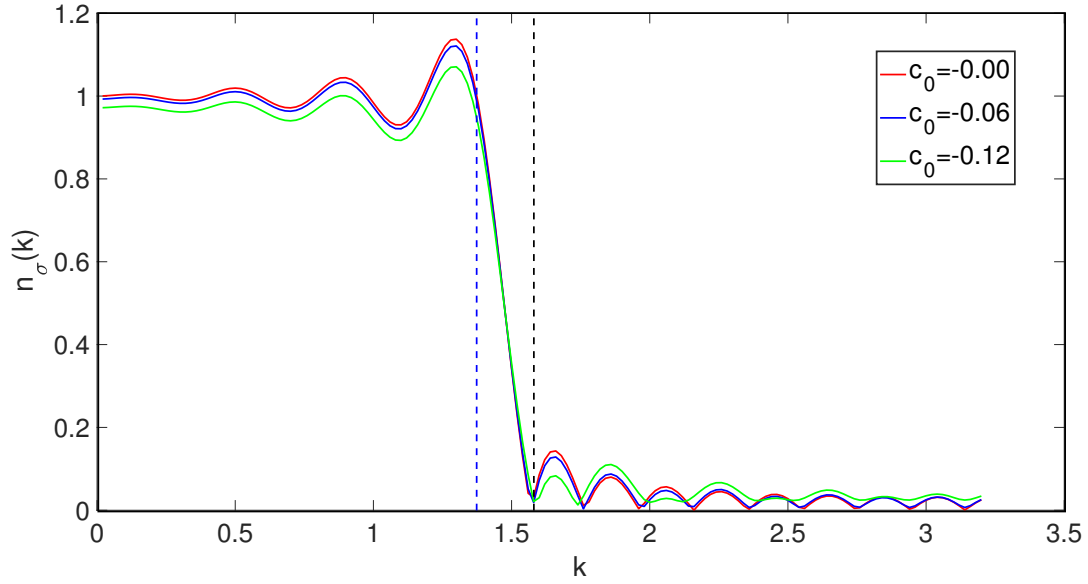


Figure 4.20: One-body correlation function in momentum space with $N_{\uparrow} = N_{\downarrow} = 15$ in an $L = 32$ one-dimensional lattice. The vertical dashed line in blue corresponds to the Fermi momentum k_F and the one in black indicates the momentum right above Fermi surface. All values are in lattice units.

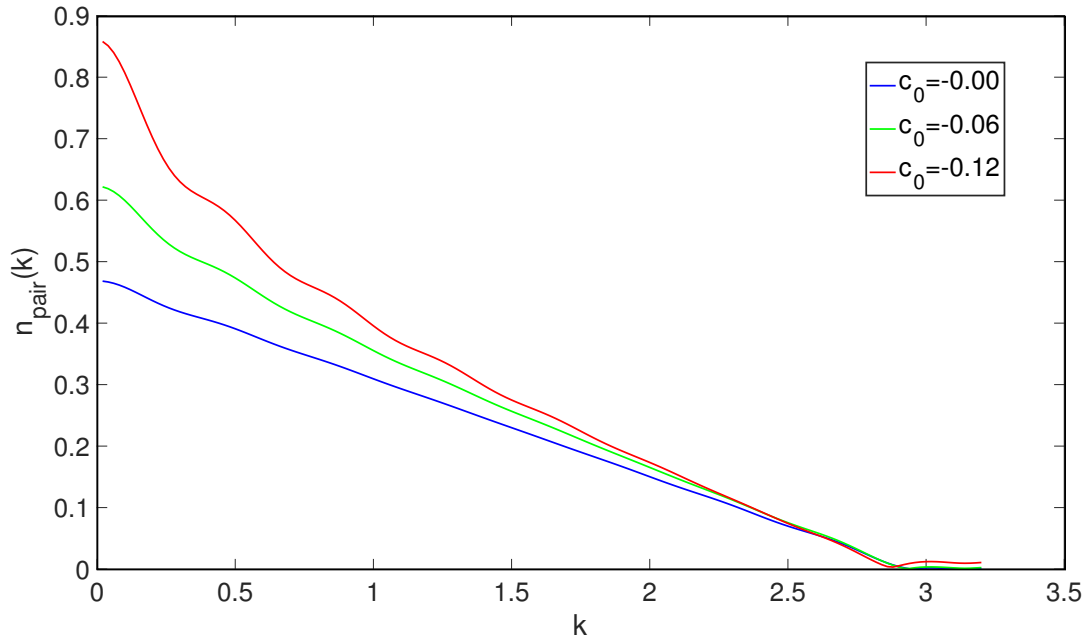


Figure 4.21: Pair correlation function in momentum space with $N_{\uparrow} = N_{\downarrow} = 15$ in an $L = 32$ one-dimensional lattice. All values are in lattice units.

values of the interaction strength c_0 . In Fig. 4.20, we show the momentum distribution of one spin species and the famous step function emerges. The vertical blue dashed line indicates the Fermi momentum where the step function starts to drop. The black dashed line corresponds to the momentum right above Fermi surface. It can be calculated by

$$k = \pm \frac{N_\sigma + 1}{2} \frac{2\pi}{L}. \quad (4.32)$$

For different strengths of the interaction, the momentum distribution remains the same for one-body correlation function. When it comes to the pair correlation function in k -space (Fig. 4.21), the total momentum of a pair peaks at $k = 0$ for all values of c_0 we tested. As the interaction becomes stronger, the peak is higher. A hand-waving explanation⁷ is that a strong interaction can connect fermions which lie deep in the Fermi sea. Thus, a stronger interaction yields a higher peak for the momentum distribution of the pairs. In the case of $c_0 = 0$, those deeply-lying fermions are much less active.

4.4.2 Order parameter

We have investigated the system of no spin polarization and found that the momenta of pairs always peak at zero for various strengths of the contact interaction. When the particle numbers of two spin species are not the same, their Fermi momenta are mismatched and the total momentum of a fermion pair should peak at a finite value. As illustrated in Fig. 4.22, when the Fermi momenta match for two spin species, the fermions with momenta close to k_{F1} (or k_{F2}) pair together with arbitrarily weak attractive interaction (shown in left panel). The momentum of formed pair is $-k_{F1} + k_{F2}$ or $-k_{F2} + k_{F1}$, which equals zero in this

⁷See rigorous derivation in Ref. [174].

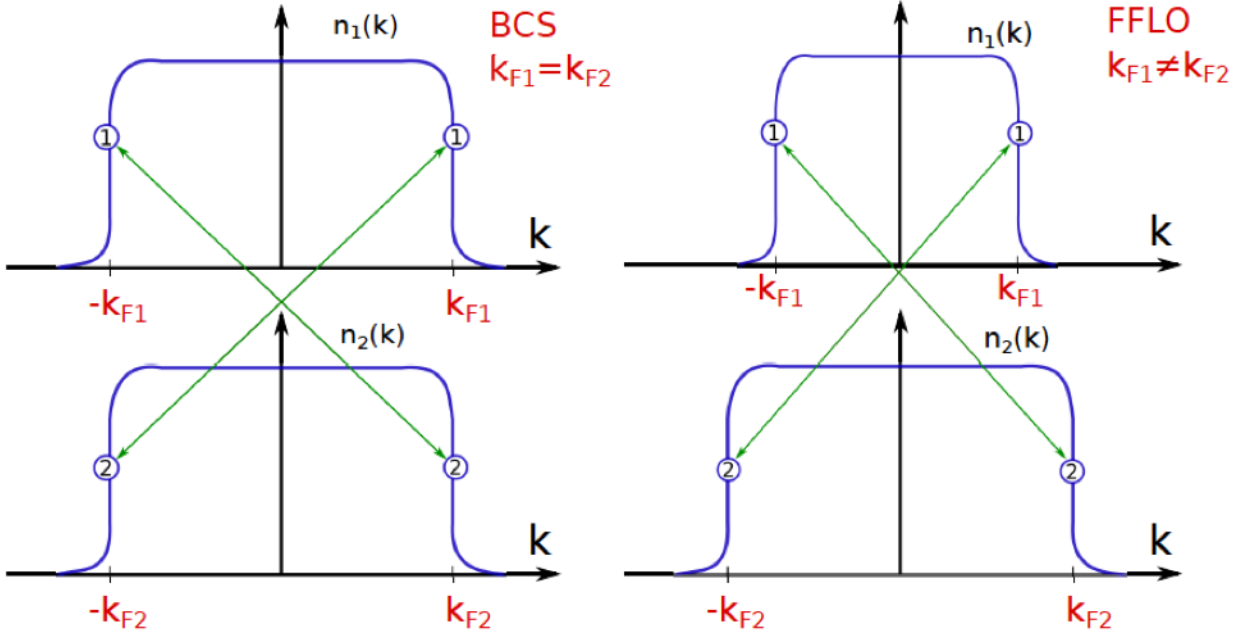


Figure 4.22: Fermion pair formation of unpolarized system (BCS theory) versus that of polarized system (FFLO phase) in momentum space [174].

case. In the right panel of Fig. 4.22, the Fermi surfaces of two spin species mismatch, and therefore a nonzero center of mass momentum appears for the fermion pair. The phase of these pairs is characterized by a spatially oscillating order parameter and named after Fulde and Ferrell and Larkin and Ovchinnikov (FFLO) [63,64]. The order parameter $\Delta(\mathbf{r})$ follows the equation from Ref. [64],

$$\Delta(\mathbf{r}) = \Delta_2 \cos(\mathbf{q} \cdot \mathbf{r}). \quad (4.33)$$

where \mathbf{q} is the wave vector and $q = \pm|k_{F1} - k_{F2}|$ in our one-dimensional system. We measure the pair correlation function in the polarized systems with N_\downarrow fixed to 15 and varying N_\uparrow . The results are shown in Fig. 4.23. Since the 1D lattice is periodic, plots are all symmetric with respect to the line at $|i - j| = \frac{L}{2}$. The pair correlation functions decay as $|i - j|$ becomes larger and, at the same time, they oscillate with specific periods. According to the

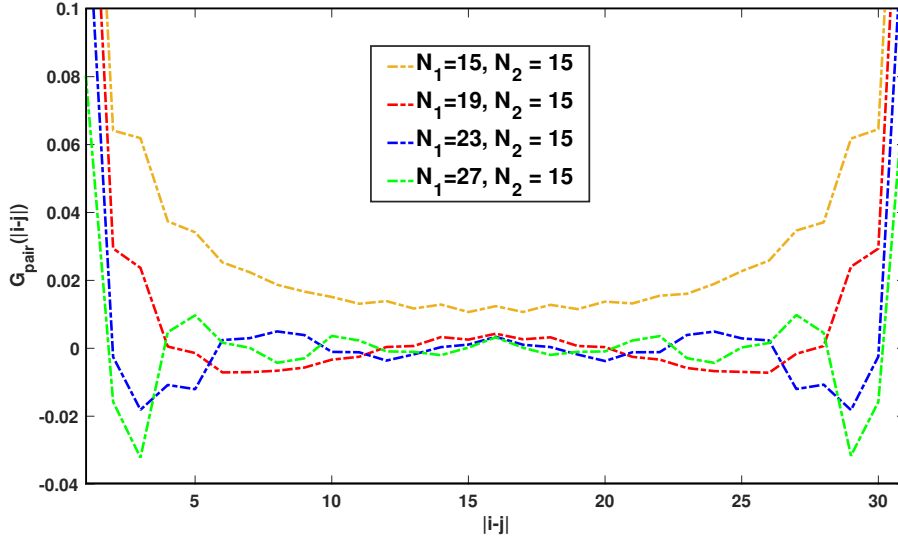


Figure 4.23: Pair correlation function in polarized systems with $N_{\downarrow} = 15$ and varying N_{\uparrow} . Our one-dimensional system uses the periodic boundary condition with $L = 32$ and $c_0 = -0.06$.

Eq. (4.31), the value of the wave vector \mathbf{q} is

$$q = \pm \frac{2\pi}{L} \left| \frac{N_{\uparrow} - N_{\downarrow}}{2} \right|. \quad (4.34)$$

Therefore, the oscillation period R_{Δ} can be calculated by

$$R_{\Delta} = \left| \frac{2\pi}{q} \right| = \frac{2L}{|N_{\uparrow} - N_{\downarrow}|}. \quad (4.35)$$

For instance, $N_{\uparrow} - N_{\downarrow} = 4$ and hence $R_{\Delta} = 16$, which matches the oscillation period of the red curve in Fig. 4.23. For the case of $N_{\uparrow} = N_{\downarrow}$, the period is infinite that exactly agrees with the curve in dark yellow. The amplitude of the oscillation will in general decay to zero with increased separation $|i - j|$, if there is no non-vanishing long-range order in the two-body density matrix.

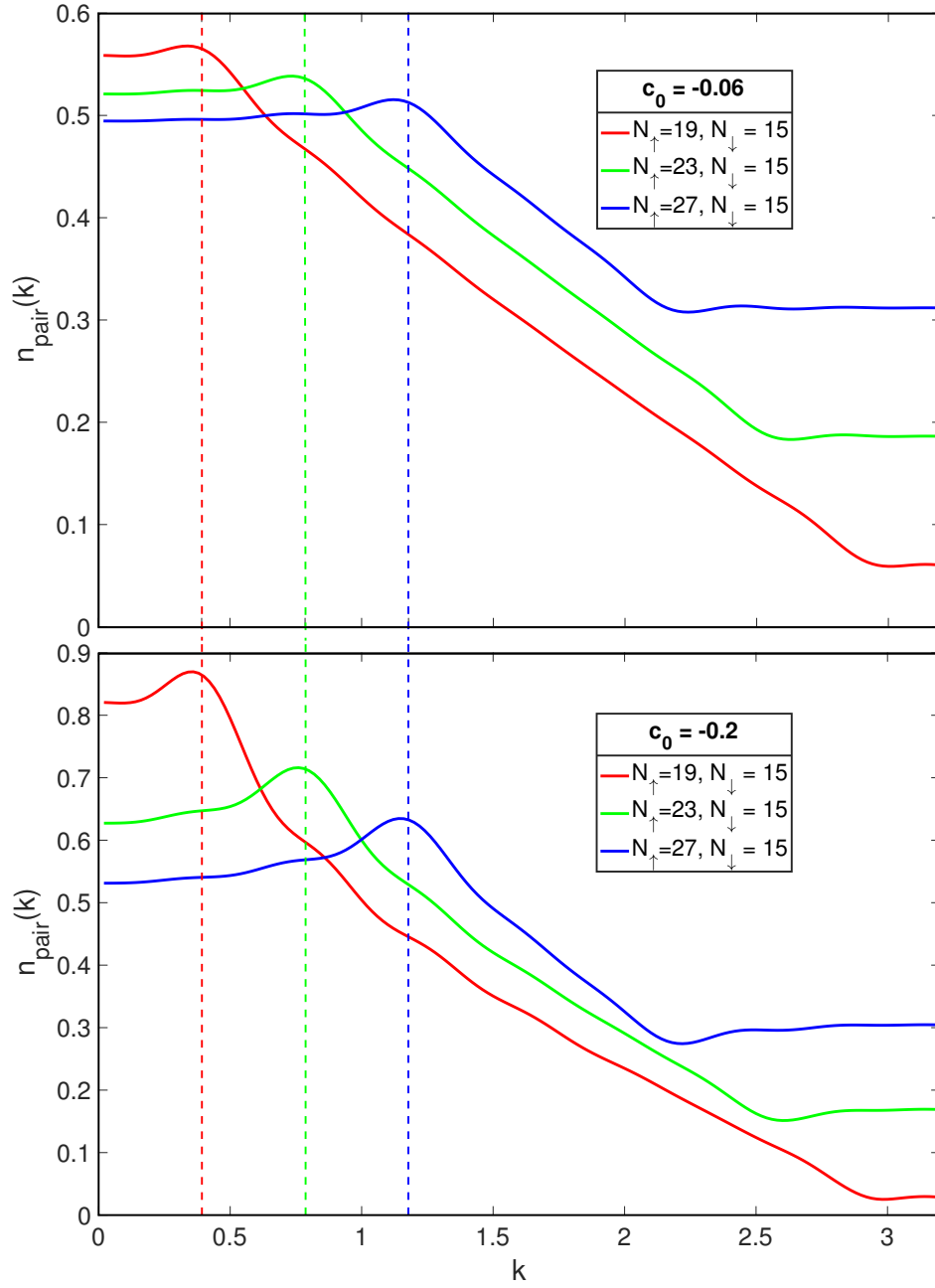


Figure 4.24: Pair correlation function in momentum space of the spin-polarized systems for different interaction strengths. All values are in lattice units.

In Fig. 4.24, we report the distribution of pair momentum with fixing N_\downarrow to 15 and varying N_\uparrow . It is apparent that $n_{pair}(k)$ peaks at a nonzero value for all plots due to the unbalanced populations of the two spin species. As the spin polarization becomes stronger, the peak moves to the right due to the increasing mismatch between the two Fermi surfaces. The dashed lines at certain values of k are calculated according to Eq. (4.34), and they are all in agreement with the positions of the peaks. Since $q = \pm \frac{2\pi}{L} \left| \frac{N_\uparrow - N_\downarrow}{2} \right|$ does not depend on c_0 , the peaks lie at exactly the same positions for the different interactions shown in the upper and lower panels. Note that there is still some population of fermions at the high momentum. We believe that the attractive interaction combined with the spin polarization leads to a deformation of the Fermi surfaces that makes it easier to occupy high momentum states.

Let us conclude by talking about the numerical sign oscillation in this 1D system with unbalanced spin populations. Similar to Eq. (3.67), the path integral for a one-dimensional system is expressed as

$$Z_{N_\uparrow, N_\downarrow}(\alpha_t L_t) = \prod_{n, n_t} \left[\int \mathcal{D}s(n, n_t) \right] \langle \Phi_{N_\uparrow, N_\downarrow}^{0, free} | M(s, L_t - 1) \cdots M(s, 0) | \Phi_{N_\uparrow, N_\downarrow}^{0, free} \rangle, \quad (4.36)$$

where $|\Phi_{N_\uparrow, N_\downarrow}^{0, free}\rangle$ is the normalized Slater determinant for the ground state of a non-interacting system of N_\uparrow up spins and N_\downarrow down spins. The transfer matrix reads

$$M(s, n_t) =: \exp \left\{ -H_{free} \alpha_t + \sum_n \sqrt{-c_0 \alpha_t} s(n, n_t) \left[\rho_\uparrow^{a^\dagger} a(n) + \rho_\downarrow^{a^\dagger} a(n) \right] \right\} : . \quad (4.37)$$

Note that $M(s, n_t)$ only contains single-particle operators interacting with the auxiliary field

and no direct particle-particle interactions. We write the path integral explicitly as

$$\begin{aligned}
Z_{N_\uparrow, N_\downarrow}(\alpha_t L_t) &= \prod_{n, n_t} \left[\int ds(n, n_t) e^{-\frac{1}{2}[s(n, n_t)]^2} \right] \\
&\quad \times \left\langle \Phi_{N_\uparrow, N_\downarrow}^{0, free} \left| M(s, L_t - 1) \cdots M(s, 0) \right| \Phi_{N_\uparrow, N_\downarrow}^{0, free} \right\rangle \\
&= \prod_{n, n_t} \left[\int ds(n, n_t) \right] \exp \left\{ -\frac{1}{2} \sum_{n, n_t} [s(n, n_t)]^2 \right\} \\
&\quad \times \det[\mathcal{M}_\uparrow(s, t)] \det[\mathcal{M}_\downarrow(s, t)],
\end{aligned} \tag{4.38}$$

where

$$\left[\mathcal{M}_\sigma(s, t) \right]_{k, k'} = \left\langle \mathbf{p}_{\sigma, k} \left| M(s, L_t - 1) \cdots M(s, 0) \right| \mathbf{p}_{\sigma, k'} \right\rangle, \tag{4.39}$$

with matrix indices $k, k' = 1, \dots, N_\sigma$. $|\mathbf{p}_{\sigma, k}\rangle$ and $|\mathbf{p}_{\sigma, k'}\rangle$ are the single-particle momentum states filled in from low to high momentum⁸. The hermicity of \mathcal{M}_σ leads to a real-valued $\det[\mathcal{M}_\sigma]$; however, we cannot guarantee that $\det[\mathcal{M}_\uparrow(s, t)] \det[\mathcal{M}_\downarrow(s, t)]$ is non-negative with the condition $N_\uparrow \neq N_\downarrow$ and we indeed encounter the numerical sign problem here. In order to use the importance sampling in our Monte Carlo simulations, we employ the mixing

$$x|f(s, \alpha_t L_t)| + (1 - x)|f(s, \alpha_t L_t - \alpha_t)| \quad (0 < x < 1) \tag{4.40}$$

as the weight, where

$$f(s, \alpha_t L_t) = \exp \left\{ -\frac{1}{2} \sum_{n, n_t} [s(n, n_t)]^2 \right\} \det[\mathcal{M}_\uparrow(s, t)] \det[\mathcal{M}_\downarrow(s, t)]. \tag{4.41}$$

⁸See details in section 4.4.1

The sign oscillation can be measured as

$$\langle \text{Sign}[f(s, \alpha_t L_t)] \rangle, \quad (4.42)$$

which we find to be very close to 1. Therefore, the sign oscillation in this system is fairly weak so that good statistics can be achieved by a slight increase of the computational cost.

Chapter 5

Summary and outlook

In this thesis we have presented the ab initio studies of the Fermi systems in lattice effective field theory. We have determined the universal parameter ξ in the unitary limit at zero temperature for two-component fermion systems with $N_\uparrow = N_\downarrow = 33$. The results are calculated in the continuum limit by the extrapolation to an infinite box size. Using extrapolation functions $A\rho^{2/3} + B\rho + \xi$ and $B\rho + C\rho^{4/3} + \xi$, we have found

$$\xi_{N_\uparrow, N_\downarrow}^{thermo} = 0.369(2), \quad \xi_{N_\uparrow, N_\downarrow} = 0.373(2), \quad (5.1)$$

and

$$\xi_{N_\uparrow, N_\downarrow}^{thermo} = 0.370(1), \quad \xi_{N_\uparrow, N_\downarrow} = 0.371(1), \quad (5.2)$$

respectively. These values are in agreement with the latest results by numerical calculations [161,163] and the experiment [131]. We have also investigated the superfluidity in the ground state of the ultracold Fermi systems at unitarity. The superfluid phase is characterized by the non-vanishing ODLRO of the two body density matrix and the condensate fraction has been calculated in the continuum limit,

$$\alpha = 0.43(1). \quad (5.3)$$

This value agrees with the experiments [170,171], but is lower than the numerical calculations [162,169,172,173]. We are the first to study the pair wave function in the condensate state by an ab initio method. At unitarity, the pair size ζ_p is proportional to k_F^{-1} and we have found

$$\zeta_p = 0.193(9)k_F^{-1}. \quad (5.4)$$

In those non-polarized Fermi systems, the simulations are all done by the GPU-based algorithms, which shows a significantly boosted computational efficiency compared to the CPU-based algorithms. In even larger systems, this boost will be enhanced. For the work we have done, we only focus on the S-wave scattering and the unitary limit. In the future, we can explore the nuclear superfluidity in finite systems with more realistic nuclear forces. The two-dimensional Fermi systems, like layered superconductors, could also be a good direction using our current framework.

For the one-dimensional spin-polarized systems, we have characterized the FFLO phase by an spatially modulated order parameter and the oscillation period of the order parameter is obtained as

$$R_\Delta = \frac{2L}{|N_\uparrow - N_\downarrow|}. \quad (5.5)$$

In systems with different spin polarizations, the pair momentum distributions are all found to peak at the nonzero momenta.

Eigenvector continuation method is employed in the simulations of the neutron matter and shown to reduce errors by an order of magnitude compared to the direct calculations in cases where there exists a strong sign problem. This method is proved by the technique of analytic continuation, and we demonstrate that while an eigenvector resides in a linear space with enormous dimensions, the eigenvector trajectory generated by a smoothly

changed Hamiltonian matrix is well approximated by a relatively low-dimensional manifold. To approximate this low-dimensional manifold with desired accuracy, the number of vectors needed is dependent on the number of necessary analytic expansions and the convergence rate of each series expansion. If the norm kernel and Hamiltonian kernel can be computed with sufficient accuracy, then in principle any eigenvector problem can be solved by this method. For instance, this method can be used to extend the convergence region of perturbation theory [45]. While we have emphasized the use of eigenvector continuation to perform the extrapolations in the control parameter, it can also be applied to where the interpolation is the most interesting question. One example is the BCS-BEC crossover. We can use the variational wave functions that work very well on BCS and BEC sides, respectively and then use eigenvector continuation to perform an interpolation to find a good wave function for the crossover transition.

BIBLIOGRAPHY

BIBLIOGRAPHY

- [1] J. J. Sakurai. Modern Quantum Mechanics (Revised Edition). Addison Wesley, 1st edition, 1993.
- [2] E. Feenberg. The scattering of slow electrons by neutral atoms. *Phys. Rev.*, 40:40-54, 1932.
- [3] J. R. Taylor. Scattering Theory - The Quantum Theory of Nonrelativistic Collisions. R.E. Krieger Publishing Company, reprint edition, 1972.
- [4] H. A. Bethe. Theory of the effective range in nuclear scattering. *Phys. Rev.*, 76:38-50, Jul 1949.
- [5] J. D. Jackson and J. M. Blatt. The interpretation of low energy proton-proton scattering. *Rev. Mod. Phys.*, 22:77-118, Jan 1950.
- [6] M. Lüscher. Volume Dependence of the Energy Spectrum in Massive Quantum Field Theories. 1. Stable Particle States, *Commun. Math. Phys.* 104:177-206, Jun 1986.
- [7] M. Lüscher. Volume Dependence of the Energy Spectrum in Massive Quantum Field Theories. 2. Scattering States, *Commun. Math. Phys.* 105:153-188, Jun 1986.
- [8] S. R. Beane, P. F. Bedaque, A. Parreno, and M. J. Savage. Two nucleons on a lattice. *Phys. Lett. B*, 585:106-114, 2004.
- [9] R. Seki and U. van Kolck. Effective field theory of nucleon-nucleon scattering on large discrete lattices. *Phys. Rev. C*, 73:044006, 2006.
- [10] D. Lee and T. Schäfer. Neutron matter on the lattice with pionless effective field theory. *Phys. Rev. C*, 72:024006, Aug 2005.
- [11] X. Li and C. Liu. Two particle states in an asymmetric box. *Phys. Lett. B*, 587:100-104, 2004.
- [12] X. Feng, X. Li and C. Liu. Two particle states in an asymmetric box and the elastic scattering phases. *Phys. Rev. D*, 70:014505, 2004.
- [13] K. Rummukainen and S. A. Gottlieb. Resonance scattering phase shifts on a non-rest frame lattice. *Nucl. Phys. B*, 450:397-436, 1995.
- [14] V. Bernard, M. Lage, U.-G. Meißner and A. Rusetsky. Resonance properties from the finite-volume energy spectrum. *JHEP* 0808:024, 2008.

- [15] K. Polejaeva and A. Rusetsky. Three particles in a finite volume. *Eur. Phys. J. A*, 48:67, 2012.
- [16] C. P. Burgess. Introduction to effective field theory. *Ann. Rev. Nucl. Part. Sci.* 57:329-362, 2007.
- [17] A. Pich. Effective field theory (lectures at the 1997 Les Houches summer school “Probing the Standard Model of Particle Interactions”) [arXiv:hep-ph/9806303].
- [18] C. N. Yang. Fermi’s β -decay Theory. *Asia Pacific Physics Newsletter*. 1 (01): 2730, (2012).
- [19] T. Appelquist and J. Carazzone. Infrared singularities and massive fields. *Phys. Rev. D*, 11:2856-2861, 1975.
- [20] W. Buchmuller, D. Wyler. Effective Lagrangian analysis of new interactions and flavor conservation. *Nucl. Phys. B*, 268:621-653, 1986.
- [21] B. Grinstein, MB. Wise, *Phys. Lett. B*, 265:326-334, 1991.
- [22] U.-G. Meißner. Recent developments in chiral perturbation theory. *Rept. Prog. Phys.*, 56:903-996, 1993.
- [23] A.V. Manohar (1977) Effective field theories. In: Latal H., Schweiger W. (eds) *Perturbative and Nonperturbative Aspects of Quantum Field Theory. Lecture Notes in Physics*, vol 479. Springer, Berlin, Heidelberg.
- [24] F. Strocchi. Locality, charges and quark confinement. *Phys. Lett. B*, 62:60, 1976.
- [25] H. Araki, K. Hepp and D. Ruelle. On the Asymptotic behaviour of Wightman functions in space-like directions. *Helv. Phys. Acta*, 35:164, 1962.
- [26] S. Weinberg. Phenomenological Lagrangians. *Physica A*, 96:327-340, 1979.
- [27] H. Leutwyler, *Ann. Phys.*, 235:165-203, 1994.
- [28] E. Epelbaum, H.-W. Hammer, and U.-G. Meißner. Modern theory of nuclear forces. *Rev. Mod. Phys.*, 81:1773-1825, 2009.
- [29] R. Machleidt, D. R. Entem. Chiral effective field theory and nuclear forces. *Phys. Rept.*, 503:1-75, 2011.
- [30] E. Epelbaum, H. Krebs, D. Lee, and U.-G. Meißner. Lattice calculations for $A = 3, 4, 6, 12$ nuclei using chiral effective field theory. *Eur. Phys. J. A*, 45:335-352, 2010.

- [31] I. Karatsas and S. Shreve. *Brownian Motion and Stochastic Calculus*, 2nd ed. New York: Springer-Verlag, 1997.
- [32] P. A. M. Dirac. The Lagrangian in quantum mechanics. *Physikalisches Zeitschrift Der Sowjetunion*, 3:6472, 1933.
- [33] R. P. Feynman. Space-time approach to non-relativistic quantum mechanics. *Rev. Mod. Phys.*, 20:367387, Apr 1948.
- [34] A. Zee. *Quantum Field Theory in a Nutshell*. Princeton University Press, 2nd edition, 2010.
- [35] M. Creutz. Global MOnTe Carlo algorithms for many-fermions systems. *Phys. Rev. D*, 38:1228-1238, 1988.
- [36] M. Creutz. Transfer matrices and lattice fermions at finite density. *Found. Phys.*, 30:487-492, 2000.
- [37] J. Hubbard. Calculation of partition functions. *Phys. Rev. Lett.*, 3:77-78, 1959.
- [38] R. L. Stratonovich. On a method of calculating quantum distribution function. *Soviet Phys., Doklady*, 2:416 (1957).
- [39] R. M. Neal. *Probabilistic Inference Using Markov Chain Monte Carlo Methods*. Department of Computer Science, University of Toronto.
- [40] W.R. Gilks, S. Richardson, David Spiegelhalter. *Markov Chain Monte Carlo in Practice*. Chapman and Hall/CRC, 1st edition, 1995.
- [41] G.C. Wei and M.A. Tanner. A monte carlo implementation of the EM algorithm and the poor mans data augmentation algorithms. *J. Am. Stat. Assoc.*, 85:699-704, 1990.
- [42] D.J.C. Mackay. *Introduction to Monte Carlo Methods*, 1998. In: Jordan M.I. (eds) *Learning in Graphical Models*. NATO ASI Series (Series D: Behavioural and Social Sciences), vol 89. Springer, Dordrecht.
- [43] W. K. Hastings. Monte Carlo sampling methods using Markov chains and their applications. *Biometrika*, 57:97-109, Apr 1970.
- [44] A. C. Cameron and P. K. Trivedi. *Microeconometrics : methods and applications*, pp. 375. Cambridge New York: Cambridge University Press, 2005.
- [45] D. Frame, R.-Z. He, I. Ipsen, Da. Lee, De. Lee and E. Rrapaj. Eigenvector continuation with subspace learning. *Phys. Rev. Lett.*, 121:032501, 2018.

- [46] Y. Alhassid, D. J. Dean, S. Koonin, G. Lang, and W. E. Ormand. Practical solution to the Monte Carlo sign problem: Realistic calculation of ^{54}Fe . *Phys. Rev. Lett.*, 72:613-616, 1994.
- [47] T. A. Lähde, T. Luu, D. Lee, U.-G. Meißner, E. Epelbaum, H. Krebs, and G. Rupak. Nuclear lattice simulations using symmetry-sign extrapolation. *Eur. Phys. J. A*, 51:92, 2015.
- [48] S. Elhatisari, N. Li, A. Rokash, J. M. Alarcón, D. Du, N. Klein, B.-N. Lu, U.-G. Meißner, E. Epelbaum, H. Krebs, T. A. Lähde, D. Lee, and G. Rupak. Nuclear binding energy near a quantum phase transition. *Phys. Rev. Lett.*, 117:132501, 2016.
- [49] S. Elhatisari, E. Epelbaum, H. Krebs, T. A. Lähde, D. Lee, N. Li, B.-N. Lu, U.-G. Meißner, and G. Rupak. Ab initio calculations of the isotopic dependence of nuclear clustering. *Phys. Rev. Lett.*, 119:222505, 2017.
- [50] D. Lee. Tutorial: methods for few body systems. In: *Progress in Diagrammatic Monte Carlo Methods for Quantum Field Theories in Particle-, Nuclear-, and Condensed Matter*. *Physics. Lect. Notes Phys.*, 936:237, 2017.
- [51] B. Borasoy, E. Epelbaum, H. Krebs, D. Lee and U.-G. Meißner. Lattice simulations for light nuclei: Chiral effective field theory at leading order. *Eur. Phys. J. A*, 31:105-123, 2007.
- [52] C. Lanczos. An iteration method for the solution of the eigenvalue problem of linear differential and integral operators. *J. Res. Nat. Bur. Stand.*, 45:255-282, 1950.
- [53] Y. Saad. *Numerical Methods for Large Eigenvalue Problems*, vol. 66 of *Classics in Applied Mathematics*. (Society for Industrial and Applied Mathematics (SIAM), Philadelphia, PA, 2011), revised edition of the 1992 original.
- [54] D. Lee, N. Salwen, and M. Windolowski. Introduction to stochastic error correction methods. *Phys. Lett. B*, 502:329-337, 2001.
- [55] K. Onnes. Investigations into the properties of substances at low temperatures, which have led, amongst other things, to the preparation of liquidhelium. Nobel lecture, Dec 1913, in *Nobel Lectures, Physics 1901-1921*, (Elsevier Publishing Company, Amsterdam) 1967.
- [56] M. R. Schafroth. Remarks on the Meissner effect. *Phys. Rev.*, 111:72-74, 1958.
- [57] C. A. Reynolds, B. Serin, W. H. Wright, and L. B. Nesbitt. Superconductivity of isotopes of mercury. *Phys. Rev.*, 78:487, 1950.

- [58] E. Maxwell. Isotope effect in the superconductivity of mercury. *Phys. Rev.*, 78:477, 1950.
- [59] H. Fröhlich. Theory of the superconducting state. I. the ground state at the absolute zero of temperature. *Phys. Rev.*, 79:845-856, 1950.
- [60] J. Bardeen, L. N. Cooper, and J. R. Schrieffer. Theory of superconductivity. *Phys. Rev.*, 108:1175-1204, Dec 1957.
- [61] B.S. Chandrasekhar. A note on the maximum critical field of high-field superconductors. *Appl. Phys. Lett.*, 1:7-8, 1962.
- [62] A.M. Clogston. Upper limit for the critical field in hard superconductors. *Phys. Rev. Lett.*, 9:266-267, 1962.
- [63] P. Fulde and R. A. Ferrell. Superconductivity in a strong spin-exchange field. *Phys. Rev.*, 135:A550-A563, 1964.
- [64] A. I. Larkin and Yu. N. Ovchinnikov. Inhomogeneous state of superconductors. *Zh. Eksp. Theor. Fiz.* 47:1136, 1964 [*Sov. Phys. JETP*, 20:762-769, 1965].
- [65] Y. Shin, M. W. Zwierlein, C. H. Schunck, A. Schirotzek, and W. Ketterle. Observation of phase separation in a strongly interacting imbalanced Fermi gas. *Phys. Rev. Lett.*, 97:030401, 2006.
- [66] G. B. Partridge, W. Li, Y.-a. Liao, R. G. Hulet, and H. T. C. Stoof. Deformation of a trapped Fermi gas with unequal spin populations. *Phys. Rev. Lett.*, 97:190407, 2006.
- [67] T. Mizushima, K. Machida, and M. Ichioka. Direct imaging of spatially modulated superfluid phases in atomic fermion systems. *Phys. Rev. Lett.*, 94:060404, 2005.
- [68] J. Kinnunen, L. M. Jensen, and P. Törmä. Strongly interacting Fermi gases with density imbalance. *Phys. Rev. Lett.*, 96:110403, 2006.
- [69] X.-J. Liu, H. Hu, and P. D. Drummond. Fulde-Ferrell-Larkin-Ovchinnikov states in one-dimensional spin-polarized ultracold atomic Fermi gases. *Phys. Rev. A*, 76:043605, 2007.
- [70] M. R. Bakhtiari, M. J. Leskinen, and P. Torma. Spectral signatures of the Fulde-Ferrell-Larkin-Ovchinnikov order parameter in one-dimensional optical lattices. *Phys. Rev. Lett.*, 101:120404, 2008.
- [71] J. M. Edge and N. R. Cooper. Signature of the Fulde-Ferrell-Larkin-Ovchinnikov phase in the collective modes of a trapped ultracold Fermi gas. *Phys. Rev. Lett.*, 103:065301, 2009.

- [72] R. A. Molina, J. Dukelsky, and P. Schmitteckert. Comment on “spectral signatures of the Fulde-Ferrell-Larkin-Ovchinnikov order parameter in one-dimensional optical lattices”. *Phys. Rev. Lett.*, 102:168901, 2009.
- [73] M. Casula, D. M. Ceperley, and E. J. Mueller. Quantum Monte Carlo study of one-dimensional trapped fermions with attractive contact interactions. *Phys. Rev. A*, 78:033607, 2008.
- [74] J. C. Pei, J. Dukelsky, and W. Nazarewicz. Competition between normal superfluidity and Larkin-Ovchinnikov phases of polarized Fermi gases in elongated traps. *Phys. Rev. A*, 82:021603(R), 2010.
- [75] T. K. Koponen, T. Paananen, J.-P. Martikainen, M.R. Bakhtiari, P. Torma. FFLO state in 1, 2, and 3 dimensional optical lattices combined with a non-uniform background potential. *New J. Phys.*, 10:045014, 2008.
- [76] H. Shimahara. Transition from the vortex state to the FuldeFerrellLarkinOvchinnikov state in quasi-two-dimensional superconductors. *Phys. Rev. B*, 80:214512, 2009.
- [77] Y. Kamihara, T. Watanabe, M. Hirano, and H. Hosono. Iron-based layered superconductor $\text{La}[\text{O}_{1-x}\text{F}_x]\text{FeAs}$ ($x = 0.050.12$) with $T_c = 26$ K. *J. Am. Chem. Soc.*, 130:32966297, 2008.
- [78] A. Gurevich. Iron-based superconductors at high magnetic fields. *Rep. Prog. Phys.*, 74:124501, 2011.
- [79] T. Terashima, K. Kihou, M. Tomita, S. Tsuchiya, N. Kikugawa, S. Ishida, C.-H. Lee, A. Iyo, H. Eisaki, and S. Uji. Hysteretic superconducting resistive transition in $\text{Ba}_{0.07}\text{K}_{0.93}\text{Fe}_2\text{As}_2$. *Phys. Rev. B*, 87:184513, 2013.
- [80] C.-w. Cho, J. H. Yang, N. F. Q. Yuan, J. Shen, T. Wolf, and R. Lortz. Thermodynamic Evidence for the Fulde-Ferrell-Larkin-Ovchinnikov State in the KFe_2As_2 Superconductor. *Phys. Rev. Lett.*, 119:217002, 2017.
- [81] J. Müller, M. Lang, F. Steglich, J. A. Schlueter, A. M. Kini, U. Geiser, J. Mohtasham, R. W. Winter, G. L. Gard, T. Sasaki, and N. Toyota. Comparative thermal-expansion study of $\beta'' - (\text{ET})_2\text{SF}_5\text{CH}_2\text{CF}_2\text{SO}_3$ and $\kappa - (\text{ET})_2\text{Cu}(\text{NCS})_2$: Uniaxial pressure coefficients of T_c and upper critical fields. *Phys. Rev. B*, 61:11739, 2000.
- [82] K. Cho, B. E. Smith, W. A. Coniglio, L. E. Winter, C. C. Agosta, and J. A. Schlueter. Upper critical field in the organic superconductor $\beta'' - (\text{ET})_2\text{SF}_5\text{CH}_2\text{CF}_2\text{SO}_3$: Possibility of Fulde-Ferrell-Larkin-Ovchinnikov state. *Phys. Rev. B*, 79:220507(R), 2009

- [83] G. Koutroulakis, H. Kühne, J. A. Schlueter, J. Wosnitza, and S. E. Brown. Microscopic study of the Fulde-Ferrell-Larkin-Ovchinnikov state in an all-organic superconductor. *Phys. Rev. Lett.*, 116:067003, 2016.
- [84] R. Beyer, B. Bergk, S. Yasin, J. A. Schlueter, and J. Wosnitza. Angle-dependent evolution of the Fulde-Ferrell-Larkin-Ovchinnikov state in an organic superconductor. *Phys. Rev. Lett.*, 109:027003, 2012.
- [85] J. Singleton, J. A. Symington, M.-S. Nam, A. Ardavan, M. Kurmoo, and P. Day. Observation of the Fulde-Ferrell-Larkin-Ovchinnikov state in the quasi-two-dimensional organic superconductor. κ -(BEDT-TTF)₂Cu(NCS)₂(BEDT-TTF=bis(ethylene-dithio)tetrathiafulvalene). *J. Phys.: Condens. Matter*, 12:L641L648, 2000.
- [86] B. Bergk, A. Demuer, I. Sheikin, Y. Wang, J. Wosnitza, Y. Nakazawa, and R. Lortz. Magnetic torque evidence for the Fulde-Ferrell-Larkin-Ovchinnikov state in the layered organic superconductor κ - (BEDT - TTF)₂Cu(NCS)₂. *Phys. Rev. B*, 83:064506, 2011.
- [87] C. C. Agosta, Jing Jin, W. A. Coniglio, B. E. Smith, K. Cho, I. Stroe, C. Martin, S. W. Tozer, T. P. Murphy, E. C. Palm, J. A. Schlueter, and M. Kurmoo. Experimental and semiempirical method to determine the Pauli-limiting field in quasi-two-dimensional superconductors as applied to κ - (BEDT - TTF)₂Cu(NCS)₂: Strong evidence of a FFLO state. *Phys. Rev. B*, 85:214514, 2012.
- [88] H. Mayaffre, S. Krämer, M. Horvatić, C. Berthier, K. Miyagawa, K. Kanoda, and V. F. Mitrović. Evidence of Andreev bound states as a hallmark of the FFLO phase in κ - (BEDT - TTF)₂Cu(NCS)₂. *Nat. Phys.*, 10:928932, 2014.
- [89] S. Tsuchiya, J.-i. Yamada, K. Sugii, D. Graf, J. S. Brooks, T. Terashima, and S. Uji. Phase boundary in a superconducting state of κ - (BEDT - TTF)₂Cu(NCS)₂: Evidence of the Fulde-Ferrell-Larkin-Ovchinnikov Phase. *J. Phys. Soc. Jpn.*, 84:034703, 2015.
- [90] C. C. Agosta, N. A. Fortune, S. T. Hannahs, S. Gu, L. Liang, J.-H. Park, and J. A. Schlueter. Calorimetric measurements of magnetic-field-induced inhomogeneous superconductivity above the paramagnetic limit. *Phys. Rev. Lett.*, 118:267001, 2017.
- [91] S. Uji, K. Kodama, K. Sugii, T. Terashima, Y. Takahide, N. Kurita, S. Tsuchiya, M. Kimata, A. Kobayashi, B. Zhou, and H. Kobayashi. Magnetic torque studies on FFLO phase in magnetic-field-induced organic superconductor λ -(BETS)₂FeCl₄. *Phys. Rev. B*, 85:174530, 2012.
- [92] M. A. Tanatar, T. Ishiguro, H. Tanaka, and H. Kobayashi. Magnetic field-temperature phase diagram of the quasi-two-dimensional organic superconductor λ -(BETS)₂GaCl₄ studied via thermal conductivity. *Phys. Rev. B*, 66:134503, 2002.

- [93] W. A. Coniglio, L. E. Winter, K. Cho, C. C. Agosta, B. Fravel, and L. K. Montgomery. Superconducting phase diagram and FFLO signature in λ -(BETS) $_2$ GaCl $_4$ from rf penetration depth measurements. *Phys. Rev. B*, 83:224507, 2011.
- [94] S. Uji, K. Kodama, K. Sugii, T. Terashima, T. Yamaguchi, N. Kurita, S. Tsuchiya, T. Konoike, M. Kimata, A. Kobayashi, B. Zhou, and H. Kobayashi. Vortex dynamics and diamagnetic torque signals in two dimensional organic superconductor λ -(BETS) $_2$ GaCl $_4$. *J. Phys. Soc. Jpn.*, 84:104709, 2015.
- [95] Y.-a. Liao, A. S. C. Rittner, T. Paprotta, W. Li, G. B. Partridge, R. G. Hulet, S. K. Baur, and E. J. Mueller. Spin-imbalance in a one-dimensional Fermi gas. *Nature* 467:567569, 2010.
- [96] M. W. Zwierlein, A. Schirotzek, C. H. Schunck, and W. Ketterle. Fermionic superfluidity with imbalanced spin populations. *Science*, 311:492496, 2006.
- [97] G. B. Partridge, W. Li, R. I. Kamar, Y.-a. Liao, and R. G. Hulet. Pairing and phase separation in a polarized Fermi gas. *Science*, 311:503505, 2006.
- [98] Y.-I. Shin, C. H. Schunck, A. Schirotzek, and W. Ketterle. Phase diagram of a two-component Fermi gas with resonant interactions. *Nature*, 451:689693, 2008.
- [99] S. Nascimbène, N. Navon, K. J. Jiang, L. Tarruell, M. Teichmann, J. McKeever, F. Chevy, and C. Salomon. Collective oscillations of an imbalanced Fermi gas: axial compression modes and polaron effective mass. *Phys. Rev. Lett.*, 103:170402, 2009.
- [100] D. E. Sheehy and L. Radzihovsky. BEC-BCS crossover, phase transitions and phase separation in polarized resonantly-paired superfluids. *Ann. Phys.*, 322:17901924, 2007.
- [101] A. Bulgac and M. M. Forbes. Unitary Fermi supersolid: the Larkin-Ovchinnikov phase. *Phys. Rev. Lett.*, 101:215301, 2008.
- [102] J. R. Schrieffer. Theory of Superconductivity. *Phys. Rev.*, 108:1175-1204, Dec 1957.
- [103] V. N. Popov. Theory of a Bose gas produced by bound states of Fermi particles. *Zh. Eksp. Teor. Fiz.*, 50:1550-1558, 1966 [*Sov. Phys. JETP*, 23:1034-1039, 1968].
- [104] L. V. Keldysh and A. N. Kozlov. Collective properties of excitons in semiconductors. *Zh. Eksp. Teor. Fiz.*, 54:978-993, 1968 [*Sov. Phys. JETP*, 27:521-528, 1968].
- [105] D. M. Eagles. Possible pairing without superconductivity at low carrier concentrations in bulk and thin-film superconducting semiconductors. *Phys. Rev.*, 186:456-463, 1969.
- [106] A. J. Leggett. Diatomic molecules and Cooper pairs. In: A. Pekalski, J. A. Przystawa (eds) *Modern Trends in the Theory of Condensed Matter. Lecture Notes in Physics*, vol 115. Springer, Berlin, Heidelberg.

- [107] W. Ketterle, M. W. Zwierlein. Making, probing and understanding ultracold Fermi gases. Proceedings of the International School of Physics En-rico Fermi, Course CLXIV, Varenna, 20 - 30 June 2006, edited by M. Inguscio, W.Ketterle, and C. Salomon (IOS Press, Amsterdam) 2008.
- [108] T.-L. Ho. Universal thermodynamics of degenerate quantum gases in the unitarity limit. *Phys. Rev. Lett.*, 92:090402, 2004.
- [109] G. F. Bertsch. The many-body challenge problem formulated by G. F. Bertsch in 1999, see R. A. Bishop, *Int. J. Mod. Phys. B* 15, iii, 2001.
- [110] C.Chin, R. Grimm, P. Julienne, and E. Tiesinga. Feshbach resonances in ultracold gases. *Rev. Mod. Phys.*, 82:1225-1286, Apr 2010.
- [111] C. Gros. The boundary condition integration technique: results for the Hubbard model in 1D and 2D. *Physik B - Condensed Matter*, 86:359, 1992.
- [112] C. Gros. Control of the finite-size corrections in exact diagonalization studies. *Phys. Rev. B*, 53:6865-6868, 1996.
- [113] C. Lin, F.-H. Zong, and D. M. Ceperley. Twist-averaged boundary conditions in continuum quantum Monte Carlo. *Phys. Rev. E*, 64:016702, 2001.
- [114] G. Hagen, T. Papenbrock, A. Ekström, K. A. Wendt, G. Baardsen, S. Gandolfi, M. Hjorth-jensen, and C. J. Horowitz. Coupled-cluster calculations of nucleonic matter. *Phys. Rev. C*, 89:014319, 2014.
- [115] B. Schuetrumpf, and W. Nazarewicz. Twist-averaged boundary conditions for nuclear pasta Hartree-Fock calculations. *Phys. Rev. C*, 92:045806, 2015.
- [116] B. C. Tiburzi. Flavor twisted boundary conditions and the nucleon axial current. *Phys. Lett. B*, 617:40-48, 2005.
- [117] R. A. Briceño, Z. Davoudi, T. C. Luu, and M. J. Savage. Two-Baryon Systems with Twisted Boundary Conditions. *Phys. Rev. D*, 89:074509, 2014.
- [118] B. Carter, N. Chamel, and P. Haensel. Entrainment coefficient and effective mass for conduction neutrons in neutron star crust: simple microscopic models. *Nuclear Physics A*, 748:675, 2005.
- [119] N. Chamel, S. Naimi, E. Khan, and J. Margueron. On the validity of the Wigner-Seitz approximation in neutron star crust. *Phys. Rev. C*, 75:055806, 2007.
- [120] B.-N. Lu, T. A. Lähde, D. Lee and U.-G. Meißner. Precise determination of lattice phase shifts and mixing angles. *Phys. Rev. B*, 760:309-313, 2016.

- [121] K. M. O'Hara, S. L. Hemmer, M. E. Gehm, S. R. Granade, and J. E. Thomas. Observation of a strongly interacting degenerate Fermi gas of atoms. *Science*, 298:2179, 2002.
- [122] M. E. Gehm, S. L. Hemmer, S. R. Granade, K. M. O'Hara, and J. E. Thomas. Mechanical stability of a strongly interacting Fermi gas of atoms. *Phys. Rev. A*, 68:011401, 2003.
- [123] T. Bourdel, L. Khaykovich, J. Cubizolles, J. Zhang, F. Chevy, M. Teichmann, L. Tarruell, S. J. J. M. F. Kokkelmans, and C. Salomon. Experimental Study of the BEC-BCS Crossover Region in Lithium 6. *Phys. Rev. Lett.*, 93:050401, 2004.
- [124] M. Bartenstein, A. Altmeyer, S. Riedl, S. Jochim, C. Chin, J. H. Denschlag, and R. Grimm. Crossover from a molecular Bose-Einstein condensate to a degenerate Fermi gas. *Phys. Rev. Lett.*, 92:120401, 2004.
- [125] J. Kinast, A. Turlapov, J. E. Thomas, Q. Chen, J. Stajic, and K. Levin. Heat capacity of a strongly interacting Fermi gas. *Science*, 307:1296, 2005.
- [126] C. A. Regal, M. Greiner, S. Giorgini, M. Holland, and D. S. Jin. Momentum distribution of a Fermi gas of atoms in the BCS-BEC crossover. *Phys. Rev. Lett.*, 95:250404, 2005.
- [127] J. T. Stewart, J. P. Gaebler, C. A. Regal, and D. S. Jin. Potential energy of a ^{40}K Fermi gas in the BCS-BEC crossover. *Phys. Rev. Lett.*, 97:220406, 2006.
- [128] L. Luo and J. E. Thomas. Thermodynamic measurements in a strongly interacting Fermi gas. *J. Low Temp. Phys.* 154:1-29, 2009.
- [129] N. Navon, S. Nascimbène, F. Chevy, and C. Salomon. The equation of state of a low-temperature Fermi gas with tunable interactions. *Science*, 328:729-732, 2010.
- [130] S. Nascimbène, N. Navon, K. J. Jiang, F. Chevy, and C. Salomon. Exploring the thermodynamics of a universal Fermi gas. *Nature (London)*, 463:1057-1060, 2010.
- [131] M. J. H. Ku, A. T. Sommer, L. W. Cheuk, M. W. Zwierlein. Revealing the superfluid lambda transition in the universal thermodynamics of a unitary Fermi gas. *Science*, 335:563-567, 2012.
- [132] J. R. Engelbrecht, Mohit Randeria, and C. A. R. Sáde Melo. BCS to Bose crossover: Broken-symmetry state. *Phys. Rev. B*, 55:15153, 1997.
- [133] G. A. Baker. Neutron matter model. *Phys. Rev. C*, 60:054311, 1999.
- [134] J. V. Steele. Effective field theory power counting at finite density. arXiv:nucl-th/0010066.

- [135] H. Heiselberg. Fermi systems with long scattering lengths. *Phys. Rev. A*, 63:043606, 2001.
- [136] A. Perali, P. Pieri, and G. C. Strinati. Quantitative comparison between theoretical predictions and experimental results for the BCS-BEC crossover. *Phys. Rev. Lett.*, 93:100404, 2004.
- [137] T. Schäfer, C.-W. Cao, and S. R. Cotanh. Many body methods and effective field theory. *Nucl. Phys. A*, 762:82, 2005.
- [138] T. Papenbrock. Density-functional theory for fermions in the unitary regime. *Phys. Rev. A*, 72:041603(R), 2005.
- [139] Y. Nishida and D. T. Son. ϵ Expansion for a Fermi Gas at Infinite Scattering Length. *Phys. Rev. Lett.*, 97:050403, 2006.
- [140] R. Haussmann, W. Rantner, S. Cerrito, and W. Zwerger. Thermodynamics of the BCS-BEC crossover. *Phys. Rev. A*, 75:023610, 2007.
- [141] M. Y. Veillette, D. E. Sheehy, and L. Radzihovsky. Large- N expansion for unitary superfluid Fermi gases. *Phys. Rev. A*, 75:043614, 2007.
- [142] P. Arnold, J. E. Drut, and D. T. Son. Next-to-next-to-leading order ϵ expansion for a Fermi gas at infinite scattering length. *Phys. Rev. A*, 75:043605, 2007.
- [143] Y. Nishida and D. T. Son. Fermi gas near unitarity around four and two spatial dimensions. *Phys. Rev. A*, 75:063617, 2007.
- [144] C. Ji-Sheng. Ground state energy of unitary fermion gas with the Thomson problem approach. *Chin. Phys. Lett.*, 24:1825, 2007.
- [145] Y. Nishida. Ground-state energy of the unitary Fermi gas from the ϵ expansion. *Phys. Rev. A*, 79:013627, 2009.
- [146] J. Carlson, S.-Y. Chang, V. R. Pandharipande, and K. E. Schmidt. Superfluid Fermi gases with large scattering length. *Phys. Rev. Lett.*, 91:050401, 2003.
- [147] S. Y. Yang, V. R. Pandharipande, J. Carlson, and K. E. Schmidt. Quantum Monte Carlo studies of superfluid Fermi gases. *Phys. Rev. A*, 70:043602, 2004.
- [148] G. E. Astrakharchik, J. Boronat, J. Casulleras, and S. Giorgini. Equation of state of a Fermi gas in the BEC-BCS crossover: a quantum Monte Carlo study. *Phys. Rev. Lett.*, 93:200404, 2004.
- [149] J. Carlson and S. Reddy. Asymmetric two-component fermion systems in strong coupling. *Phys. Rev. Lett.*, 95:060401, 2005.

- [150] D. Lee and T. Schäfer. Cold dilute neutron matter on the lattice. II. Results in the unitary limit. *Phys. Rev. C*, 73:015202, 2006.
- [151] A. Bulgac, J. E. Drut, and P. Magierski. Spin 1/2 fermions in the unitary regime: a superfluid of a new type. *Phys. Rev. Lett.*, 96:090404, 2006.
- [152] D. Lee. Ground-state energy of spin- $\frac{1}{2}$ fermions in the unitary limit. *Phys. Rev. B*, 73:115112, 2006.
- [153] O. Juillet. Sign-free stochastic mean-field approach to strongly correlated phases of ultracold fermions. *New J. Phys.*, 9:163, 2007.
- [154] D. Lee. The symmetric heavy-light ansatz. *Eur. Phys. J. A*, 35:171, 2008.
- [155] D. Lee. Ground state energy at unitarity. *Phys. Rev. C*, 78:024001, 2008.
- [156] A. Bulgac, J.E. Drut, and P. Magierski. Quantum Monte Carlo simulations of the BCS-BEC crossover at finite temperature. *Phys. Rev. A* 78:023625, 2008.
- [157] T. Abe and R. Seki. From low-density neutron matter to the unitary limit. *Phys. Rev. C*, 79:054003, 2009.
- [158] P. Magierski, G. Wlazowski, A. Bulgac, and J. E. Drut. Finite-temperature pairing gap of a unitary Fermi gas by quantum Monte Carlo calculations. *Phys. Rev. Lett.*, 103:210403, 2009.
- [159] S. Gandolfi, K. E. Schmidt, and J. Carlson. BEC-BCS crossover and universal relations in unitary Fermi gases. *Phys. Rev. A*, 83:041601(R), 2011.
- [160] M. G. Endres, D. B. Kaplan, J.-W. Lee, and A. N. Nicholson. Lattice Monte Carlo calculations for unitary fermions in a finite box. *Phys. Rev. A*, 87:023615, 2013.
- [161] M. M. Forbes, S. Gandolfi and A. Gezerlis. Resonantly interacting fermions in a box. *Phys. Rev. Lett.*, 106:235303, 2011.
- [162] X. Li, J. Kolorenč, and L. Mitas. Atomic Fermi gas in the unitary limit by quantum Monte Carlo methods: Effects of the interaction range. *Phys. Rev. A*, 84:023615, 2011.
- [163] J. Carlson, S. Gandolfi, K. E. Schmidt and S. Zhang. Auxiliary-field quantum Monte Carlo method for strongly paired fermions. *Phys. Rev. A*, 84:061602(R), 2011.
- [164] Ultracold Fermi Gases. In: Proceedings of the International School of Physics “Enrico Fermi”, Course 164, edited by M. Inguscio, W. Ketterle, C. Salomon (IOS Press, Amsterdam) 2007.

- [165] C. N. Yang. Concept of off-diagonal long-range order and the quantum phases of liquid He and of superconductors. *Rev. Mod. Phys.*, 34:694-704, 1962.
- [166] O. Penrose. CXXXVI. On the quantum mechanics of helium II. *Phil. Mag.*, 42:1373-1377, 1951.
- [167] O. Penrose and L. Onsager. Bose-Einstein condensation and liquid Helium. *Phys. Rev.*, 104:576-584, 1956.
- [168] S. De Palo, F. Rapisarda, and G. Senatore. Excitonic condensation in a symmetric electron-hole bilayer. *Phys. Rev. Lett.*, 88:206401, 2002.
- [169] G. Ortiz and J. Dukelsky. BCS-toBEC crossover from the exact BCS solution. *Phys. Rev. A*, 72:043611, 2005.
- [170] M. W. Zwierlein, C. A. Stan, C. H. Schunck, S. M. F. Raupach, A. J. Kerman, and W. Ketterle. Condensation of pairs of fermionic atoms near a Feshbach resonance. *Phys. Rev. Lett.*, 92:120403, 2004.
- [171] M. W. Zwierlein, C. H. Schunck, C. A. Stan, S. M. F. Raupach, and W. Ketterle. Formation dynamics of a fermion pair condensate. *Phys. Rev. Lett.*, 94:180401, 2005.
- [172] L. Salasnich, N. Manini, and A. Parola. Condensate fraction of a Fermi gas in the BCS-BEC crossover. *Phys. Rev. A*, 72:023621, 2005.
- [173] G. E. Astrakharchik, J. Boronat, J. Casulleras, and S. Giorgini. Momentum distribution and condensate fraction of a fermion gas in the BCS-BEC crossover. *Phys. Rev. Lett.*, 95:230405, 2005.
- [174] M. J. WOLAK (2012). *Quantum Monte Carlo studies of the population imbalanced Fermi Gas* (Doctoral dissertation). Retrieved from ScholarBank@NUS Repository (<https://scholarbank.nus.edu.sg/handle/10635/37484>).
- [175] L. N. Cooper. Bound electron pairs in a degenerate Fermi gas. *Phys. Rev.*, 104:11891190, 1956.